UNIVERSITY OF SÃO PAULO
SÃO CARLOS SCHOOL OF ENGINEERING

Douglas Ramalho Queiroz Pacheco

Nonlinear finite element aeroelastic modelling of reinforced skin panels in supersonic flows

São Carlos

2018

Douglas Ramalho Queiroz Pacheco

Modelagem aeroelástica não linear, pelo método dos elementos finitos, de painéis reforçados em escoamentos supersônicos

Dissertação apresentada à Escola de Engenharia de São Carlos da Universidade de São Paulo, para obtenção do título de Mestre em Ciências - Programa de Pós-Graduação em Engenharia Mecânica.

Área de concentração: Dinâmica e Mecatrônica

Supervisor: Flavio Donizeti Marques

São Carlos

2018

Catalog card prepared by Patron Service at "Prof. Dr. Sergio Rodrigues Fontes" Library at EESC/USP

Douglas Ramalho Queiroz Pacheco

Nonlinear finite element aeroelastic modelling of reinforced skin panels in supersonic flows

Master Dissertation presented to the University of São Paulo at São Carlos School of Engineering, for obtaining the title of Master of Science - Graduate Program in Mechanical Engineering, Research area in Dynamics and Mechatronics

Supervisor: Dr Flavio Donizeti Marques

São Carlos

2018

FOLHA DE JULGAMENTO

Candidato: Engenheiro **DOUGLAS RAMALHO QUEIROZ PACHECO**.

Título da dissertação: "Modelagem aeroelástica não linear, pelo método dos elementos finitos, de painéis reforçados em escoamento supersônicos".

Data da defesa: 03/08/2018.

Comissão Julgadora: **Resultado:**

Prof. Associado **Flávio Donizete Marques**   _APROVADO_
(Orientador)
(Escola de Engenharia de São Carlos/EESC)

Prof. Dr. **Thiago Augusto Machado Guimarães**   _APROVADO_
(Universidade Federal de Uberlândia/UFU)

Prof. Dr. **António Joaquim Mendes Ferreira**   _APROVADO_
(Universidade do Porto/FEUP)

Coordenador do Programa de Pós-Graduação em Engenharia Mecânica:
Prof. Associado **Gherhardt Ribatski**

Presidente da Comissão de Pós-Graduação:
Prof. Associado **Luís Fernando Costa Alberto**

ACKNOWLEDGEMENTS

ABSTRACT

PACHECO, D.R.Q. **Nonlinear finite element aeroelastic modelling of reinforced skin panels in supersonic flows.** 2018. 92p. MSc Dissertation - Escola de Engenharia de São Carlos, Universidade de São Paulo, São Carlos, 2018.

Panel flutter is an aeroelastic phenomenon that can cause critical structural failure in aerospace vehicles operating at supersonic speeds. A reliable modelling of such phenomenon is crucial for safely predicting the lifespan of aircraft skin, thus being of great importance to aerospace structural design. The vast majority of works published on this subject treat each skin panel as an isolated structure. In reality, however, aircraft skin is typically composed of large panels mounted over spars, stringers and other types of reinforcement elements. The presence of such stiffening components ends up subdividing the panel into multiple smaller cells that can interact during flutter, thereby making the aeroelastic motion potentially more complex and dangerous. Moreover, stiffeners are also deformable structures, which therefore take part in the dynamics of the problem. In this context, the present work deals with the study and implementation of a computational finite element model for the analysis of nonlinear flutter in stiffened panels. A combination of the Mindlin plate model and the Timoshenko beam model, both with geometric non-linearities, is employed. The model and the analyses tackle both isotropic and laminated panels. The aerodynamic forces are computed through first-order piston theory, which provides good results for high-supersonic flows. The energy equations are discretised via the Finite Element Method, and the resulting aeroelastic equations of motion are solved in the time domain through an iterative Newmark-type integration scheme. The final code is verified and validated through comparison with numerical solutions from the literature. As far as results and analyses are concerned, the present work focuses on three main aspects, thereby aiming to fill an existing gap in panel flutter literature: a) Investigating how stiffeners behave during flutter, from a dynamic perspective, and how their vibration affects the overall aeroelastic motion; b) Studying the influence of stiffener geometry on such effects; and c) Assessing the inaccuracies of the single-panel model by systematically comparing its results with those from the present multi-cell model. Results reveal novel aeroelastic phenomena arising from the modelling of stiffeners as flexible structural elements. Furthermore, the popular assumption of ideal fixation is proven to be potentially unconservative regarding the onset of flutter and the intensity of vibrations.

Keywords: Aerospace structures. Panel flutter. Nonlinear aeroelasticity. Finite element modelling. Reinforced plates. Nonlinear Timoshenko beam.

RESUMO

PACHECO, D.R.Q. **Modelagem aeroelástica não linear, pelo método dos elementos finitos, de painéis reforçados em escoamentos supersônicos.** 2018. 92p. Dissertação (Mestrado) - Escola de Engenharia de São Carlos, Universidade de São Paulo, São Carlos, 2018.

O *flutter* de painel é um fenômeno aeroelástico que pode lavar a falhas veículos aeroespaciais operando em velocidades supersônicas. Uma modelagem confiável do fenômeno é crucial para prever de maneira segura a vida útil de revestimentos aeronáuticos, sendo, portanto, de grande importância para o projeto de estruturas aeroespaciais. A maioria dos trabalhos publicados sobre este tema trata cada painel como uma estrutura isolada. Na realidade, entretanto, revestimentos aeronáuticos são tipicamente compostos por grandes painéis montados sobre longarinas, *stringers* e outros elementos de reforço. A presença destes elementos acaba subdividindo o painel em múltiplas células menores capazes de interagir durante o *flutter* – tornando, com isso, o movimento aeroelástico potencialmente mais complexo e perigoso. Ademais, reforçadores também são estruturas deformáveis, que, portanto, participam da dinâmica do problema. Neste contexto, o presente trabalho trata do estudo e implementação de um modelo computacional em elementos finitos para análise de *flutter* em painéis reforçados. Emprega-se uma combinação do modelo de placa de Mindlin com o modelo de viga de Timoshenko, incluindo não-linearidade geométrica. O modelo e as análises abordam tanto painéis isotrópicos quanto laminados. A aerodinâmica é simulada pela teoria de pistão, adequada para escoamentos alto-supersônicos. As equações de energia são discretizadas pelo Método dos Elementos Finitos, resultando em equações de movimento que são resolvidas no domínio do tempo por meio de um método de Newmark iterativo. O código final é verificado via comparação com soluções numéricas encontradas na literatura. Em termos de análises, este trabalho foca em três aspectos, com o objetivo de preencher uma lacuna da literatura específica: a) Investigar como reforçadores comportam-se durante o *flutter*, do ponto de vista dinâmico, e como sua vibração afeta o movimento aeroelástico como um todo; b) Estudar a influência da geometria dos reforçadores sobre tais efeitos; e c) Avaliar as imprecisões do modelo de painel isolado por meio de uma comparação sistemática entre os resultados deste modelo e aqueles gerados pela presente abordagem multi-célula. Resultados revelam novos fenômenos aeoelásticos oriundos da modelagem dos reforçadores como elementos estruturais flexíveis. Ademais, demonstra-se que a popular hipótese de fixação ideal pode ser altamente não conservadora no que diz respeito à condição crítica de *flutter* e à intensidade das vibrações.

Palavras-chave: Estruturas aeroespaciais. *Flutter* de painel. Aeroelasticidade não linear. Método dos elementos finitos. Placa reforçada. Viga de Timoshenko não linear.

LIST OF FIGURES

LIST OF TABLES

LIST OF ABBREVIATIONS AND ACRONYMS

FEM   Finite Element Method

FE   Finite element

CFD   Computational Fluid Dynamics

DOF   Degree of freedom

LCO   Limit cycle oscillation

ODE   Ordinary differential equation

PVW   Principle of Virtual Works

LIST OF SYMBOLS

$\mathbf{A}$	Plate in-plane (membrane) matrix
A_b	Stiffener cross-sectional area
b	Stiffener width
$\mathbf{B}$	Plate coupling (bending-membrane) matrix
$\mathbf{B}_m, \mathbf{B}_\theta$	Shape function derivative matrices
$\mathbf{B}_c$	Shape function matrix
c	Stiffener height
$\mathbf{C}$	Plate shear (transverse) matrix
$\tilde{\mathbf{C}}$	Uncorrected shear matrix
$\mathbf{c}_a$	Normalised elemental aerodynamic damping matrix
C_b	Constitutive constant from generalised beam theory
D	Reference flexural stiffness
$\mathbf{D}$	Plate bending matrix
e	Stiffener eccentricity
$\bar{E}$	Dimensionless mechanical energy
E_b	Beam Young's modulus
E_m	Mechanical energy stored in the structure
$\mathbf{f}$	Elemental force vector
$\mathbf{G}$	Global damping matrix
g_a	Dimensionless aerodynamic damping coefficient
G_b	Beam shear modulus
h	Panel height
$\mathbf{H}$	Nonlinear stiffness matrix
I_t	Polar moment of inertia for an eccentric beam

I_y	Moment of inertia for an eccentric beam
$\hat{K}$	Modified stiffness matrix
K_0	Global zeroth-order stiffness matrix
k_0^b	Elemental zeroth-order stiffness matrix (beam)
k_0^p	Elemental zeroth-order stiffness matrix (plate)
K_1	Global first-order stiffness matrix
k_1, k_2	Plate shear correction factors
k_1^b	Elemental first-order stiffness matrix (beam)
k_1^p	Elemental first-order stiffness matrix (plate)
K_2	Global second-order stiffness matrix
k_2^b	Elemental second-order stiffness matrix (beam)
k_2^p	Elemental second-order stiffness matrix (plate)
k_a	Normalised elemental aerodynamic stiffness matrix
k_A	Elemental in-plane stiffness matrix
k_b	Beam shear correction factor
k_B	Elemental coupling stiffness matrix
k_C	Elemental shear stiffness matrix
k_D	Elemental bending stiffness matrix
L	Panel width, stiffener length
M	Mach number
m^p	Elemental mass matrix (plate)
m_x, m_y, m_z	Auxiliary mass matrices
N_i	Plate shape function related to the i-th elemental node
N_i^b	Beam shape function related to the i-th elemental node
N_u, N_v, N_w	Plate shape function vectors
N_u^p, N_v^p, N_w^p	Beam shape function vectors

$\mathbf{\hat{P}}$	Modified force vector
p_0	Arbitrary external pressure (step load)
q	Free-stream dynamic pressure
$\mathbf{Q}_p$	Plate in-plane constitutive matrix
$\mathbf{Q}_s$	Plate shear constitutive matrix
u	Plate displacement in the x direction
u_b	Beam displacement in the x direction
$\mathbf{u}$	Elemental DOF vector
$\mathbf{u}_m$	Elemental membrane DOF vector (plate)
$\mathbf{u}_m^b$	Elemental membrane DOF vector (beam)
$\mathbf{u}_w$	Elemental transverse DOF vector (plate)
$\mathbf{u}_w^b$	Elemental transverse DOF vector (beam)
$\mathbf{u}_\phi$	Elemental bending DOF vector (plate)
$\mathbf{u}_\phi^b$	Elemental bending DOF vector (beam)
$\mathbf{U}$	Global DOF vector
$\hat{u}, \hat{v}, \hat{w}$	Midsurface displacements
v	Plate displacement in the y direction
v_b	Beam displacement in the y direction
w	Plate displacement in the z direction
w_b	Beam displacement in the z direction
w_c	Central transverse displacement
(y', z')	Local stiffener coordinates
α	Beam height-to-width ratio
γ_{xy}, γ_{xz}	Shear strains (beam)
δ	Variational operator
δW	Generic virtual work

δW_{int}^e	Virtual internal work within a plate element
Δp	Pressure difference (lower-upper surface)
Δt	Time step
$\Delta x, \Delta y$	Element sizes
$\overline{\Delta x}$	Minimum element size
ε_p	Plate in-plane (membrane) strain
ε_s	Plate shear strain
ε_x	Beam axial strain
ε_θ	Nonlinear plate strain
θ_k	Layer-wise fiber orientation angle
Θ	Plate slope matrix
κ	Plate bending strain
λ	Dimensionless dynamic pressure
λ_f	Critical dimensionless dynamic pressure
μ	Flow-panel mass ratio
ν_b	Beam Poisson's ratio
ρ	Plate density
ρ_b	Beam density
ρ_∞	Free-stream flow density
τ	Dimensionless time
τ_{xy}	Beam shear stress
ϕ_x, ϕ_y	Midsurface normal rotations
ω_0	Reference frequency
Ω_e	Elemental domain (plate elements)
Ω_{ref}	Reference integration domain

CONTENTS

1 INTRODUCTION

Around the middle of the 20th century, structural failures in the metallic skin of experimental aircrafts and space launch vehicles drew the attention of the aerospace community to aeroelastic problems involving skin panels (DOWELL, 1975). The physical phenomena responsible for causing such failures were given the generic name of *panel flutter*, which is a type of aeroelastic instability that can affect plates and shells immersed in high-speed flows, tipically during supersonic flight. It is a fluid-structure interaction problem: the flow produces a pressure field that deforms the panel, whose new (deformed) shape modifies the pressure distribution. This process continues cyclically, resulting in a self-excited oscillatory motion that can lead the panel to fatigue rupture. In that context, inummerous scientific works were conducted in the 1960s to address panel flutter (DOWELL, 1970). This aeroelastic phenomenon is still under intense investigation, with tens or perhaps hundreds of articles being published every year worldwide.

This chapter addresses the historical development of the mathematical models used for studying panel flutter, as well as the evolution of aeroelastic modelling for reinforced (stiffened) panels, which are the main object of study of the present work. The importance of reliable simulation of stiffener behaviour for proper aeroelastic design is highlighted.

1.1 The evolution of panel flutter modelling

Due to the elevated cost and complexity demanded by supersonic and hypersonic aeroelastic experiments, panel flutter has always been studied primarily via mathematical models. According to Dowell (1970), the first analytical methods conceived for studying the problem were based on linear aeroelastic models, using the principle of modal superposition for the assessment of flutter eigen-modes. In general, an aeroelastic model is composed of two essential elements: an aerodynamic model and a structural model. The latter usually simulates a structure of engineering interest – e.g., aircraft skin, wings, tails, etc – and the former accounts for the forces loading such structural element. There exist a myriad of different approaches and theories for addressing both fields. Selecting which to adopt depends upon the task at hand, resource availability and, especially, the specific goals of a project or study.

1.1.1 Aerodynamic modelling

The oldest and still most popular aerodynamic model used for panel flutter analysis is the first-order piston theory, whose applicability to supersonic panel flutter was perhaps first suggested by Ashley and Zartarian (1956). It is an extremely simple model derived from supersonic potential flow theory by dropping convolution and nonlinear terms. The

resulting linear model computes the pressure at a given point over the panel directly from its local slope and normal velocity. The conception of this model was the first step towards making analytical panel flutter modelling viable, which in turn caused a no-number of scientific publications to emerge in the following years. Comparison between experiments and theory showed that the piston theory provides reasonably accurate estimates for the pressure field in supersonic regimes (MEI; ABDEL-MOTAGALY; CHEN, 1999).

A few years later, Cunningham (1963) and Dowell (1966a) devised more complex aerodynamic models based on linearised supersonic potential theory. Such methods are considerably more intricate than piston theory, having multiple integrals of nonlinear, complex mathematical functions, and being strongly based upon assumed vibration modes and frequencies. Their use is required for low-supersonic Mach numbers, say, $1.0 < M < 1.5$. Dowell (1971) enhanced the model by introducing boundary layer effects based on shear flow theory. He then concluded that, for low Mach numbers, shear velocity profiles can greatly influence the aeroelastic response of fluttering panels. Recently, Vedeneev (2012) and Shitov and Vedeneev (2017) compared the flutter boundaries computed through potential flow theory with those obtained through linear piston theory, and concluded that the latter yields satisfactory results for high-supersonic regimes, say, $M > 1.7$.

An even higher-fidelity approach is to solve the Euler or Navier-Stokes equations of gas dynamics, thereby creating the generically called CFD-based methods. These methods have the important downside of requiring the use of fluid meshes, which makes their computational performance lower – by orders of magnitude – than that of potential flow methods. Bein et al. (1993) compared hypersonic panel flutter results obtained from an Euler solver with those attained through first-, second- and third-order piston theories. They concluded that the piston theory approximations for the pressure distribution over the panel are generally satisfactory. Recently, Alder (2015) compared piston-theory panel flutter with a finite-volume-based Euler solver. He then confirmed the validity of linear piston theory for studying both the stability boundary and the post-flutter response of panels in high-supersonic flight.

For the reasons briefly exposed here, the linear piston theory has been chosen for the present work. As demonstrated further on in chapter 2, it allows easy implementation into any pre-existing finite element structural solver and dismisses the need for fluid meshes, whilst maintaining sufficient accuracy for high-supersonic panel flutter investigation. It is, thus, an extremely efficient tool for optimisation and parametric studies, in which the generation of large amounts of result data is required.

1.1.2 Structural modelling

The dissemination of finite-element- and finite-difference-based computational methods made it possible to study panel flutter with diverse geometries, loads and materials

(BISMARCK-NASR, 1992). Such diversification of spatial discretisation methods fomented the evolution of the structural models employed for studying panel flutter. Dowell (1966b) combined von Karman's geometrical non-linearity with the classical Kirchhoff plate theory, using Galerking's method for discretisation. This allowed the reproduction of limit cycle oscillations (LCOs), which are periodic aeroelastic motions with limited amplitudes. Shortly after that, Dowell (1969) enhanced the model again by considering curved panel geometries. Sawyer (1977), also using Galerkin's method, investigated the aeroelastic behaviour of composite panels including buckling effects, and studied the influence of fiber orientaion, lamination sequence and in-plane load magnitude on the flutter boundary (stability limit). Bismarck-Nasr (1976) applied the Finite Element Method (FEM) to supersonic flutter analysis of cylindrical panels. Also using the FEM, Mei (1977) discretised von Karman's equations for infinite-span plates, aiming to study nonlinear flutter motion. In the years that followed, a myriad of works adressing improvements and applications of the FEM for panel flutter were published (CHEN; LIN, 1985; KUO-JIUN; PONG-JEU; JIANN-QUO, 1989; SARMA; VARADAN, 1988; SUNDER; RAMAKRISHNAN; SENGUPTA, 1983).

In the 1990s, iterative algorithms that dismissed the need for time integration became popular (DIXON; MEI, 1993; MEI; ABDEL-MOTAGALY; CHEN, 1999; SHORE; MEI; GRAY, 1991; XUE; MEI, 1993a; XUE; MEI, 1993b). With the aid of such algorithms, and also owing to the increase of computer processing capacity, detailed study of nonlinear aeroelastic regimes was made properly viable. Then, the focus of panel flutter investigation shifted from flutter onset prediction – which is typically linear – to the analysis of post-flutter (nonlinear) regimes, in which LCOs are observed. Such cyclic motions can present potentially large amplitudes and frequencies, which can drive wing and fuselage skin towards fatigue failure. Xue and Mei (1993a) categorically demonstrated the importance of studying the nonlinear regime by quantitatively assessing the fatigue life of limit-cycling panels. They showed that it is possible to design the skin in such a way that the panels operate in "infinite life" regime, whilst allowing flutter to happen. Therefore, it was demonstrated that panels designed to completely suppress the occurrence of flutter (instead of withstanding it) tend to be overdesigned.

Parallelly, FEM structural modelling was also being improved with respect to plate kinematics. In the 1990s, many aeroelasticians started to adopt the Mindlin kinematic assumptions instead of the Kirchhoff-Love classical thin plate theory. Differently from classical theory, Mindlin's assumptions do not require that transverse shear deformability be neglected. Therefore, this model is not restricted to thin panels, being also adequate for representing the behaviour of moderately thick plates. Abdel-Motagaly, Duan and Mei (1999) employed Mindlin's theory, coupled with von Karman's geometrical non-linearity, to study flutter on acoustically excited panels. Lee (1999) and Oh, Lee and Lee (2001) also used the Mindlin-von Karman model for the panels, coupled with the Timoshenko beam theory to represent stiffeners. Marques, Natarajan and Ferreira (2017) used Mindlin's formulation

for laminated panels, aiming at the aeroelastic tailoring of layers for increasing critical flutter speeds. In the present work, the finite element computational model represents the panel as a nonlinear Mindlin-von Karman plate. The panel flutter problem is tackled considering isotropic and laminated panels, which have become a competitive trend in the aerospace industry in the last decades. Furthermore, the role of stiffening elements – such as stringers, longerons and frames – is included in the model by considering one-dimensional nonlinear beams coupled to the panel's lower surface.

1.2 Flutter in reinforced panels

The study of flutter in stiffened panels is of great practical interest, since aircraft skin is typically built of thin-walled panels fixed on top of more robust structural elements such as ribs and stiffeners (CARRERA; ZAPPINO; PETROLO, 2013). Figure 1 shows an aircraft fuselage from inside, where multiple stiffeners can be seen underneath the skin. Liao and Sun (1993) used linear Timoshenko beam theory to simulate the stiffeners underneath laminated panels, in order to study the influence of lamination sequence and stiffener number on the flutter boundary. Lee (1999) and Oh, Lee and Lee (2001) enhanced the model by adding geometrical non-linearity and thermal loading. Zhao and Cao (2013) studied the effects of stiffener geometry and distribution, modelling the stiffeners as Euler-Bernoulli beams. Castro et al. (2016) analysed the aeroelastic behaviour of curved panels via a semi-analytical model that considered only the stiffener's base as a structural element. Fernandes and Tamijani (2017) devised an aeroelastic model with curvilinear stiffeners and showed that such unconventional geometric feature can be explored for efficient flutter supression.

In most of these works, the analyses were focused on the effects of stiffener addition on the panel's aeroelastic behaviour. In other words, the comparison is always drawn between the original (unstiffened) panel and the *same* panel with one or more stiffeners. It seems somewhat natural to expect a panel to have its flutter characteristics (critical speed, LCO amplitudes, etc) improved by the addition of stiffeners. A different standpoint to be explored – instead of studying the same panel with and without stiffeners – is to compare each cell (bay) in the reinforced panel with an individual (isolated) panel with the same dimensions, as illustrated in Figure 2. By doing so, this approach aims to study the effects of the structural coupling between the multiple cells in a panel, rather than to quantify the additional reinforcement brought by stiffeners.

Such "multi-panel" approach was first performed in the 1960s by Dowell (1964) and Rodden (1964), who used linear aeroelastic models for predicting the stability boundary of sets of coupled panels. In their approach, also known as *multibay analysis*, the stiffeners were modelled as simple supports positioned between the subpanels. At that time, limited by the restrictions of linear modelling, the general conclusion reached by authors who

Figure 1 – Typical fuselage skin with multiple stiffening elements.
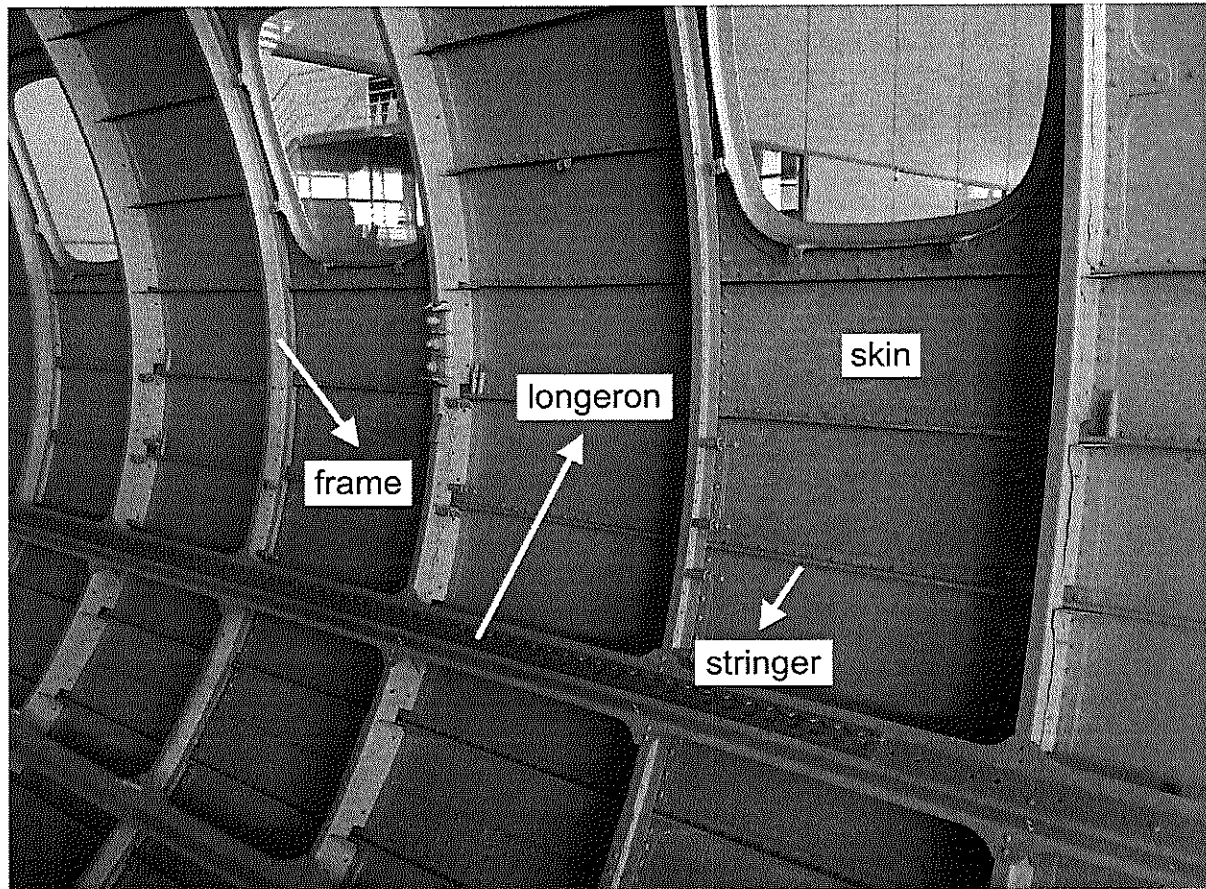
Source: Elaborated by the author.

investigated multibay panel flutter was that panels with multiple cells possess critical flutter speeds that are very similar to those of single-celled panels (DOWELL, 1964; LOCK; FARKAS, 1965). Probably for that reason, literature on multibay panel flutter remained incipient for decades. To the best of the author's knowledge, only a handful of papers were published on this subject for over fifty years (MUKHERJEE; PARTHAN, 1995; PANY; PARTHAN, 2003; SHIAU; CHANG, 1991), all of which stuck, once again, to linear flutter prediction. In order to fill an existing gap, the author of the present work has recently investigated the multibay problem from a post-flutter standpoint, using a nonlinear aeroelastic model. The study has revealed that the nonlinear structural coupling between adjacent bays during LCOs can strongly influence the flutter mechanism and the motion amplitudes. They showed that, depending on the relative vibration phase between the cells, the maximum LCO amplitudes of a multibay panel can be several times larger than that which each cell would undergo if vibrating isolatedly (PACHECO et al., 2017; PACHECO; MARQUES; FERREIRA, 2017). It has been thereby demonstrated that idealising skin structures as individual panels – as done in the vast majority of works

Figure 2 – Schematic representation of a single panel and a four-cell reinforced panel.

Reinforced panel   Isolated panel
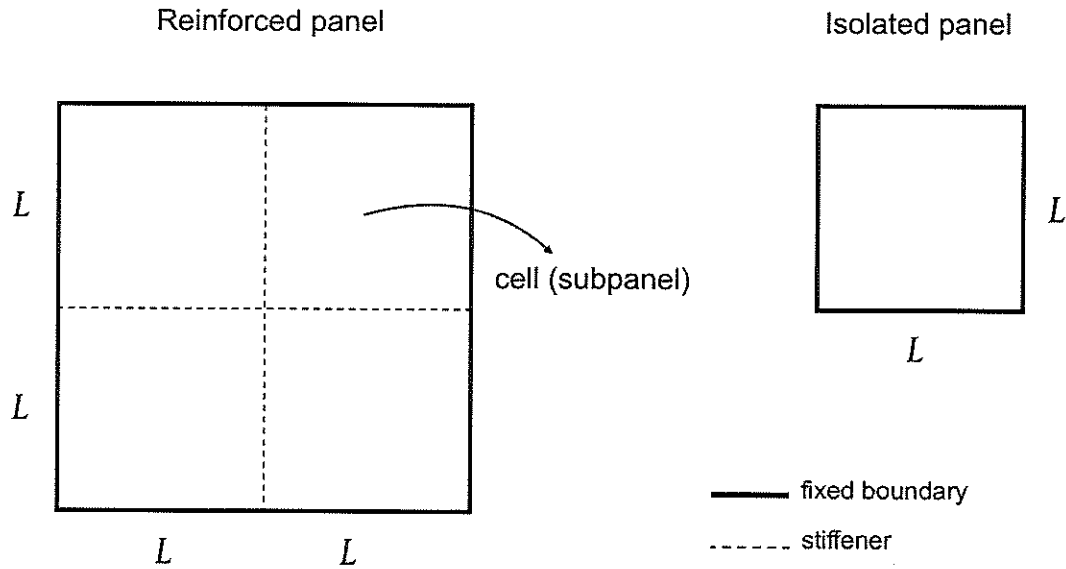
Source: Elaborated by the author.

published on panel flutter – can be unsafe from the perspective of structural integrity. Yet, the multibay approach still presents a considerable level of structural idealisation as it models stiffeners as simple supports, which have infinite translational stiffness and zero torsional stiffness. In reality, stiffeners are deformable structural elements, which are thus subject to a certain degree of transverse translation, whilst imposing considerable resistence to the local rotation of the panel.

This Masters project proposes a higher-fidelity methodology for addressing the problem of multi-celled (reinforced) panels. The stiffeners are modelled as nonlinear Timoshenko beams, and the panels (isotropic or laminated) as nonlinear Mindlin plates. The approach used for the aerodynamic load is rather classical: the first-order piston theory, which is suitable for high-supersonic flows. The energy equations are discretised through the Finite Element Method, and the resulting aeroelastic equations of motion are solved directly in time by means of numerical time-marching.

1.3 Objectives

High-speed flight imposes several challenges to the design of aerospace structures. Some examples are panel flutter, diverse types of shock-related performance loss, and extreme temperatures caused by friction with air particles. In order for commercial supersonic flight – interrupted since 2003, when the last *Concorde* airplanes ceased to operate – to reemerge, advances are required in analysis, design and modelling. In this context, one of the multiphysical phenomena that have been getting substantial attention

from the scientific community lately is panel flutter, as aerospace skin panels can undergo large-amplitude, high-frequency aeroelastic oscillations during supersonic flight. Such intense cycling can lead to fatigue rupture after hours of flight operation. Therefore, a quantitatively accurate description of such oscillations is crucial for safely estimating the lifespan of aerospace structures. For this reason, reliable modelling of the panel flutter phenomenon is essential for aerospace structural design. Moreover, aircraft skin is usually built in the form of large panels mounted and fixed on stiffeners, thereby dividing the panel into multiple cells which are structurally coupled. In this context, the present research project proposes the implementation and validation of a finite element aeroelastic model for aircraft skin panels being reinforced by beams. By conducting a systematic comparative analysis in which the aeroelastic response of coupled panels is confronted with that of single panels, this project aims to fill a gap in the panel flutter scientific literature. The purpose here is not to propose a definitive model for reinforced skin. Rather than this, the goal is to take one step further in modelling – by considering double instead of single panels – in order to identify potential sources of inaccuracy in the classical panel flutter model. Furthermore, the inclusion of composite material behaviour into the model has the goal of making the present methodology compatible with the growing trend of the aerospace industry to employ this type of efficient materials in aircraft design.

2 AEROELASTIC MODEL

2.1 Introduction

The computational aeroelastic model proposed here for studying flutter in reinforced panels consists of two basic elements: an aerodynamic model and a nonlinear structural model. The latter is composed of a plate model for the panel, a beam model for the stiffener and, of course, a proper coupling between them. Figure 3 illustrates the problem setup and the typical coordinate system adopted. All the parts of the model are combined by the Principle of Virtual Work (PVW), whose mathematical statement is discretised through the Finite Element Method (FEM).

Figure 3 – Panel flutter problem setup.
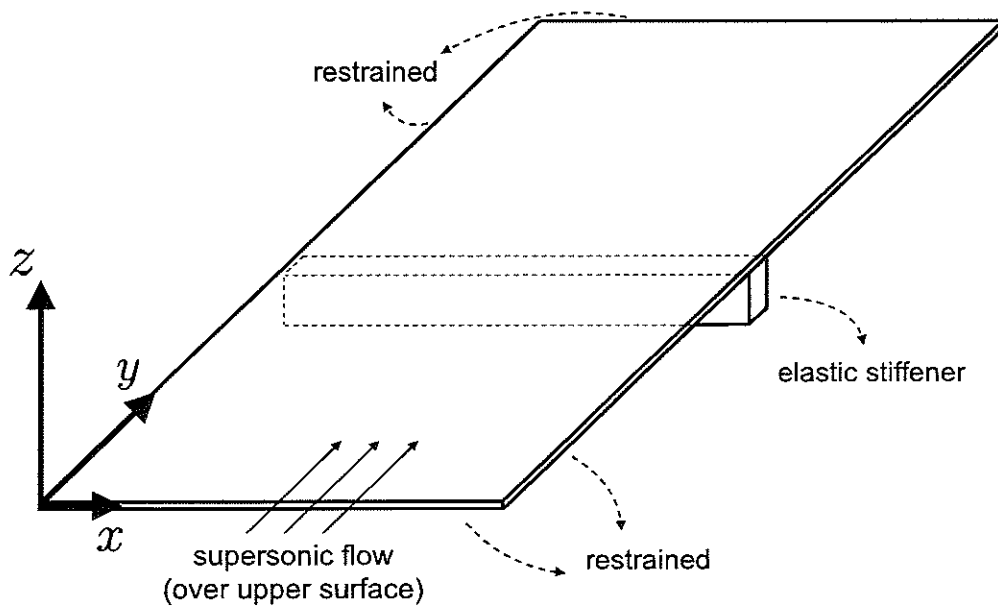
Source: Elaborated by the author.

The following subsections deal with the detailed derivation of the aeroelastic model, from physical energy principles to the resulting computational model. First, the plate model is addressed, followed by the derivation of the beam model, which is coupled with the former in order to produce the stiffened (reinforced) panel structural model. Then, the aerodynamic theory is described and mathematically combined with the structural equations, thereby resulting in the aeroelastic model. Finally, the numerical schemes used for solving the aeroelastic equations are addressed.

2.2 The nonlinear Mindlin plate

The Mindlin kinematic theory is an evolution of classical plate theory that considers transverse shear deformability. The Mindlin assumptions do not require that normals to the midsurface remain normal after deformation. For this reason, it is capable of reproducing the kinematics of moderately thick panels. In a Mindlin plate, the displacement field at a point (x, y, z) and a time t is (PICA; WOOD; HINTON, 1980)

$$u(x, y, z, t) = \hat{u}(x, y, t) - z\phi_x(x, y, t), \tag{2.1}$$

$$v(x, y, z, t) = \hat{v}(x, y, t) - z\phi_y(x, y, t), \tag{2.2}$$

$$w(x, y, z, t) = \hat{w}(x, y, t), \tag{2.3}$$

in which u, v and w are the displacements in the x, y and z directions, respectively, and the symbol ($\hat{\ }$) indicates midsurface ($z = 0$) displacements. The quantities ϕ_x and ϕ_y are the rotation of the normals about the y and x axes, respectively. Note that such rotation degrees of freedom are independent on the translational displacements, whereas classical plate theory states that $\phi_x = \frac{\partial w}{\partial x}$ and $\phi_y = \frac{\partial w}{\partial y}$. In the present model those relations are not imposed, but will be observed (approximately) whenever plate thickness, h, is much smaller than the lateral dimensions. The Mindlin theory can be coupled with the von Karman nonlinear strain-displacement relations so that the resulting strucutural model is able to account for geometrical non-linearities arising from large-displacement motion. The relevant entries of the strain tensor for a Minlin-von Karman plate can be organised in a vector as (PICA; WOOD; HINTON, 1980)

$$\varepsilon = \begin{Bmatrix} \varepsilon_x \\ \varepsilon_y \\ \gamma_{xy} \\ \gamma_{xz} \\ \gamma_{yz} \end{Bmatrix} = \begin{Bmatrix} \frac{\partial \hat{u}}{\partial x} \\ \frac{\partial \hat{v}}{\partial y} \\ \frac{\partial \hat{u}}{\partial y} + \frac{\partial \hat{v}}{\partial x} \\ \frac{\partial \hat{w}}{\partial x} - \phi_x \\ \frac{\partial \hat{w}}{\partial y} - \phi_y \end{Bmatrix} - z \begin{Bmatrix} \frac{\partial \phi_x}{\partial x} \\ \frac{\partial \phi_y}{\partial y} \\ \frac{\partial \phi_x}{\partial y} + \frac{\partial \phi_y}{\partial x} \\ 0 \\ 0 \end{Bmatrix} + \begin{Bmatrix} \frac{1}{2}\left(\frac{\partial \hat{w}}{\partial x}\right)^2 \\ \frac{1}{2}\left(\frac{\partial \hat{w}}{\partial y}\right)^2 \\ \frac{\partial \hat{w}}{\partial x}\frac{\partial \hat{w}}{\partial y} \\ 0 \\ 0 \end{Bmatrix}, \tag{2.4}$$

in which the last term, quadratic with respect to $\hat{w}$, is the von Karman strain. Note that this model assumes uniform transverse shear (γ_{xz} and γ_{yz}) along the thickness. Such assumed distribution is not physically true, though, since γ_{xz} and γ_{yz} are known to vanish at the upper and lower surfaces, whilst having nonzero values in between. In order to compensate for such inconsistency, the classical approach is to introduce shear correction factors. These coefficients are applied to the transverse-shear strain energy so as to promote energetic equivalence between the real distribution and the assumed one. For isotropic plates, the correction factors are usually taken as 5/6, whereas for composite panels they depend on the lamination scheme (WHITNEY, 1973). The methodology for addressing shear correction is discussed in subsection 2.2.2, although it is not of the greatest relevance to the present work, which focuses on thin panels.

The stresses are obtained by applying the proper constitutive relations to the strains. For a Mindlin plate, the in-plane and out-of-plane (transverse) quantities are constitutively uncoupled. For this reason, it is more pratical to separate the plate strain into in-plane strain, ε_p, and transverse shear strain, ε_s:

$$\varepsilon_p = \begin{Bmatrix} \varepsilon_x \\ \varepsilon_y \\ \gamma_{xy} \end{Bmatrix} = \begin{Bmatrix} \frac{\partial \hat{u}}{\partial x} \\ \frac{\partial \hat{v}}{\partial y} \\ \frac{\partial \hat{u}}{\partial y} + \frac{\partial \hat{v}}{\partial x} \end{Bmatrix} + z \begin{Bmatrix} -\frac{\partial \phi_x}{\partial x} \\ -\frac{\partial \phi_y}{\partial y} \\ -\frac{\partial \phi_x}{\partial y} - \frac{\partial \phi_y}{\partial x} \end{Bmatrix} + \begin{Bmatrix} \frac{1}{2}\left(\frac{\partial \hat{w}}{\partial x}\right)^2 \\ \frac{1}{2}\left(\frac{\partial \hat{w}}{\partial y}\right)^2 \\ \frac{\partial \hat{w}}{\partial x}\frac{\partial \hat{w}}{\partial y} \end{Bmatrix} = \varepsilon_m + z\kappa + \varepsilon_\theta, \qquad (2.5)$$

and

$$\varepsilon_s = \begin{Bmatrix} \gamma_{xz} \\ \gamma_{yz} \end{Bmatrix} = \begin{Bmatrix} \frac{\partial \hat{w}}{\partial x} - \phi_x \\ \frac{\partial \hat{w}}{\partial y} - \phi_y \end{Bmatrix}. \qquad (2.6)$$

Note that the in-plane strain is split into ε_m, $z\kappa$ and ε_θ, which are the membrane, bending and nonlinear strains, respectively. The corresponding in-plane and transverse stresses are

$$\sigma_p = \bar{\mathbf{Q}}_p \varepsilon_p \quad \text{and} \quad \sigma_s = \bar{\mathbf{Q}}_s \varepsilon_s, \qquad (2.7)$$

in which $\bar{\mathbf{Q}}_p$ and $\bar{\mathbf{Q}}_s$ are the constitutive matrices with respect to the (x, y, z) system. The computation of these matrices is addressed in subsection 2.2.2.

The stresses and strains are combined by the Principle of Virtual Work, which states an equality between the virtual works done by internal and external forces. The internal work is computed as the strain energy variation caused by the stress field acting over a virtual strain field:

$$\delta W_{\text{int}} = \int_V \left(\sigma_p{}^T \delta\varepsilon_p + \sigma_s{}^T \delta\varepsilon_s \right) \mathrm{d}V, \qquad (2.8)$$

with the variational operator, δ, indicating virtual quantities. Upon substitution of the constitutive equations, the virtual strain energy becomes

$$\delta W_{\text{int}} = \int_V \left(\delta\varepsilon_p{}^T \bar{\mathbf{Q}}_p \varepsilon_p + \delta\varepsilon_s{}^T \bar{\mathbf{Q}}_s \varepsilon_s \right) \mathrm{d}V. \qquad (2.9)$$

The infinitesimal volume can by factored into a thickness differential and a surface differencial: $\mathrm{d}V = \mathrm{d}z\mathrm{d}A$. Moreover, the in-plane strain can be split into $\varepsilon_0 + z\kappa$, in which $\varepsilon_0 = \varepsilon_m + \varepsilon_\theta$ is the midsurface strain. So, the internal work can be written as

$$\delta W_{\text{int}} = \int_A \int_{-\frac{h}{2}}^{\frac{h}{2}} \left[(\delta\varepsilon_0 + z\delta\kappa)^T \bar{\mathbf{Q}}_p (\varepsilon_0 + z\kappa) + \delta\varepsilon_s{}^T \bar{\mathbf{Q}}_s \varepsilon_s \right] \mathrm{d}z\mathrm{d}A. \qquad (2.10)$$

After expanding the products and performing the integration along the thickness, Eq. (2.10) becomes

$$\delta W_{\text{int}} = \int_A \left(\delta\varepsilon_0{}^T \mathbf{A}\varepsilon_0 + \delta\varepsilon_0{}^T \mathbf{B}\kappa + \delta\kappa^T \mathbf{B}\varepsilon_0 + \delta\kappa^T \mathbf{D}\kappa + \delta\varepsilon_s{}^T \mathbf{C}\varepsilon_s \right) \mathrm{d}A, \qquad (2.11)$$

in which

$$(\mathbf{A}, \mathbf{B}, \mathbf{D}) = \int_{-\frac{h}{2}}^{\frac{h}{2}} \left(1, z, z^2 \right) \bar{\mathbf{Q}}_p \, \mathrm{d}z, \qquad (2.12)$$

and $\mathbf{C}$ is a function of $\tilde{\mathbf{C}}$, which is calculated as

$$\tilde{\mathbf{C}} = \int_{-\frac{h}{2}}^{\frac{h}{2}} \bar{\mathbf{Q}}_s \mathrm{d}z.$$ (2.13)

The detailed expressions for such matrices are given in subsection 2.2.2.

The external work will generally have two sets contributions. One coming from an external load field and another one coming from the inertial forces due to the plate's acceleration field:

$$\delta W_{\text{ext}} = \int_A \delta w \Delta p \ \mathrm{d}A \ - \ \int_V \rho \left(\delta u \frac{\partial^2 u}{\partial t^2} + \delta v \frac{\partial^2 v}{\partial t^2} + \delta w \frac{\partial^2 w}{\partial t^2} \right) \mathrm{d}V,$$ (2.14)

in which ρ is the material density. For now, the pressure field, Δp, is assumed to be arbitrary and independent upon the displacement field. Yet, in the final aeroelastic model, the pressure shall be calculated from the aerodynamic model as a function of $\hat{w}$.

The next step is to substitute the plate displacement fields (Eqs. (2.1) - (2.3)) into Eq. (2.14), which after integration along the thickness yields

$$\delta W_{\text{ext}} = \int_A \delta \hat{w} \Delta p - \rho \left[h \left(\delta \hat{u} \frac{\partial^2 \hat{u}}{\partial t^2} + \delta \hat{v} \frac{\partial^2 \hat{v}}{\partial t^2} + \delta \hat{w} \frac{\partial^2 \hat{w}}{\partial t^2} \right) + \frac{h^3}{12} \left(\delta \phi_x \frac{\partial^2 \phi_x}{\partial t^2} + \delta \phi_y \frac{\partial^2 \phi_y}{\partial t^2} \right) \right] \mathrm{d}A.$$ (2.15)

The PVW complements Eqs. (2.10) and (2.15) by stating that $\delta W_{\text{int}} = \delta W_{\text{ext}}$. Nevertheless, in order to proceed with the formulation, a discretisation technique is required. In the present work, the Finite Element Method is employed for such purpose. By introducing the FEM formulation into the PVW, it is possible to extract the equations of motion from the energy equations.

2.2.1 Finite element formulation

In this work, a classical finite element formulation is employed for discretising the PVW. The four-node lagrangian quadrilateral element is chosen for composing the mesh. Each node has five degrees of freedom (DOFs): $\hat{u}$, $\hat{v}$, $\hat{w}$, ϕ_x and ϕ_y, which for convenience and computational efficiency are grouped in: membrane DOFs, $(\hat{u}, \hat{v})$, transverse DOF, $\hat{w}$, and rotation DOFs, (ϕ_x, ϕ_y). Hence, the elemental DOF vector can be written as

$$\mathbf{u} = \begin{Bmatrix} \mathbf{u}_m \\ \mathbf{u}_w \\ \mathbf{u}_\phi \end{Bmatrix},$$ (2.16)

with

$$\mathbf{u}_m = \left\{ u_1 \ \ v_1 \ \ u_2 \ \ v_2 \ \ u_3 \ \ v_3 \ \ u_4 \ \ v_4 \right\}^T,$$ (2.17)

$$\mathbf{u}_w = \left\{ w_1 \ \ w_2 \ \ w_3 \ \ w_4 \right\}^T,$$ (2.18)

$$\mathbf{u}_\phi = \left\{ \phi_{x1} \ \ \phi_{y1} \ \ \phi_{x2} \ \ \phi_{y2} \ \ \phi_{x3} \ \ \phi_{y3} \ \ \phi_{x4} \ \ \phi_{y4} \right\}^T,$$ (2.19)

in which indices 1 through 4 refer to the elemental nodes. Figure 4 shows the finite element and the node numbering adopted. Observe that node 1 is brought to the origin, which is standard procedure to simplify explicit shape function calculation.

Figure 4 – Standard four-node rectangular finite element.
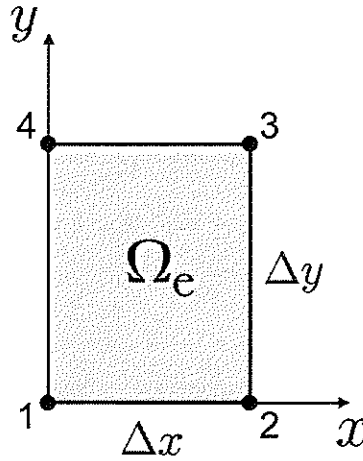
Source: Elaborated by the author.

Each node has an associated shape function. The i-th nodal shape function has the following property: it takes value 1 at node i, and value 0 at the remaining nodes. Mathematically:

$$N_i(x_j, y_j) = \begin{cases} 1, & \text{if } j = i, \\ 0, & \text{if } j \neq i. \end{cases} \tag{2.20}$$

Since $j = 1, 2, 3, 4$, Eq. (2.20) provides four equations for each shape funcion. Thus, it is possible to generate bilinear functions of the form $N_i(x, y) = a_i x + b_i y + c_i xy + d_i$. Upon substituting Eq. (2.20) into this general bilinear polynomial, the following shape functions are obtained:

$$N_1(x, y) = 1 - \frac{x}{\Delta x} - \frac{y}{\Delta y} + \frac{xy}{\Delta x \Delta y}, \tag{2.21}$$

$$N_2(x, y) = \frac{x}{\Delta x} - \frac{xy}{\Delta x \Delta y}, \tag{2.22}$$

$$N_3(x, y) = \frac{xy}{\Delta x \Delta y}, \tag{2.23}$$

$$N_4(x, y) = \frac{y}{\Delta y} - \frac{xy}{\Delta x \Delta y}, \tag{2.24}$$

in which Δx and Δy are the element sizes. As a direct consequence of the definition of nodal functions (Eq. (2.20)), it is possible to approximate any displacement in terms of shape functions and the respective nodal values. For instance, the transverse displacement can be interpolated as

$$\hat{w}(x, y, t) = \sum_{i=1}^{4} N_i(x, y)\hat{w}_i(t). \tag{2.25}$$

Note that the shape functions do not depend upon t, so that the time dependence of any DOF occurs through the nodal values. Eq. (2.25) can be rearranged as

$$\hat{w} = \mathbf{N}_w{}^T \mathbf{u}_w, \tag{2.26}$$

in which $\mathbf{N}_w = \{N_1\ N_2\ N_3\ N_4\}^T$. The remaining DOFs can be written as

$$\hat{u} = \mathbf{N}_u{}^T \mathbf{u}_m, \tag{2.27}$$

$$\hat{v} = \mathbf{N}_v{}^T \mathbf{u}_m, \tag{2.28}$$

$$\phi_x = \mathbf{N}_u{}^T \mathbf{u}_\phi, \tag{2.29}$$

$$\phi_y = \mathbf{N}_v{}^T \mathbf{u}_\phi, \tag{2.30}$$

in which $\mathbf{N}_u = \{N_1\ 0\ N_2\ 0\ N_3\ 0\ N_4\ 0\}^T$ and $\mathbf{N}_v = \{0\ N_1\ 0\ N_2\ 0\ N_3\ 0\ N_4\}^T$. The next step is to write each of the strain components also in terms of nodal values and shape functions, and introduce the resulting discretised strains into the PVW.

Take the membrane strain ε_m, for instance. It can be written in discretised form as

$$\varepsilon_m = \left\{ \begin{array}{c} \frac{\partial \hat{u}}{\partial x} \\ \frac{\partial \hat{v}}{\partial y} \\ \frac{\partial \hat{u}}{\partial y} + \frac{\partial \hat{v}}{\partial x} \end{array} \right\} = \left\{ \begin{array}{c} \frac{\partial(\mathbf{N}_u{}^T \mathbf{u}_m)}{\partial x} \\ \frac{\partial(\mathbf{N}_v{}^T \mathbf{u}_m)}{\partial y} \\ \frac{\partial(\mathbf{N}_u{}^T \mathbf{u}_m)}{\partial y} + \frac{\partial(\mathbf{N}_v{}^T \mathbf{u}_m)}{\partial x} \end{array} \right\} = \left\{ \begin{array}{c} \frac{\partial \mathbf{N}_u{}^T}{\partial x} \\ \frac{\partial \mathbf{N}_v{}^T}{\partial y} \\ \frac{\partial \mathbf{N}_u{}^T}{\partial y} + \frac{\partial \mathbf{N}_v{}^T}{\partial x} \end{array} \right\} \mathbf{u}_m = \mathbf{B}_m \mathbf{u}_m, \tag{2.31}$$

in which

$$\mathbf{B}_m = \begin{bmatrix} \frac{\partial N_1}{\partial x} & 0 & \frac{\partial N_2}{\partial x} & 0 & \frac{\partial N_3}{\partial x} & 0 & \frac{\partial N_4}{\partial x} & 0 \\ 0 & \frac{\partial N_1}{\partial y} & 0 & \frac{\partial N_2}{\partial y} & 0 & \frac{\partial N_3}{\partial y} & 0 & \frac{\partial N_4}{\partial y} \\ \frac{\partial N_1}{\partial y} & \frac{\partial N_1}{\partial x} & \frac{\partial N_2}{\partial y} & \frac{\partial N_2}{\partial x} & \frac{\partial N_3}{\partial y} & \frac{\partial N_3}{\partial x} & \frac{\partial N_4}{\partial y} & \frac{\partial N_4}{\partial x} \end{bmatrix}. \tag{2.32}$$

Analogously, the bending vector, $\boldsymbol{\kappa}$, becomes simply

$$\boldsymbol{\kappa} = -\mathbf{B}_m \mathbf{u}_\phi. \tag{2.33}$$

The nonlinear strain, ε_θ, requires a little more manipulation:

$$\varepsilon_\theta = \left\{ \begin{array}{c} \frac{1}{2}\left(\frac{\partial \hat{w}}{\partial x}\right)^2 \\ \frac{1}{2}\left(\frac{\partial \hat{w}}{\partial y}\right)^2 \\ \frac{\partial \hat{w}}{\partial x}\frac{\partial \hat{w}}{\partial y} \end{array} \right\} = \frac{1}{2} \begin{bmatrix} \frac{\partial \hat{w}}{\partial x} & 0 \\ 0 & \frac{\partial \hat{w}}{\partial y} \\ \frac{\partial \hat{w}}{\partial y} & \frac{\partial \hat{w}}{\partial x} \end{bmatrix} \left\{ \begin{array}{c} \frac{\partial \hat{w}}{\partial x} \\ \frac{\partial \hat{w}}{\partial y} \end{array} \right\} = \frac{1}{2}\Theta \left\{ \begin{array}{c} \frac{\partial \hat{w}}{\partial x} \\ \frac{\partial \hat{w}}{\partial y} \end{array} \right\} = \frac{1}{2}\Theta \left\{ \begin{array}{c} \frac{\partial(\mathbf{N}_w{}^T \mathbf{u}_w)}{\partial x} \\ \frac{\partial(\mathbf{N}_w{}^T \mathbf{u}_w)}{\partial y} \end{array} \right\} = \frac{1}{2}\Theta \mathbf{B}_\theta \mathbf{u}_w, \tag{2.34}$$

in which

$$\mathbf{B}_\theta = \begin{bmatrix} \frac{\partial N_1}{\partial x} & \frac{\partial N_2}{\partial x} & \frac{\partial N_3}{\partial x} & \frac{\partial N_4}{\partial x} \\ \frac{\partial N_1}{\partial y} & \frac{\partial N_2}{\partial y} & \frac{\partial N_3}{\partial y} & \frac{\partial N_4}{\partial y} \end{bmatrix}, \tag{2.35}$$

and

$$\Theta = \begin{bmatrix} \frac{\partial \hat{w}}{\partial x} & 0 \\ 0 & \frac{\partial \hat{w}}{\partial y} \\ \frac{\partial \hat{w}}{\partial y} & \frac{\partial \hat{w}}{\partial x} \end{bmatrix}. \tag{2.36}$$

At last, the transverse shear strain, ε_s, can be written as

$$\varepsilon_s = \left\{\begin{array}{c} \frac{\partial \hat{w}}{\partial x} \\ \frac{\partial \hat{w}}{\partial y} \end{array}\right\} - \left\{\begin{array}{c} \phi_x \\ \phi_y \end{array}\right\} = \mathbf{B}_\theta \mathbf{u}_w - \mathbf{B}_c \mathbf{u}_\phi, \tag{2.37}$$

in which

$$\mathbf{B}_c = \begin{bmatrix} N_1 & 0 & N_2 & 0 & N_3 & 0 & N_4 & 0 \\ 0 & N_1 & 0 & N_2 & 0 & N_3 & 0 & N_4 \end{bmatrix}. \tag{2.38}$$

The virtual strains must also be discretised. For the linear terms, the result is trivial:

$$\delta \varepsilon_m = \delta\left(\mathbf{B}_m \mathbf{u}_m\right) = \mathbf{B}_m \delta \mathbf{u}_m, \tag{2.39}$$

$$\delta \kappa = \delta\left(-\mathbf{B}_m \kappa\right) = -\mathbf{B}_m \delta \kappa, \tag{2.40}$$

$$\delta \varepsilon_s = \delta\left(\mathbf{B}_\theta \mathbf{u}_w - \mathbf{B}_c \mathbf{u}_\phi\right) = \mathbf{B}_\theta \delta \mathbf{u}_w - \mathbf{B}_c \delta \mathbf{u}_\phi. \tag{2.41}$$

The nonlinear component yields

$$\delta \varepsilon_\theta = \left\{\begin{array}{c} \delta\left(\frac{1}{2}\left(\frac{\partial \hat{w}}{\partial x}\right)^2\right) \\ \delta\left(\frac{1}{2}\left(\frac{\partial \hat{w}}{\partial y}\right)^2\right) \\ \delta\left(\frac{\partial \hat{w}}{\partial x}\frac{\partial w}{\partial y}\right) \end{array}\right\} = \left\{\begin{array}{c} \frac{\partial \hat{w}}{\partial x}\delta\left(\frac{\partial \hat{w}}{\partial x}\right) \\ \frac{\partial \hat{w}}{\partial y}\delta\left(\frac{\partial \hat{w}}{\partial y}\right) \\ \frac{\partial \hat{w}}{\partial y}\delta\left(\frac{\partial \hat{w}}{\partial x}\right) + \frac{\partial \hat{w}}{\partial x}\delta\left(\frac{\partial \hat{w}}{\partial y}\right) \end{array}\right\} = \begin{bmatrix} \frac{\partial \hat{w}}{\partial x} & 0 \\ 0 & \frac{\partial \hat{w}}{\partial y} \\ \frac{\partial \hat{w}}{\partial y} & \frac{\partial \hat{w}}{\partial x} \end{bmatrix} \delta\left\{\begin{array}{c} \frac{\partial \hat{w}}{\partial x} \\ \frac{\partial \hat{w}}{\partial y} \end{array}\right\} = \Theta \mathbf{B}_\theta \delta \mathbf{u}_\rho. \tag{2.42}$$

Now that all the strain components and their corresponding virtual quantities have been written in discrete form, it is possible to advance in the finite element formulation.

The PVW must be discretised and ultimately written in terms of nodal degrees of freedom and their time derivatives. Recalling Eq. (2.11), it is possible to see that for a general laminate ($\mathbf{B} \neq \mathbf{0}$) the internal work has five major contributions. Each one is handled separately here. First, the bending energy within an element in the mesh is

$$\int_{\Omega_e} \delta \kappa^T \mathbf{D} \kappa \, dA, \tag{2.43}$$

with Ω_e being the elemental domain. Mind that every energy term in the PVW is calculated for each finite element in the mesh. The elemental contributions are ultimately assembled in the form of global matrices and vectors. The procedure employed for integrating the present quantities within the elements is addressed in subsection 2.2.3.

Substituting Eqs. (2.33) and (2.40) into Eq. (2.43) yields

$$\int_{\Omega_e} \delta \kappa^T \mathbf{D} \kappa \, dA = \int_{\Omega_e} \left(-\mathbf{B}_m \delta \mathbf{u}_\phi\right)^T \mathbf{D} \left(-\mathbf{B}_m \mathbf{u}_\phi\right) dA = \delta \mathbf{u}_\phi^T \left(\int_{\Omega_e} \mathbf{B}_m^T \mathbf{D} \mathbf{B}_m \, dA\right) \mathbf{u}_\phi. \tag{2.44}$$

It is convenient to rewrite Eq. (2.44) as

$$\left\{\delta \mathbf{u}_m^T \quad \delta \mathbf{u}_w^T \quad \delta \mathbf{u}_\phi^T\right\} \begin{bmatrix} 0 & 0 & 0 \\ 0 & 0 & 0 \\ 0 & 0 & \int_{\Omega_e} \mathbf{B}_m^T \mathbf{D} \mathbf{B}_m \, dA \end{bmatrix} \left\{\begin{array}{c} \mathbf{u}_m \\ \mathbf{u}_w \\ \mathbf{u}_\phi \end{array}\right\} = \delta \mathbf{u}^T \mathbf{k}_\mathbf{D} \mathbf{u}. \tag{2.45}$$

The energy due to transverse shear is

$$\int_{\Omega_e} \delta\varepsilon_s{}^T \mathbf{C}\varepsilon_s \, \mathrm{d}A = \int_{\Omega_e} (\mathbf{B}_\theta \delta\mathbf{u}_w - \mathbf{B}_c \delta\mathbf{u}_\phi)^T \, \mathbf{C} \, (\mathbf{B}_\theta \mathbf{u}_w - \mathbf{B}_c \mathbf{u}_\phi) \, \mathrm{d}A = \delta\mathbf{u}^T \mathbf{k_C} \mathbf{u}, \qquad (2.46)$$

in which

$$\mathbf{k_C} = \int_{\Omega_e} \left(\begin{bmatrix} 0 & 0 & 0 \\ 0 & \mathbf{B}_\theta{}^T \mathbf{C} \mathbf{B}_\theta & -\mathbf{B}_\theta{}^T \mathbf{C} \mathbf{B}_c \\ 0 & -\mathbf{B}_c{}^T \mathbf{C} \mathbf{B}_\theta & \mathbf{B}_c{}^T \mathbf{C} \mathbf{B}_c \end{bmatrix} \right) \mathrm{d}A \qquad (2.47)$$

The third contribution comes from the midsurface strain:

$$\int_{\Omega_e} \delta\varepsilon_0{}^T \mathbf{A}\varepsilon_0 \, \mathrm{d}A = \int_{\Omega_e} (\mathbf{B}_m \delta\mathbf{u}_m + \Theta\mathbf{B}_\theta \delta\mathbf{u}_w)^T \, \mathbf{A} \left(\mathbf{B}_m \mathbf{u}_m + \frac{1}{2}\Theta\mathbf{B}_\theta \mathbf{u}_w \right) \mathrm{d}A, \qquad (2.48)$$

which leads to four terms:

$$\int_{\Omega_e} \left[\delta\mathbf{u}_m{}^T \left(\mathbf{B}_m{}^T \mathbf{A} \mathbf{B}_m \right) \mathbf{u}_m + \delta\mathbf{u}_m{}^T \left(\frac{1}{2}\mathbf{B}_m{}^T \mathbf{A}\Theta\mathbf{B}_\theta \right) \mathbf{u}_w + \right.$$
$$\left. \delta\mathbf{u}_w{}^T \left(\frac{1}{2}\mathbf{B}_\theta{}^T \Theta^T \mathbf{A}\Theta\mathbf{B}_\theta \right) \mathbf{u}_w + \delta\mathbf{u}_w{}^T \left(\mathbf{B}_m{}^T \mathbf{A}\Theta\mathbf{B}_\theta \right)^T \mathbf{u}_m \right] \mathrm{d}A, \qquad (2.49)$$

the fourth of which can be split into two equal parts so that Eq. (2.49) becomes

$$\int_{\Omega_e} \left[\delta\mathbf{u}_m{}^T \left(\mathbf{B}_m{}^T \mathbf{A} \mathbf{B}_m \right) \mathbf{u}_m + \delta\mathbf{u}_m{}^T \left(\frac{1}{2}\mathbf{B}_m{}^T \mathbf{A}\Theta\mathbf{B}_\theta \right) \mathbf{u}_w + \delta\mathbf{u}_w{}^T \left(\frac{1}{2}\mathbf{B}_\theta{}^T \Theta^T \mathbf{A}\Theta\mathbf{B}_\theta \right) \mathbf{u}_w + \right.$$
$$\left. \delta\mathbf{u}_w{}^T \left(\frac{1}{2}\mathbf{B}_m{}^T \mathbf{A}\Theta\mathbf{B}_\theta \right)^T \mathbf{u}_m + \delta\mathbf{u}_w{}^T \left(\frac{1}{2}\mathbf{B}_m{}^T \mathbf{A}\Theta\mathbf{B}_\theta \right)^T \mathbf{u}_m \right] \mathrm{d}A. \qquad (2.50)$$

The fifth term in Eq. (2.50) must undergo some algebraic manipulation in order for the final $\mathbf{k_A}$ stiffness matrix to be symmetric. It is possible to show that

$$\delta\mathbf{u}_w{}^T \left(\frac{1}{2}\mathbf{B}_m{}^T \mathbf{A}\Theta\mathbf{B}_\theta \right)^T \mathbf{u}_m = \delta\mathbf{u}_w{}^T \left(\frac{1}{2}\mathbf{B}_\theta{}^T \mathbf{N}_m \mathbf{B}_\theta \right) \mathbf{u}_w, \qquad (2.51)$$

in which

$$\mathbf{N}_m = \begin{bmatrix} N_m^x & N_m^{xy} \\ N_m^{xy} & N_m^y \end{bmatrix}, \qquad (2.52)$$

and

$$\{ N_m^x \quad N_m^y \quad N_m^{xy} \} = (\mathbf{A}\mathbf{B}_m \mathbf{u}_m)^T. \qquad (2.53)$$

Hence, the virtual midsurface strain energy becomes $\delta\mathbf{u}^T \mathbf{k_A} \mathbf{u}$, in which

$$\mathbf{k_A} = \int_{\Omega_e} \left(\begin{bmatrix} \mathbf{B}_m{}^T \mathbf{A} \mathbf{B}_m & \frac{1}{2}\mathbf{B}_m{}^T \mathbf{A}\Theta\mathbf{B}_\theta & 0 \\ \left(\frac{1}{2}\mathbf{B}_m{}^T \mathbf{A}\Theta\mathbf{B}_\theta \right)^T & \frac{1}{2}\mathbf{B}_\theta{}^T \left(\Theta^T \mathbf{A}\Theta + \mathbf{N}_m \right) \mathbf{B}_\theta & 0 \\ 0 & 0 & 0 \end{bmatrix} \right) \mathrm{d}A. \qquad (2.54)$$

Finally, the fourth and fifth contributions to the virtual strain energy come from the coupling between bending and axial deformations:

$$\int_{\Omega_e} \delta\varepsilon_0{}^T \mathbf{B}\kappa + \delta\kappa^T \mathbf{B}\varepsilon_0 \, \mathrm{d}A, \qquad (2.55)$$

which after the FE discretisation becomes $\delta \mathbf{u}^T \mathbf{k_B} \mathbf{u}^T$, with

$$\mathbf{k_B} = -\int_{\Omega_e} \left(\begin{bmatrix} \mathbf{0} & \mathbf{0} & \mathbf{B}_m{}^T \mathbf{B} \mathbf{B}_m \\ \mathbf{0} & \frac{1}{2}\mathbf{B}_\theta{}^T \mathbf{N}_\phi \mathbf{B}_\theta & \frac{1}{2}\mathbf{B}_\theta{}^T \Theta^T \mathbf{B} \mathbf{B}_m \\ \left(\mathbf{B}_m{}^T \mathbf{B} \mathbf{B}_m\right)^T & \left(\frac{1}{2}\mathbf{B}_\theta{}^T \Theta^T \mathbf{B} \mathbf{B}_m\right)^T & \mathbf{0} \end{bmatrix} \right) \mathrm{d}A, \qquad (2.56)$$

in which

$$\mathbf{N}_\phi = \begin{bmatrix} N_\phi^x & N_\phi^{xy} \\ N_\phi^{xy} & N_\phi^y \end{bmatrix}, \qquad (2.57)$$

and

$$\left\{ N_\phi^x \quad N_\phi^y \quad N_\phi^{xy} \right\} = (\mathbf{B} \mathbf{B}_m \mathbf{u}_\phi)^T. \qquad (2.58)$$

Finally, the virtual strain energy within an element e is

$$\delta W_{\mathrm{int}}^e = \delta \mathbf{u}^T \left(\mathbf{k_A} + \mathbf{k_B} + \mathbf{k_C} + \mathbf{k_D} \right) \mathbf{u}. \qquad (2.59)$$

It is convenient to rearrange the stiffness matrices in Eq. (2.59) as zeroth-, first- and second-order terms: $\mathbf{k}_0^p$, $\mathbf{k}_1^p$ and $\mathbf{k}_2^p$, respectively:

$$\delta W_{\mathrm{int}}^e = \delta \mathbf{u}^T \left(\mathbf{k}_0^p + \mathbf{k}_1^p + \mathbf{k}_2^p \right) \mathbf{u}, \qquad (2.60)$$

in which

$$\mathbf{k}_0^p = \int_{\Omega_e} \left(\begin{bmatrix} \mathbf{B}_m{}^T \mathbf{A} \mathbf{B}_m & \mathbf{0} & -\mathbf{B}_m{}^T \mathbf{B} \mathbf{B}_m \\ \mathbf{0} & \mathbf{B}_\theta{}^T \mathbf{C} \mathbf{B}_\theta & -\mathbf{B}_\theta{}^T \mathbf{C} \mathbf{B}_c \\ \left(-\mathbf{B}_m{}^T \mathbf{B} \mathbf{B}_m\right)^T & \left(-\mathbf{B}_\theta{}^T \mathbf{C} \mathbf{B}_c\right)^T & \mathbf{B}_c{}^T \mathbf{C} \mathbf{B}_c + \mathbf{B}_m{}^T \mathbf{D} \mathbf{B}_m \end{bmatrix} \right) \mathrm{d}A, \qquad (2.61)$$

$$\mathbf{k}_1^p = \frac{1}{2} \int_{\Omega_e} \left(\begin{bmatrix} \mathbf{0} & \mathbf{B}_m{}^T \mathbf{A} \Theta \mathbf{B}_\theta & \mathbf{0} \\ \left(\mathbf{B}_m{}^T \mathbf{A} \Theta \mathbf{B}_\theta\right)^T & \mathbf{B}_\theta{}^T \left(\mathbf{N}_m - \mathbf{N}_\phi\right) \mathbf{B}_\theta & -\mathbf{B}_\theta{}^T \Theta^T \mathbf{B} \mathbf{B}_m \\ \mathbf{0} & \left(-\mathbf{B}_\theta{}^T \Theta^T \mathbf{B} \mathbf{B}_m\right)^T & \mathbf{0} \end{bmatrix} \right) \mathrm{d}A, \qquad (2.62)$$

$$\mathbf{k}_2^p = \int_{\Omega_e} \left(\begin{bmatrix} \mathbf{0} & \mathbf{0} & \mathbf{0} \\ \mathbf{0} & \frac{1}{2}\mathbf{B}_\theta{}^T \Theta^T \mathbf{A} \Theta \mathbf{B}_\theta & \mathbf{0} \\ \mathbf{0} & \mathbf{0} & \mathbf{0} \end{bmatrix} \right) \mathrm{d}A, \qquad (2.63)$$

superscript p standing for "plate".

The zeroth-order stiffness is constant, whereas the first- and second-order matrices depend upon $\mathbf{u}$ linearly and quadratically, respectively. For this reason, the geometrical non-linearity of the discretised plate model is expressed through $\mathbf{k}_1^p$ and $\mathbf{k}_2^p$. The classical linear Mindlin plate theory is recovered by setting $\mathbf{k}_1^p = \mathbf{k}_2^p = \mathbf{0}$.

The discretisation of the external work is a simpler process. It consists of inserting Eqs. (2.27) - (2.30) into Eq. (2.11). The work due to the pressure load becomes

$$\int_{\Omega_e} \delta \hat{w} \Delta p \, \mathrm{d}A = \int_A \delta \left(\mathbf{u}_w{}^T \mathbf{N}_w \right) \Delta p(x, y, t) \, \mathrm{d}A = \delta \mathbf{u}_w{}^T \int_{\Omega_e} \mathbf{N}_w \Delta p(x, y, t) \, \mathrm{d}A = \delta \mathbf{u}^T \mathbf{f}, \qquad (2.64)$$

with

$$f = \left\{ \begin{array}{c} 0 \\ \int_{\Omega_e} N_w \Delta p \ dA \\ 0 \end{array} \right\}. \tag{2.65}$$

Note that, for now, the pressure field is assumed as arbitrary and independent on **u**. In section 2.4, Δp is treated as an aerodynamic pressure which is a function of $\hat{w}$ and its derivatives.

The inertial work within an element becomes simply

$$-\delta \mathbf{u}^T \mathbf{m}^p \frac{\partial^2 \mathbf{u}}{\partial t^2} \tag{2.66}$$

with $\mathbf{m}^p$ being the elemental mass matrix, given by

$$\mathbf{m}^p = \begin{bmatrix} \mathbf{m}_m^p & 0 & 0 \\ 0 & \mathbf{m}_w^p & 0 \\ 0 & 0 & \mathbf{m}_\phi^p \end{bmatrix} = \begin{bmatrix} h\left(\mathbf{m}_x + \mathbf{m}_y\right) & 0 & 0 \\ 0 & h\mathbf{m}_z & 0 \\ 0 & 0 & \frac{h^3}{12}\left(\mathbf{m}_x + \mathbf{m}_y\right) \end{bmatrix}, \tag{2.67}$$

in which

$$\mathbf{m}_x = \int_{\Omega_e} \rho \mathbf{N}_u \mathbf{N}_u^T \ dA, \tag{2.68}$$

$$\mathbf{m}_y = \int_{\Omega_e} \rho \mathbf{N}_v \mathbf{N}_v^T \ dA, \tag{2.69}$$

$$\mathbf{m}_z = \int_{\Omega_e} \rho \mathbf{N}_w \mathbf{N}_w^T \ dA. \tag{2.70}$$

$$\tag{2.71}$$

After the finite element discretisation and assembly, the equality stated by the Principle of Virtual Work becomes

$$\delta \mathbf{U}^T \left(\mathbf{F} - \mathbf{M}^p \ddot{\mathbf{U}} \right) = \delta \mathbf{U}^T \left(\mathbf{K}_0^p + \mathbf{K}_1^p + \mathbf{K}_2^p \right) \mathbf{U}, \tag{2.72}$$

or

$$\delta \mathbf{U}^T \left[\mathbf{M}^p \ddot{\mathbf{U}} + \left(\mathbf{K}_0^p + \mathbf{K}_1^p + \mathbf{K}_2^p \right) \mathbf{U} - \mathbf{F} \right] = 0, \tag{2.73}$$

in which the dot symbol represents time derivatives: $\dot{\mathbf{U}} = \frac{d\mathbf{U}}{dt}$ and $\ddot{\mathbf{U}} = \frac{d^2\mathbf{U}}{dt^2}$. It is important to note that the matrices and vectors in Eq. (2.73) are now written in capital letters, meaning that they represent global quantities (post-assembly). For example, matrix $\mathbf{K}_0^p$ is obtained by assembling all the elemental contributions in terms of $\mathbf{k}_0^p$. Moreover, **U** is the vector that contains all the degrees of freedom in the FE mesh.

The PVW states that the internal and external virtual works must be equal for any compatible virtual displacement field, $\delta \mathbf{U}$. Thus, Eq (2.73) is reduced to

$$\mathbf{M}^p \ddot{\mathbf{U}} + \left(\mathbf{K}_0^p + \mathbf{K}_1^p + \mathbf{K}_2^p \right) \mathbf{U} = \mathbf{F}, \tag{2.74}$$

which is the system of ordinary differencial equations (ODEs) that dictate the motion of the discrete plate system. Moreover, it is a nonlinear ODE system, as the values of matrices $\mathbf{K}_1^p$ and $\mathbf{K}_2^p$ at any given time depend on the solution, $\mathbf{U}$, at that same time. In order to solve Eq. (2.74), numerical time-marching is required, which is the subject of section 2.5.

2.2.2 Constitutive modelling

In order to derive the finite element formulation for the Mindlin-von Kármán plate in section 2.2, it has been assumed that the constitutive plate stiffnesses ($\mathbf{A}, \mathbf{B}, \mathbf{C}$ and $\mathbf{D}$) can be calculated. This section deals with the computation of such matrices for a general laminated Mindlin plate.

Let there be a panel with n_l layers, so that the first layer's lower surface is at $z = -h/2$ and the n_l-th layer's upper surface is at $z = h/2$. Assume that the k-th layer has fibers uniformly oriented along direction 1, which is rotated θ_k degrees counterclockwise from direction y. Thus, direction 2 is the in-plane normal to 1, and direction 3 coincides with z. Figure 5 shows the local and global systems for a generic layer. The in-plane constitutive matrix with respect to the local coordinate system is (NETTLES, 1994)

$$\mathbf{Q}_p = \begin{bmatrix} Q_{11} & Q_{12} & 0 \\ Q_{12} & Q_{22} & 0 \\ 0 & 0 & Q_{66} \end{bmatrix}, \tag{2.75}$$

whose entries are

$$Q_{11} = \frac{E_1}{1 - \nu_{12}\nu_{21}}, \tag{2.76}$$

$$Q_{22} = \frac{E_2}{1 - \nu_{12}\nu_{21}}, \tag{2.77}$$

$$Q_{12} = \nu_{12}Q_{22}, \tag{2.78}$$

$$Q_{66} = G_{12}, \tag{2.79}$$

in which ν_{12} and ν_{21} are the in-plane Poisson's ratios, G_{12} is the in-plane shear modulus and E_1 e E_2 are the in-plane Young's moduli. The Poisson's ratios are related by

$$\frac{\nu_{21}}{\nu_{12}} = \frac{E_2}{E_1}. \tag{2.80}$$

The transverse shear matrix is

$$\mathbf{Q}_s = \begin{bmatrix} G_{13} & 0 \\ 0 & G_{23} \end{bmatrix}, \tag{2.81}$$

in which G_{13} and G_{23} are the transverse shear moduli.

Figure 5 – Local and global coordinate systems for a generic layer.
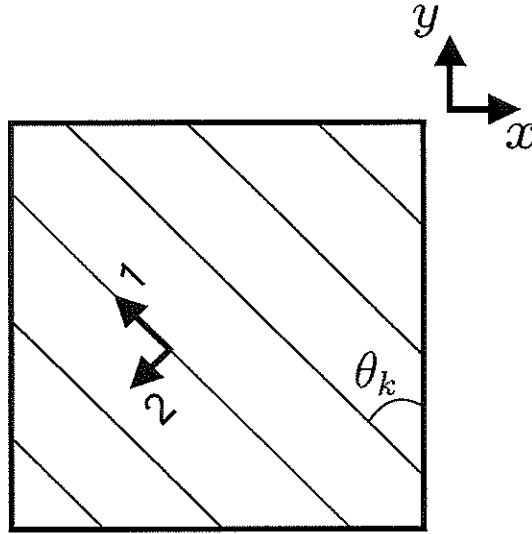
Source: Elaborated by the author.

The constitutive matrices must be transformed from the local to the global system for calculation purposes. The in-plane matrix with respect to the (x, y, z) system is

$$\bar{\mathbf{Q}}_p^{(k)} = (\mathbf{P}\mathbf{T}_k)^{-1} \mathbf{Q}_p (\mathbf{T}_k\mathbf{P}), \tag{2.82}$$

in which

$$\mathbf{P} = \begin{bmatrix} 1 & 0 & 0 \\ 0 & 1 & 0 \\ 0 & 0 & \frac{1}{2} \end{bmatrix}, \tag{2.83}$$

and

$$\mathbf{T}_k = \begin{bmatrix} s_k{}^2 & c_k{}^2 & -2c_k s_k \\ c_k{}^2 & s_k{}^2 & 2c_k s_k \\ c_k s_k & -c_k s_k & s_k{}^2 - c_k{}^2 \end{bmatrix}, \tag{2.84}$$

with $s_k = \sin\theta_k$ e $c_k = \cos\theta_k$. The transverse shear matrix becomes (REDDY, 2004)

$$\bar{\mathbf{Q}}_s^{(k)} = \begin{bmatrix} \bar{Q}_{55} & \bar{Q}_{45} \\ \bar{Q}_{45} & \bar{Q}_{44} \end{bmatrix}, \tag{2.85}$$

in which

$$\bar{Q}_{44} = G_{13}s_k{}^2 + G_{23}c_k{}^2, \tag{2.86}$$

$$\bar{Q}_{55} = G_{13}c_k{}^2 + G_{23}s_k{}^2, \tag{2.87}$$

$$\bar{Q}_{45} = (G_{13} - G_{23})s_k c_k. \tag{2.88}$$

Since matrices $\bar{\mathbf{Q}}_p$ and $\bar{\mathbf{Q}}_s$ are layer-wise constant, the integrals in Eqs. (2.12) and (2.13) turn into summations:

$$\mathbf{A} = \int_{-h/2}^{h/2} \bar{\mathbf{Q}}_p \, \mathrm{d}z = \sum_{k=1}^{n_l} (z_{k+1} - z_k) \, \bar{\mathbf{Q}}_p^{(k)}, \tag{2.89}$$

$$\mathbf{B} = \int_{-h/2}^{h/2} \bar{\mathbf{Q}}_p \, \mathrm{d}z = \frac{1}{2} \sum_{k=1}^{n_l} \left(z_{k+1}^2 - z_k^2\right) \bar{\mathbf{Q}}_p^{(k)}, \tag{2.90}$$

$$\mathbf{D} = \int_{-h/2}^{h/2} \bar{\mathbf{Q}}_p \, \mathrm{d}z = \frac{1}{3} \sum_{k=1}^{n_l} \left(z_{k+1}^3 - z_k^3\right) \bar{\mathbf{Q}}_p^{(k)}, \tag{2.91}$$

$$\tilde{\mathbf{C}} = \int_{-h/2}^{h/2} \bar{\mathbf{Q}}_s \, \mathrm{d}z = \sum_{k=1}^{n_l} (z_{k+1} - z_k) \, \bar{\mathbf{Q}}_s^{(k)}. \tag{2.92}$$

Matrix $\tilde{\mathbf{C}}$ must still be corrected for nonuniform shear. The classical Mindlin plate model accounts for shear deformability, yet introduces an unrealist kinematic consideration by assuming shear strains to be constant along the thickness. In reality, the transverse shear strains normally present a near-parabolic distribution, being zero at $z = \pm\frac{h}{2}$ and taking maximum value in between. In order to compensate for such discrepancy between assumed and real distributions, shear correction is required.

There exist several approaches for overcoming this issue (CHOW, 1971; LIU; SOH, 2007; SRINIVAS, 1973; WHITNEY, 1972; WHITNEY, 1973). The most popular method is perhaps the one proposed by Whitney (1972). It is based on an energy equivalence principle, imposing that the assumed (uniform) shear distribution yield the same amount of strain energy as the physical one would. The present section explains the mathematical aspects and steps of such approach. Details on the theoretical basis behind this method can be found in Chow (1971) and Whitney (1972).

The corrected shear matrix is of the form

$$\mathbf{C} = \begin{bmatrix} k_1{}^2 \tilde{C}_{11} & k_1 k_2 \tilde{C}_{12} \\ k_1 k_2 \tilde{C}_{12} & k_2{}^2 \tilde{C}_{22,} \end{bmatrix} \tag{2.93}$$

in which the $\tilde{C}_{ij}$ coefficients are the elements of matrix $\tilde{\mathbf{C}}$ (Eq. (2.92)), and k_1 and k_2 are the so-called shear correction factors. The procedure described here is valid for an asymmetric orthotropic plate. The calculations for a general anisotropic plate are similar, yet somewhat more cumbersome, and can be found in detail in Whitney (1972). For an orthotropic plate, the first factor is calculated as

$$k_1{}^2 = \left\{ \tilde{C}_{11} \int_{-h/2}^{h/2} S_1(z) \left[g(z)\right]^2 \mathrm{d}z \right\}^{-1}, \tag{2.94}$$

in which S_1 is the inverse of the first element in matrix $\bar{\mathbf{Q}}_s$, and $g(z)$ is a layer-wise parabolic "shape function" of the form

$$g_k(z) = \gamma_k + \beta_k z + \alpha_k z^2. \tag{2.95}$$

Coefficients β_k and α_k are calculated as

$$\alpha_k = -\frac{A_{11}\bar{Q}_{11}^{(k)}}{2\Delta_{11}}, \tag{2.96}$$

$$\beta_k = -\frac{2B_{11}}{A_{11}}\alpha_k, \tag{2.97}$$

in which $\Delta_{11} = A_{11}D_{11} - B_{11}^2$, and A_{11}, B_{11} and D_{11} are the first entries in matrices $\mathbf{A}$, $\mathbf{B}$ and $\mathbf{D}$, respectively. The coefficients γ_k are obtained by enforcing continuity of $g(z)$, that is,

$$g_k(z_{k-1}) = g_{k-1}(z_{k-1}), \tag{2.98}$$

which yields

$$\gamma_k = \gamma_{k-1} + (\beta_{k-1} - \beta_k)z_{k-1} + (\alpha_{k-1} - \alpha_k)z_{k-1}^2. \tag{2.99}$$

Thus, γ_k is defined in a recursive manner for $k > 1$. Since the shear strains must vanish at the plate surfaces, it is known that $g(-\frac{h}{2}) = 0$, that is,

$$\gamma_1 + \beta_1\left(-\frac{h}{2}\right) + \alpha_1\left(-\frac{h}{2}\right)^2 = 0 \;\Rightarrow\; \gamma_1 = \frac{h}{2}\left(\beta_1 - \frac{h}{2}\alpha_1\right). \tag{2.100}$$

Now, the integral in Eq. (2.94) can be calculated:

$$\int_{-h/2}^{h/2} S_1(z)\left[g(z)\right]^2 dz = \sum_{k=1}^{n_l}\left\{S_1^{(k)}\int_{z_{k-1}}^{z_k}\left[g_k(z)\right]^2 dz\right\} = \sum_{k=1}^{n_l}\left\{S_1^{(k)}\left[\gamma_k^2\left(z_k - z_{k-1}\right) + \right.\right.$$
$$\left.\left.\gamma_k\beta_k\left(z_k^2 - z_{k-1}^2\right) + \frac{2\gamma_k\alpha_k + \beta_k^2}{3}\left(z_k^3 - z_{k-1}^3\right) + \frac{\beta_k\alpha_k}{2}\left(z_k^4 - z_{k-1}^4\right) + \frac{\alpha_k^2}{5}\left(z_k^5 - z_{k-1}^5\right)\right]\right\}. \tag{2.101}$$

The steps for calculating k_2 are analogous, requiring only that the quantities of interest be taken at position $()_{22}$ instead of $()_{11}$ in their respective matrices. Table 1 shows two examples of shear correction factors for cross-ply laminates whose material properties are $\nu_{12} = 0.25$ and $E_2 = 0.04E_1 = 2G_{12} = 2G_{13} = 5G_{23}$.

Table 1 – Shear correction factors for cross-ply laminates.

Lamination	k_1^2	k_2^2
[0° 90°]	0.82123	0.82123
[0° 90°]$_s$	0.59518	0.72053

Source: Elaborated by the author.

2.2.3 Numerical integration

The stiffness and mass matrices can be calculated via numerical quadrature. An integral is computed/approximated within a finite element by evaluating the integrands at certain points and combining such values in a weighted avarage. The approximmation becomes more accurate as the number of points grows. An $(N \times N)$-point gaussian quadrature over a quadrilateral element can be described as (SZABO; BABUÂŠKA, 1991)

$$\int_{-1}^{1} \int_{-1}^{1} \Phi(\xi, \eta) d\xi d\eta \simeq \sum_{i=1}^{N} \sum_{j=1}^{N} \omega_i \omega_j \Phi(\xi_i, \xi_j), \qquad (2.102)$$

in which Φ is a generic function, ξ_k are the so-called Gauss points and ω_k are their respective weights. Note that the quadrature is defined for a reference square element: $\Omega_{\text{ref}} = [-1, 1]^2$. Therefore, an integral over a generic element requires transformation of coordinates in order to be suitable for gaussian quadrature, as illustrated in Figure 6. When the physical elements are rectangles, which is the case herein, only stretching and translation are required for transforming (x, y) into (ξ, η):

$$x(\xi, \eta) = x(\xi) = \frac{\xi + 1}{2} \Delta x, \qquad (2.103)$$

$$y(\xi, \eta) = y(\eta) = \frac{\eta + 1}{2} \Delta y. \qquad (2.104)$$

Therefore, the jacobian determinant is simply

$$J = \det\left(\begin{bmatrix} \frac{\partial x}{\partial \xi} & \frac{\partial y}{\partial \xi} \\ \frac{\partial x}{\partial \eta} & \frac{\partial y}{\partial \eta} \end{bmatrix}\right) = \det\left(\begin{bmatrix} \frac{\Delta x}{2} & 0 \\ 0 & \frac{\Delta y}{2} \end{bmatrix}\right) = \frac{\Delta x \Delta y}{4}. \qquad (2.105)$$

Figure 6 – Illustration of the transformation from a physical to a reference element.
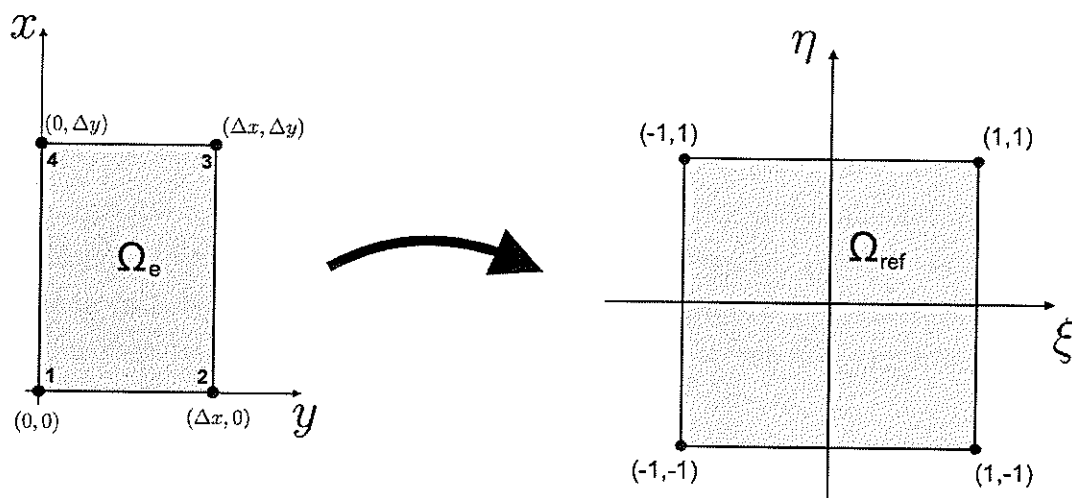
Source: Elaborated by the author.

In general cases, J is a function of (ξ, η). In the present case, however, the determinant is constant due to the straight, structured nature of the spatial mesh. Finally, an integral over an element can be evaluated as

$$
\int_{\Omega_e} \Phi(x,y) \, \mathrm{d}A = \int_0^{\Delta y} \int_0^{\Delta x} \Phi(x,y) \, \mathrm{d}x\mathrm{d}y = \int_{-1}^1 \int_{-1}^1 \Phi\left(x(\xi,\eta), y(\xi,\eta)\right) J\mathrm{d}\xi\mathrm{d}\eta
$$
$$
\simeq \sum_{i=1}^N \sum_{j=1}^N \omega_i \omega_j J \Phi\left(x(\xi_i, \xi_j), y(\xi_i, \xi_j)\right).
$$

(2.106)

Numerical integration can also be employed for overcoming a numerical issue that arises when the FEM is applied to the first-order shear plate theory. As the plate thickness-to-length ratio becomes smaller, the discretised strain energy due to transverse shear becomes progressively higher than the other strain energy terms, which is physically inconsistent. This phenomenon is called shear lock, and can be overcome through selective integration (FERREIRA, 2008). This simple technique consists of evaluating the transverse-shear-related stiffness matrices using fewer Gauss points than for the other matrices. This reduced integration is only required when the length-to-thickness ratio becomes large, say, $L/h > 40$. In the present work, four points (i.e., $N = 2$) are used for the main stiffness and mass terms, whereas $\mathbf{K_C}$ is evaluated with $N = 1$. For $N = 2$, the integration points are $\xi_1 = -\xi_2 = -\frac{1}{\sqrt{3}}$, and the weights are $\omega_1 = \omega_2 = 1$ (STROUD; SECREST, 1966). In other words,

$$
\int_{-1}^1 \int_{-1}^1 f(\xi, \eta)\mathrm{d}\xi\mathrm{d}\eta \simeq f\left(-\frac{1}{\sqrt{3}}, -\frac{1}{\sqrt{3}}\right) + f\left(-\frac{1}{\sqrt{3}}, \frac{1}{\sqrt{3}}\right) + f\left(\frac{1}{\sqrt{3}}, -\frac{1}{\sqrt{3}}\right) + f\left(\frac{1}{\sqrt{3}}, \frac{1}{\sqrt{3}}\right).
$$

(2.107)

The one-point integration is even simpler, with $\xi_1 = 0$ and $\omega_1 = 2$:

$$
\int_{-1}^1 \int_{-1}^1 f(\xi, \eta)\mathrm{d}\xi\mathrm{d}\eta \simeq 2 \times 2 \times f(0,0) = 4f(0,0).
$$

(2.108)

2.3   The nonlinear eccentric Timoshenko beam

The Timoshenko beam is the one-dimensional equivalent of the Mindlin plate, as it succeeds classical beam theory by accounting for shear deformability in bending. The Timoshenko theory is thus suitable for short beams – as well as for long ones, of course. In the present work, this theory is used for modelling stiffeners fixed underneath the main panel.

In the present case, the standard Timoshenko theory must me adapted in order to account for the eccentricity, i.e., the offset between the stiffener's neutral axis and the plate's midsurface. Figure 7 shows the stiffener's geometry. By introducing the eccentricity into the kinematic formulation, it is possible to write beam displacements in terms of plate

DOFs. The displacement field for the eccentric stiffener is (LEE; LEE, 1995)

$$u_b = \hat{u} + (e - z') \phi_x, \tag{2.109}$$

$$v_b = \hat{v} + (e - z') \phi_y, \tag{2.110}$$

$$w_b = \hat{w} + y' \phi_y, \tag{2.111}$$

in which e is the eccentricity and (z', y') are coordinates originating at the cross-sectional centroid (*cf.* Figure 7). Subscript b indicates *beam* quantities. For simplicity, the stiffener is herein assumed to have a rectangular cross-section. Hence, the cross-sectional area is

$$A_b = b \times c, \tag{2.112}$$

with b and c being the beam's width and height, respectively. The eccentricity is simply

$$e = \frac{h + c}{2}. \tag{2.113}$$

Figure 7 – Stiffener cross-section and dimensions.
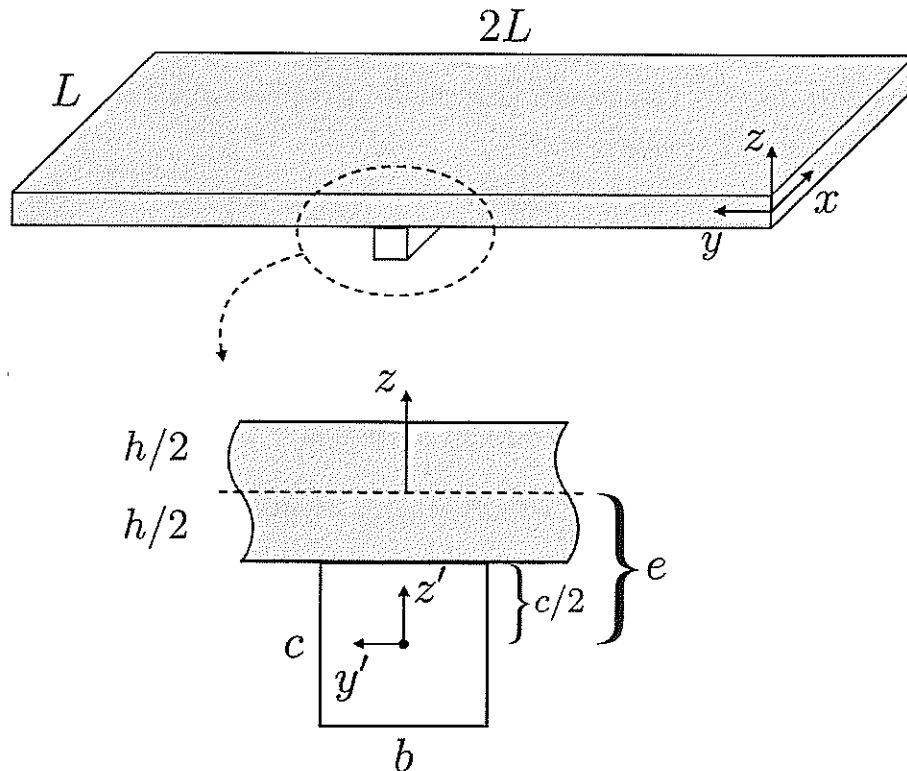
Source: Elaborated by the author.

It is important to note that the strain field described by Eqs. (2.109) - (2.111) assumes that the stiffeners are monolithically bound to the panel's lower surface, i.e., that beam and plate displacements are identical at the junction $\left(z = -\frac{h}{2}\right)$. This is easy to verify from the displacement fields, as $z' = z + e$.

It is also necessary to write the strain components in terms of plate DOFs. For an eccentric Timoshenko beam, considering geometrical non-linearity, the relevant components of the strain tensor can be given in vector form as (LEE, 1999; OH; LEE; LEE, 2001)

$$
\varepsilon_b = \begin{Bmatrix} \varepsilon_x \\ \gamma_{xy} \\ \gamma_{xz} \end{Bmatrix} = \begin{Bmatrix} \frac{\partial \hat{u}}{\partial x} \\ \frac{\partial \hat{v}}{\partial x} \\ \frac{\partial \hat{w}}{\partial x} - \phi_x \end{Bmatrix} + \begin{Bmatrix} (e - z') \frac{\partial \phi_x}{\partial x} \\ (e - z') \frac{\partial \phi_y}{\partial x} \\ y' \frac{\partial \phi_y}{\partial x} \end{Bmatrix} + \begin{Bmatrix} \frac{1}{2} \left(\frac{\partial \hat{w}}{\partial x} \right)^2 \\ 0 \\ 0 \end{Bmatrix}.
\tag{2.114}
$$

Considering the stiffener as isotropic, the virtual strain energy is

$$
\delta W_{\text{int}}^b = \int_{V_b} \left(\delta \varepsilon_x C_b \varepsilon_x + \delta \gamma_{xy} G_b \gamma_{xy} + \delta \gamma_{xz} \tau_{xz} \right) dV,
\tag{2.115}
$$

in which (REDDY; MAHAFFEY, 2013)

$$
C_b = \frac{(1 - \nu_b) E_b}{(1 + \nu_b)(1 - 2\nu_b)},
\tag{2.116}
$$

$$
G_b = \frac{E_b}{2(1 + \nu_b)},
\tag{2.117}
$$

and E_b and ν_b are the Young's modulus and Poisson's ratio of the stiffener. Substituting Eq. (2.114) into Eq. (2.115) yields several terms to the internal work. For instance, the energy due to γ_{xy} can be expanded into

$$
\int_{V_b} (\delta \gamma_{xy} G_b \gamma_{xy}) \, dV = G_b \int_0^L \int_{A_b} \delta \left[\frac{\partial \hat{v}}{\partial x} + (e - z') \frac{\partial \phi_y}{\partial x} \right] \left[\frac{\partial \hat{v}}{\partial x} + (e - z') \frac{\partial \phi_y}{\partial x} \right] dA dx,
\tag{2.118}
$$

in which L is the stiffener's length. Since the cross-section is rectangular (thus, bisymmetric),

$$
\int_{A_b} z' dA = \int_{A_b} y' dA = 0.
\tag{2.119}
$$

Besides, $\int_{A_b} (z')^2 dA = A_b \frac{c^2}{12}$, and $\int_{A_b} (y')^2 dA = A_b \frac{b^2}{12}$. Hence, Eq. (2.118) becomes

$$
\int_{V_b} (\delta \gamma_{xy} G_b \gamma_{xy}) \, dV = G_b A_b \int_0^L \delta \left(\frac{\partial \hat{v}}{\partial x} + e \frac{\partial \phi_y}{\partial x} \right) \left(\frac{\partial \hat{v}}{\partial x} + e \frac{\partial \phi_y}{\partial x} \right) + \frac{c^2}{12} \delta \left(\frac{\partial \phi_y}{\partial x} \right) \left(\frac{\partial \phi_y}{\partial x} \right) dx.
\tag{2.120}
$$

The contribution from xz-shear is

$$
\int_{V_b} (\delta \gamma_{xz} \tau_{xz}) \, dV = \int_0^L \int_{A_b} \delta \left[\frac{\partial \hat{w}}{\partial x} - \phi_x + y' \frac{\partial \phi_y}{\partial x} \right] G_b \left[k_b \left(\frac{\partial \hat{w}}{\partial x} - \phi_x \right) + y' \frac{\partial \phi_y}{\partial x} \right] dA dx,
\tag{2.121}
$$

in which $k_b = \frac{5}{6}$ is the shear correction factor used for the Timoshenko beam. After integration along the cross-section, Eq. (2.121) becomes

$$
\int_{V_b} (\delta \gamma_{xz} \tau_{xz}) \, dV = G_b A_b \int_0^L k_b \delta \left(\frac{\partial \hat{w}}{\partial x} - \phi_x \right) \left(\frac{\partial \hat{w}}{\partial x} - \phi_x \right) + \frac{b^2}{12} \delta \left(\frac{\partial \phi_y}{\partial x} \right) \left(\frac{\partial \phi_y}{\partial x} \right) dx.
\tag{2.122}
$$

The axial term becomes

$$\int_{V_b} \left(\delta\varepsilon_x C_b \varepsilon_x\right) dV = C_b A_b \int_0^L \left[\delta\left(\frac{\partial \hat{u}}{\partial x} + \frac{1}{2}\left(\frac{\partial \hat{w}}{\partial x}\right)^2 + e\frac{\partial \phi_x}{\partial x}\right)\left(\frac{\partial \hat{u}}{\partial x} + \frac{1}{2}\left(\frac{\partial \hat{w}}{\partial x}\right)^2 + e\frac{\partial \phi_x}{\partial x}\right) + \right.$$
$$\left. \frac{c^2}{12}\delta\left(\frac{\partial \phi_x}{\partial x}\right)\left(\frac{\partial \phi_x}{\partial x}\right)\right] dx.$$

$$(2.123)$$

The virtual external work for the stiffener is

$$\delta W_{\text{ext}}^b = -\int_{V_b} \rho_b \left(\delta u_b \frac{\partial^2 u_b}{\partial t^2} + \delta v_b \frac{\partial^2 v_b}{\partial t^2} + \delta w_b \frac{\partial^2 w_b}{\partial t^2}\right) dV. \qquad (2.124)$$

Upon substituting Eqs. (2.109) - (2.111) into Eq. (2.124), the inertial work becomes

$$\delta W_{\text{ext}}^b = -\rho_b A_b \int_0^L \left[\delta\left(\hat{u} + e\phi_x\right)\frac{\partial^2}{\partial t^2}\left(\hat{u} + e\phi_x\right) + \delta\left(\hat{v} + e\phi_y\right)\frac{\partial^2}{\partial t^2}\left(\hat{v} + e\phi_y\right) + \right.$$
$$\left. \delta\hat{w}\frac{\partial^2 \hat{w}}{\partial t^2} + \frac{c^2}{12}\delta\phi_x\frac{\partial^2 \phi_x}{\partial t^2} + \left(\frac{b^2 + c^2}{12}\right)\delta\phi_y\frac{\partial^2 \phi_y}{\partial t^2}\right] dx. \qquad (2.125)$$

The expressions obtained here for the external and internal works are as far the formulation can reach without spatial discretisation. Therefore, the FEM is employed in order to solve the integrals along the axial direction.

In order to maintain compatibility between the plate and beam models, a two-node lagrangian element is used for discretising the stiffener. This guarantees that the beam elements share nodes with plate elements. If the plate element had nine nodes instead of four, the beam element would have three nodes, and so on. Figure 8 exemplifies the FE mesh for a stiffened panel discretised with 24 elements. It is possible to observe that the beam elements are connected to the adjacent plate elements by the nodes.

The elemental DOF vector for the beam is written in a manner which is analogous to what has been done for the plate (cf. Eqs. (2.16) - (2.19)):

$$\mathbf{u}^b = \begin{Bmatrix} \mathbf{u}_m^b \\ \mathbf{u}_w^b \\ \mathbf{u}_\phi^b \end{Bmatrix}, \qquad (2.126)$$

in which

$$\mathbf{u}_m^b = \{u_1 \quad v_1 \quad u_2 \quad v_2\}^T, \qquad (2.127)$$

$$\mathbf{u}_w^b = \{w_1 \quad w_2\}^T, \qquad (2.128)$$

$$\mathbf{u}_\phi^b = \{\phi_{x1} \quad \phi_{y1} \quad \phi_{x2} \quad \phi_{y2}\}^T. \qquad (2.129)$$

The five kinematic quantities can then be interpolated within an element as

$$w = \mathbf{N}_w^{b\,T}\mathbf{u}_w^b, \quad u = \mathbf{N}_u^{b\,T}\mathbf{u}_m^b, \quad v = \mathbf{N}_v^{b\,T}\mathbf{u}_m^b, \quad \phi_x = \mathbf{N}_u^{b\,T}\mathbf{u}_\phi^b, \quad \text{and} \quad \phi_y = \mathbf{N}_v^{b\,T}\mathbf{u}_\phi^b, \qquad (2.130)$$

Figure 8 – Example of a FE mesh for a stiffened panel.
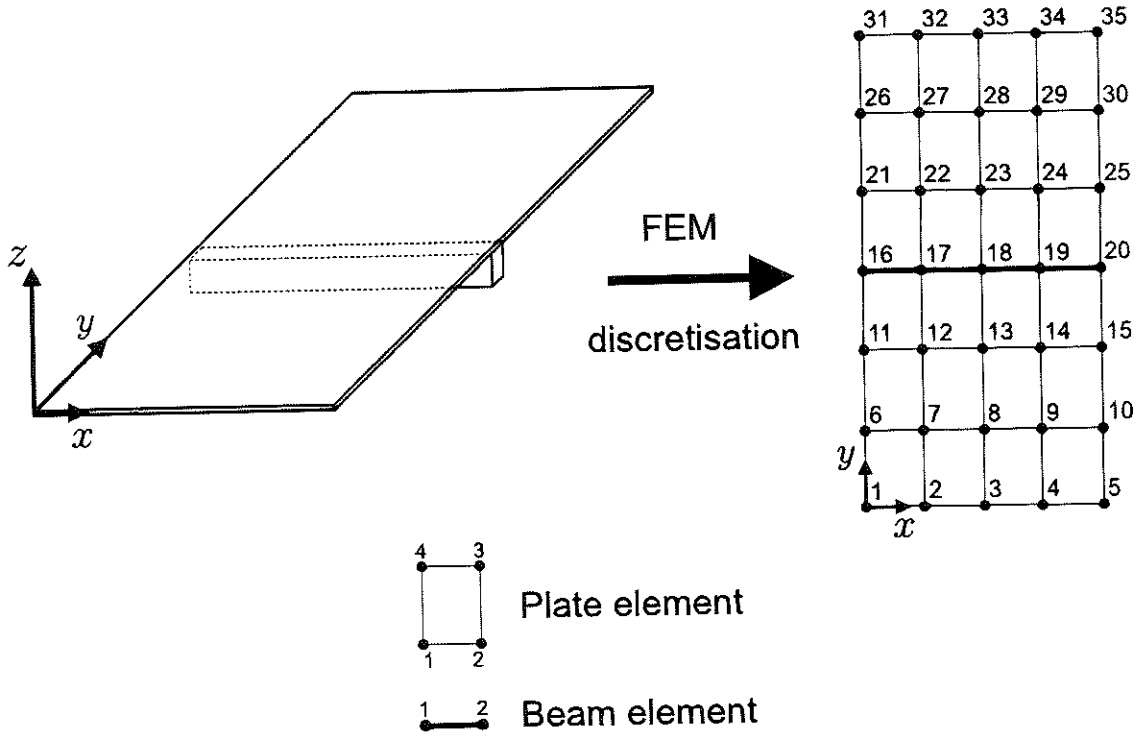
Source: Elaborated by the author.

in which the shape function vectors are $\mathbf{N}_u^b = \left\{ N_1^b \ \ 0 \ \ N_2^b \ \ 0 \right\}^T$, $\mathbf{N}_v^b = \left\{ 0 \ \ N_1^b \ \ 0 \ \ N_2^b \right\}^T$ and $\mathbf{N}_w^b = \left\{ N_1^b \ \ N_2^b \right\}^T$. The shape functions for a two-node beam element are linear:

$$N_1^b(x) = 1 - \frac{x}{\Delta x}, \tag{2.131}$$

$$N_2^b(x) = \frac{x}{\Delta x}. \tag{2.132}$$

The expressions given in Eqs. (2.131) and (2.132) are built considering that $x_1 = 0$. i.e., that the first node of the element has been translated to the origin for calculation purposes.

As seen in section 2.3, the virtual internal work has contributions from axial strain, xy-shear and xz-shear. Similarly to what has been done for the plate in subsection 2.2.1, the FEM approximation must be introduced into the strain energy expressions in order to produce the stiffness matrices.

First, recalling Eq. (2.120), it is possible to see that the expansion of the xy-shear strain energy yields several terms. They are composed of the multiplication of either $\frac{\partial \hat{v}}{\partial x}$ with $\frac{\partial \hat{v}}{\partial x}$, $\frac{\partial \hat{v}}{\partial x}$ with $\frac{\partial \phi_y}{\partial x}$, or $\frac{\partial \phi_y}{\partial x}$ with $\frac{\partial \phi_y}{\partial x}$. The latter, for instance, can be discretised as

$$\delta \left(\frac{\partial \phi_y}{\partial x} \right) \frac{\partial \phi_y}{\partial x} = \delta \left[\frac{\partial}{\partial x} \left(\mathbf{u}_\phi^{b\,T} \mathbf{N}_v^b \right) \right] \frac{\partial}{\partial x} \left(\mathbf{N}_v^{b\,T} \mathbf{u}_\phi^b \right) = \left(\delta \mathbf{u}_\phi^b \right)^T \left[\frac{\partial \mathbf{N}_v^b}{\partial x} \left(\frac{\partial \mathbf{N}_v^b}{\partial x} \right)^T \right] \mathbf{u}_\phi^b. \tag{2.133}$$

Hence,

$$\int_0^{\Delta x} \left[\delta\left(\frac{\partial \phi_y}{\partial x}\right)\frac{\partial \phi_y}{\partial x}\right] dx = \left(\delta\mathbf{u}_\phi^b\right)^T \left[\int_0^{\Delta x} \frac{\partial \mathbf{N}_v^b}{\partial x}\left(\frac{\partial \mathbf{N}_v^b}{\partial x}\right)^T dx\right]\mathbf{u}_\phi^b =$$

$$\left(\delta\mathbf{u}_\phi^b\right)^T \left(\int_0^{\Delta x} \begin{Bmatrix} 0 \\ -\frac{1}{\Delta x} \\ 0 \\ \frac{1}{\Delta x} \end{Bmatrix}\begin{Bmatrix} 0 \\ -\frac{1}{\Delta x} \\ 0 \\ \frac{1}{\Delta x} \end{Bmatrix}^T dx\right)\mathbf{u}_\phi^b = \left(\delta\mathbf{u}_\phi^b\right)^T \frac{\mathbf{S}_{vv}}{\Delta x}\mathbf{u}_\phi^b, \qquad (2.134)$$

in which

$$\mathbf{S}_{vv} = \begin{bmatrix} 0 & 0 & 0 & 0 \\ 0 & 1 & 0 & -1 \\ 0 & 0 & 0 & 0 \\ 0 & -1 & 0 & 1 \end{bmatrix}. \qquad (2.135)$$

It is analogous for the other products, so that the total xy-shear virtual strain contribution (Eq. (2.120)) integrated over an element can be written as

$$\int_{V_b^e}\left(\delta\gamma_{xy}G_b\gamma_{xy}\right)dV = \left(\delta\mathbf{u}_m^b\right)^T [\mathbf{K}_{vv}]\,\mathbf{u}_m^b + \left(\delta\mathbf{u}_m^b\right)^T [e\mathbf{K}_{vv}]\,\mathbf{u}_\phi^b + \left(\delta\mathbf{u}_\phi^b\right)^T [e\mathbf{K}_{vv}]\,\mathbf{u}_m^b +$$

$$\left(\delta\mathbf{u}_\phi^b\right)^T\left[\left(e^2 + \frac{c^2}{12}\right)\mathbf{K}_{vv}\right]\mathbf{u}_\phi^b, \qquad (2.136)$$

in which

$$\mathbf{K}_{vv} = \frac{G_b A_b}{\Delta x}\mathbf{S}_{vv}. \qquad (2.137)$$

The same procedure can be applied to the xz-shear strain energy, which has contributions from $\frac{\partial \hat{w}}{\partial x}$, $\frac{\partial \phi_y}{\partial x}$ and ϕ_x (*cf.* Eq. (2.122)). For instance:

$$\delta\phi_x\frac{\partial \hat{w}}{\partial x} = \delta\left(\mathbf{u}_\phi^{b\,T}\mathbf{N}_u^b\right)\frac{\partial}{\partial x}\left(\mathbf{N}_w^{b\,T}\mathbf{u}_w^b\right) = \left(\delta\mathbf{u}_\phi^b\right)^T\left[\mathbf{N}_u^b\left(\frac{\partial \mathbf{N}_w^b}{\partial x}\right)^T\right]\mathbf{u}_w^b. \qquad (2.138)$$

Thus,

$$\int_0^{\Delta x} k_b\left(\delta\phi_x\frac{\partial \hat{w}}{\partial x}\right)dx = \left(\delta\mathbf{u}_\phi^b\right)^T\left[k_b\int_0^{\Delta x}\mathbf{N}_u^b\left(\frac{\partial \mathbf{N}_w^b}{\partial x}\right)^T dx\right]\mathbf{u}_w^b =$$

$$\left(\delta\mathbf{u}_\phi^b\right)^T\left(k_b\int_0^{\Delta x}\begin{Bmatrix} 1-\frac{x}{\Delta x} \\ 0 \\ \frac{x}{\Delta x} \\ 0 \end{Bmatrix}\begin{Bmatrix} -\frac{1}{\Delta x} & \frac{1}{\Delta x} \end{Bmatrix}dx\right)\mathbf{u}_w^b = \left(\delta\mathbf{u}_\phi^b\right)^T k_b\begin{bmatrix} -1 & 1 \\ 0 & 0 \\ -1 & 1 \\ 0 & 0 \end{bmatrix}\mathbf{u}_w^b. \qquad (2.139)$$

In order to avoid shear lock, the integral in Eq. (2.139) would normally need to be evaluated through reduced integration. In this case, however, the result would be the same regardless of the number of Gauss points used, as the integrand is a linear polynomial

and is thus integrated exactly for any $N \geq 1$. Nonetheless, reduced integration will be required when evaluating higher-order integrals coming from the xz-shear strain energy. In the present formulation, the only such term is the following:

$$
G_b A_b \int_0^{\Delta x} k_b \delta \phi_x \phi_x \mathrm{d}x = \left(\delta \mathbf{u}_\phi^b\right)^T \left(G_b A_b k_b \int_0^{\Delta x} \begin{Bmatrix} 1 - \frac{x}{\Delta x} \\ 0 \\ \frac{x}{\Delta x} \\ 0 \end{Bmatrix} \begin{Bmatrix} 1 - \frac{x}{\Delta x} \\ 0 \\ \frac{x}{\Delta x} \\ 0 \end{Bmatrix}^T \mathrm{d}x \right) \mathbf{u}_\phi^b =
$$

$$
\left(\delta \mathbf{u}_\phi^b\right)^T \left(\frac{k_b G_b A_b \Delta x}{8} \int_{-1}^{1} \begin{bmatrix} (1-\xi)^2 & 0 & 1-\xi^2 & 0 \\ 0 & 0 & 0 & 0 \\ 1-\xi^2 & 0 & (1+\xi)^2 & 0 \\ 0 & 0 & 0 & 0 \end{bmatrix} \mathrm{d}\xi \right) \mathbf{u}_\phi^b . \tag{2.140}
$$

The integral must be evaluated by one-point Gauss quadrature, which is of the form

$$
\int_{-1}^{1} f(\xi) \mathrm{d}\xi \simeq 2f(0). \tag{2.141}
$$

Hence, Eq. (2.140) becomes

$$
G_b A_b \int_0^{\Delta x} k_b \delta \phi_x \phi_x \mathrm{d}x = \left(\delta \mathbf{u}_\phi^b\right)^T \left(\frac{k_b G_b A_b \Delta x}{4} \begin{bmatrix} 1 & 0 & 1 & 0 \\ 0 & 0 & 0 & 0 \\ 1 & 0 & 1 & 0 \\ 0 & 0 & 0 & 0 \end{bmatrix} \right) \mathbf{u}_\phi^b . \tag{2.142}
$$

The remaining energy terms due to xz-shear, as well as those coming from the linear terms of the axial strain energy, can be derived simply by analytical integration. As there are innumerous energy terms and submatrices, the detailed derivation is herein omitted, especially because the steps for obtaining the submatrices are very similar to what has been done in Eqs (2.133) - (2.139). Ultimately, the virtual strain energy within an element becomes

$$
\int_{V_b^e} \left(\delta \varepsilon_x C_b \varepsilon_x + \delta \gamma_{xy} G_b \gamma_{xy} + \delta \gamma_{xz} \tau_{xz} \right) \mathrm{d}V = \left(\delta \mathbf{u}^b\right)^T \left[\mathbf{k}_0^b + \mathbf{k}_1^b + \mathbf{k}_2^b \right] \mathbf{u}^b . \tag{2.143}
$$

The zeroth-order stiffness is

$$
\mathbf{k}_0^b = \begin{bmatrix} \mathbf{k}_{mm}^b & \mathbf{0} & e\mathbf{k}_{mm}^b \\ \mathbf{0} & \mathbf{k}_{ww}^b & \mathbf{k}_{w\phi}^b \\ \left[e\mathbf{k}_{mm}^b\right]^T & \left[\mathbf{k}_{w\phi}^b\right]^T & \mathbf{k}_{\phi\phi}^b \end{bmatrix}, \tag{2.144}
$$

the elemental submatrices being

$$
\mathbf{k}_{mm}^b = \frac{C_b A_b}{\Delta x} \begin{bmatrix} 1 & 0 & -1 & 0 \\ 0 & 0 & 0 & 0 \\ -1 & 0 & 1 & 0 \\ 0 & 0 & 0 & 0 \end{bmatrix} + \frac{G_b A_b}{\Delta x} \begin{bmatrix} 0 & 0 & 0 & 0 \\ 0 & 1 & 0 & -1 \\ 0 & 0 & 0 & 0 \\ 0 & -1 & 0 & 1 \end{bmatrix}, \tag{2.145}
$$

$$\mathbf{k}_{\phi\phi}^b = \frac{k_b G_b A_b \Delta x}{4} \begin{bmatrix} 1 & 0 & 1 & 0 \\ 0 & 0 & 0 & 0 \\ 1 & 0 & 1 & 0 \\ 0 & 0 & 0 & 0 \end{bmatrix} + \frac{G_b A_b b^2}{12\Delta x} \begin{bmatrix} 0 & 0 & 0 & 0 \\ 0 & 1 & 0 & -1 \\ 0 & 0 & 0 & 0 \\ 0 & -1 & 0 & 1 \end{bmatrix} + \left(e^2 + \frac{c^2}{12} \right) \mathbf{k}_{mm}^b, \quad (2.146)$$

$$\mathbf{k}_{w\phi}^b = \frac{k_b G_b A_b}{2} \begin{bmatrix} 1 & 0 & 1 & 0 \\ -1 & 0 & -1 & 0 \end{bmatrix}, \quad (2.147)$$

$$\mathbf{k}_{ww}^b = \frac{C_b A_b}{\Delta x} \begin{bmatrix} 1 & -1 \\ -1 & 1 \end{bmatrix}. \quad (2.148)$$

The first- and second-order stiffness matrices come from the strain energy due to axial deformation (Eq. (2.123)). The linear contributions from that energy are already accounted for in the zeroth-order matrix, $\mathbf{k}_0^b$. The second-order stiffness, $\mathbf{k}_2^b$, originates from the term

$$C_b A_b \int_0^{\Delta x} \delta \left[\frac{1}{2} \left(\frac{\partial \hat{w}}{\partial x} \right)^2 \right] \frac{1}{2} \left(\frac{\partial \hat{w}}{\partial x} \right)^2 \mathrm{d}x, \quad (2.149)$$

with

$$\delta \left[\frac{1}{2} \left(\frac{\partial \hat{w}}{\partial x} \right)^2 \right] = \left(\frac{\partial \hat{w}}{\partial x} \right) \delta \left(\frac{\partial \hat{w}}{\partial x} \right). \quad (2.150)$$

Hence,

$$C_b A_b \int_0^{\Delta x} \delta \left[\frac{1}{2} \left(\frac{\partial \hat{w}}{\partial x} \right)^2 \right] \frac{1}{2} \left(\frac{\partial \hat{w}}{\partial x} \right)^2 \mathrm{d}x = \frac{C_b A_b}{2} \int_0^{\Delta x} \delta \left(\frac{\partial \hat{w}}{\partial x} \right) \left(\frac{\partial \hat{w}}{\partial x} \right)^2 \left(\frac{\partial \hat{w}}{\partial x} \right) \mathrm{d}x \quad (2.151)$$

As done previously for the linear terms, the FE interpolation for $\hat{w}$ is introduced into Eq. (2.149). Upon doing so, the second-order energy contribution becomes

$$C_b A_b \int_0^{\Delta x} \delta \left[\frac{1}{2} \left(\frac{\partial \hat{w}}{\partial x} \right)^2 \right] \frac{1}{2} \left(\frac{\partial \hat{w}}{\partial x} \right)^2 \mathrm{d}x = \left(\delta \mathbf{u}^b \right)^T \begin{bmatrix} 0 & 0 & 0 \\ 0 & \mathbf{k}_{ww}^{b,2} & 0 \\ 0 & 0 & 0 \end{bmatrix} \mathbf{u}^b = \left(\delta \mathbf{u}^b \right)^T \mathbf{k}_2^b \mathbf{u}^b,$$

$$(2.152)$$

in which

$$\mathbf{k}_{ww}^{b,2} = \frac{1}{2} \left(\frac{\mathbf{b}\mathbf{u}_w^b}{\Delta x} \right)^2 \mathbf{k}_{ww}^b, \quad (2.153)$$

with

$$\mathbf{b} = \{-1 \quad 1\}. \quad (2.154)$$

It is possible to notice from Eq. (2.153) that the second-order stiffness, indeed, depends quadratically upon $\mathbf{u}_w^b$.

The remaining nonlinear terms from the axial strain energy produce the first-order elemental stiffness matrix, which is

$$\mathbf{k}_1^b = \begin{bmatrix} \mathbf{0} & \mathbf{k}_{mw}^{b,1} & \mathbf{0} \\ \left[\mathbf{k}_{mw}^{b,1}\right]^T & \mathbf{k}_{ww}^{b,1} & \left[e\mathbf{k}_{mw}^{b,1}\right]^T \\ \mathbf{0} & e\mathbf{k}_{mw}^{b,1} & \mathbf{0} \end{bmatrix}, \tag{2.155}$$

whose submatrices are

$$\mathbf{k}_{mw}^{b,1} = \frac{C_b A_b \left(\mathbf{b}\mathbf{u}_w^b\right)}{2\left(\Delta x\right)^2} \mathbf{E}, \tag{2.156}$$

$$\mathbf{k}_{ww}^{b,1} = \frac{C_b A_b}{2\left(\Delta x\right)^2} \mathbf{E}^T \left(\mathbf{u}_m^b + e\mathbf{u}_\phi^b\right) \mathbf{b}, \tag{2.157}$$

in which

$$\mathbf{E} = \begin{bmatrix} 1 & 0 & -1 & 0 \\ -1 & 0 & 1 & 0 \end{bmatrix}^T. \tag{2.158}$$

The linear dependence of $\mathbf{k}_1^b$ upon the displacement vectors becomes clear from Eqs. (2.155) - (2.157). Furthermore, from the expressions of $\mathbf{k}_0^b$, $\mathbf{k}_1^b$ and $\mathbf{k}_2^b$, it is possible to notice that the present stiffener model is a very complete one: the zeroth-order matrix accounts for axial motion, torsion, bending, transverse shear deformability and eccentricity effects, whilst the first- and second-order matrices represent geometrical non-linearity.

Obtaining the mass matrices is even simpler than the procedure required for the stiffness matrices, as the inertial term is purely linear. All it takes is substituting Eqs. (2.130) into Eq. (2.125) and rearranging the resulting equation so that the virtual external work over a beam element becomes

$$\delta W_{\text{ext}}^{b,e} = -\left(\delta \mathbf{u}^b\right)^T \mathbf{m}^b \frac{\partial^2 \mathbf{u}^b}{\partial t^2} = -\left(\delta \mathbf{u}^b\right)^T \begin{bmatrix} \mathbf{m}_{mm}^b & \mathbf{0} & e\mathbf{m}_{mm}^b \\ \mathbf{0} & \mathbf{m}_{ww}^b & \mathbf{0} \\ \left[e\mathbf{m}_{mm}^b\right]^T & \mathbf{0} & \mathbf{m}_{\phi\phi}^b \end{bmatrix} \frac{\partial^2 \mathbf{u}^b}{\partial t^2}, \tag{2.159}$$

in which

$$\mathbf{m}_{mm}^b = \frac{\rho_b A_b \Delta x}{6} \begin{bmatrix} 2 & 0 & 1 & 0 \\ 0 & 2 & 0 & 1 \\ 1 & 0 & 2 & 0 \\ 0 & 1 & 0 & 2 \end{bmatrix}, \tag{2.160}$$

$$\mathbf{m}_{ww}^b = \frac{\rho_b A_b \Delta x}{6} \begin{bmatrix} 2 & 1 \\ 1 & 2 \end{bmatrix}, \tag{2.161}$$

and

$$\mathbf{m}_{\phi\phi}^b = \frac{\rho_b A_b \Delta x}{6} \frac{b^2}{12} \begin{bmatrix} 0 & 0 & 0 & 0 \\ 0 & 2 & 0 & 1 \\ 0 & 0 & 0 & 0 \\ 0 & 1 & 0 & 2 \end{bmatrix} + \left(e^2 + \frac{c^2}{12}\right) \mathbf{m}_{mm}^b. \tag{2.162}$$

The kinematic coupling between the panel and the stiffener is already satisfied by the imposed displacement field equations. However, since the plate and the beam have been discretised, they have yet to be numerically coupled. It would be physically correct to sum the respective contributions, e.g., $\mathbf{k}_1 = \mathbf{k}_1^p + \mathbf{k}_1^b$. Nevertheless, this would be mathematically problematic, since the plate and beam elemental matrices have inconsistent dimensions (due to the different number of elemental nodes). One possible solution would be to expand the beam matrices by scattering its elements over larger matrices matching the dimensions of the corresponding plate quantities. However, this would not be a computationally efficient solution, as in nonlinear analysis the stiffness matrices must be constantly re-evaluated, so that every unnecessary operation (summing zeros) can ultimately result in considerable computational overhead.

A more efficient method is to sum the contributions only at the nodes where plate and beam elements meet, and at a submatrix level. For clarity, consider the 35-node mesh shown in Figure 8. Let plate elements $\{9\}$ and $\{13\}$ be the ones formed by nodes $(11, 12, 16, 17)$ and $(16, 17, 21, 22)$, respectively; and beam element $\{1\}$ be the one formed by nodes $(16, 17)$. As a calculation example, let $\mathbf{M}_w$ be the global transverse mass matrix. Then, the entry at position $16,16$ is computed as

$$(M_w)_{16,16} = \left(m_w^{p,\{9\}}\right)_{4,4} + \left(m_w^{p,\{13\}}\right)_{1,1} + \left(m_w^{b,\{1\}}\right)_{1,1}. \tag{2.163}$$

It is completely analogous for the remaining mass and stiffness submatrices. Refer again to Figure 8 for more details on the correspondence between local (elemental) and global nodes for the example at hand here.

After assembling the contributions from all the plate and beam elements, the resulting ODE system is

$$\mathbf{M\ddot{U}} + (\mathbf{K}_0 + \mathbf{K}_1 + \mathbf{K}_2)\,\mathbf{U} = \mathbf{F}. \tag{2.164}$$

Note that now the matrices have no superscripts (p or b), meaning that they represent total (beam + plate) quantities.

2.4 Aerodynamic model

The supersonic aerodynamic load is modelled by the first-order piston theory. This method is derived from supersonic potential flow theory by neglecting convolution and high-order terms. According to it, the pressure field acting over the panel can be approximated as (BISMARCK-NASR, 1992)

$$\Delta p\left(\hat{w}(x, y, t)\right) = -\frac{2q}{\sqrt{M^2 - 1}}\left[\frac{\partial \hat{w}}{\partial y} + \left(\frac{M^2 - 2}{M^2 - 1}\right)\frac{1}{U}\frac{\partial \hat{w}}{\partial t}\right], \tag{2.165}$$

in which U, q and M are the free-stream velocity, dynamic pressure and Mach number, respectively. The simplicity of this theory becomes clear from Eq. (2.165), in which it is

possible to see that the aerodynamic pressure is linearly related to the panel's instantaneous shape and velocity. It is also a local theory, as the pressure at any point is assumed to depend exclusively on the values of $\frac{\partial \hat{w}}{\partial y}$ and $\frac{\partial \hat{w}}{\partial t}$ at that very spot. For these reasons, this model avoids the need for fluid meshes, thereby rendering the resulting aeroelastic system considerably simpler than CFD-based solvers – and also making computations extremely cheaper.

Of course, this model has limitations. The accuracy of piston theory for panel flutter problems is considered to be satisfactory for $M > 1.7$ (ALDER, 2015; VEDENEEV, 2012). For lower Mach numbers, nonlocal theories are recommended. Therefore, the analyses performed in the present work are quantitatively accurate for high-supersonic regimes only. For such cases, Alder (2015) has recently compared the post-flutter response of a panel (with von Karman structural non-linearity) using two different aerodynamic models: the linear piston theory and the Euler equations (using finite volumes). He concluded that the latter high-fidelity CFD approach yields LCO amplitudes which are very similar to those obtained via piston theory, differing in around 3%. Therefore, despite being linear and very simple, the first-order piston theory is suitable for parametric assessment of LCO amplitudes, which is the focus of the present work.

In order to make parametric studies simpler, Eq. (2.165) can be conveniently rewritten as

$$\Delta p = -\lambda \left(\frac{D}{L^3} \right) \frac{\partial \hat{w}}{\partial y} - g_a \left(\rho h \omega_0 \right) \frac{\partial \hat{w}}{\partial t}, \tag{2.166}$$

in which ω_0 is a reference frequency and D is a reference flexural stiffness, namely,

$$\omega_0 = \sqrt{\frac{D}{\rho h L^4}}, \tag{2.167}$$

and

$$D = \frac{h^3 E_1}{12 \left(1 - \nu_{12} \nu_{21} \right)} \tag{2.168}$$

Moreover, analyses are normally parametrised with respect to two dimensionless coefficients: the dimensionless dynamic pressure, λ, and the damping factor, g_a, namely

$$\lambda = \frac{2 q L^3}{D \sqrt{M^2 - 1}}, \tag{2.169}$$

and

$$g_a = \sqrt{\frac{\lambda \mu}{\sqrt{M^2 - 1}}} \left(\frac{M^2 - 2}{M^2 - 1} \right) \simeq \sqrt{\frac{\lambda \mu}{M}}, \tag{2.170}$$

in which $\mu = \frac{L \rho_\infty}{h \rho}$ is the mass ratio.

The work done by the pressure field over a virtual displacement field is

$$\delta W_{\text{ext}}^{\text{flow}} = \int_A \left(\delta \hat{w} \Delta p \right) \mathrm{d}A = \sum_{\text{plate elements}} \int_{\Omega_e} \left(\delta \hat{w} \Delta p \right) \mathrm{d}A. \tag{2.171}$$

Then, as has been done for the inertial terms in section 2.2, the nodal interpolation $\hat{w} = \mathbf{N}_w{}^T \mathbf{u}_w = \mathbf{u}_w{}^T \mathbf{N}_w$ is introduced into Eq. (2.171) so as to yield (after assembly)

$$\delta W_{\text{ext}}^{\text{flow}} = -\delta \mathbf{U}^T \left(\lambda \mathbf{K}_a \mathbf{U} + g_a \mathbf{C}_a \dot{\mathbf{U}} \right), \tag{2.172}$$

in which $\lambda \mathbf{K}_a$ and $g_a \mathbf{C}_a$ are the aerodynamic stiffness and damping matrices, respectively, whose corresponding elemental quantities are

$$\mathbf{k}_a = \frac{D}{L^3} \begin{bmatrix} 0 & 0 & 0 \\ 0 & \int_{\Omega_e} \mathbf{N}_w \left(\frac{\partial \mathbf{N}_w}{\partial y} \right)^T \mathrm{d}A & 0 \\ 0 & 0 & 0 \end{bmatrix}, \tag{2.173}$$

$$\mathbf{c}_a = \rho h \omega_0 \begin{bmatrix} 0 & 0 & 0 \\ 0 & \int_{\Omega_e} \mathbf{N}_w \mathbf{N}_w{}^T \mathrm{d}A & 0 \\ 0 & 0 & 0 \end{bmatrix}. \tag{2.174}$$

It becomes evident that piston theory maintains its simplicity after discretised: the aerodynamic load is ultimately translated into two matrices that can be readily introduced into the pre-existing structural model. The complete aeroelastic equations of motion are, thus,

$$\mathbf{M}\ddot{\mathbf{U}} + g_a \mathbf{C}_a \dot{\mathbf{U}} + \left(\lambda \mathbf{K}_a + \mathbf{K}_0 + \mathbf{K}_1 + \mathbf{K}_2 \right) \mathbf{U} = \mathbf{F}, \tag{2.175}$$

with $\mathbf{F}$ generally set as zero for aeroelastic analysis.

The low computational cost enabled by the use of linear piston theory makes it a powerful tool for parametric studies that require rapid assessment of post-flutter amplitudes – provided, of course, that a nonlinear structural model is employed. The methods used for solving the aeroelastic problem is dealt with in section 2.5.

2.5   Solution methods

Before introducing the solution procedures, let Eq. (2.175) be rewritten as

$$\mathbf{M}\ddot{\mathbf{U}} + \left[\mathbf{G} \left(\lambda, \frac{\mu}{M} \right) \right] \dot{\mathbf{U}} + \left[\mathbf{K} \left(\lambda \right) + \mathbf{H}(\mathbf{U}) \right] \mathbf{U} = \mathbf{F}, \tag{2.176}$$

in which

$$\mathbf{K} \left(\lambda \right) = \lambda \mathbf{K}_a + \mathbf{K}_0, \tag{2.177}$$

$$\mathbf{G} \left(\lambda, \frac{\mu}{M} \right) = \sqrt{\frac{\lambda \mu}{M}} \mathbf{C}_a, \tag{2.178}$$

and

$$\mathbf{H}(\mathbf{U}) = \mathbf{K}_1(\mathbf{U}) + \mathbf{K}_2(\mathbf{U}). \tag{2.179}$$

This shows that, for fixed material properties and geometry, the aeroelastic system depends on two parameters: λ and μ/M, which essentially represent the flight condition.

There are two solutions of interest: a) the flutter boundary, or critical condition, which is the highest value of λ for which the system presents damped motion; and b) the post-flutter behaviour, which is the nonlinear transient response for flight conditions beyond the flutter boundary. However, before actually solving the aeroelastic equations, it is necessary to apply the boundary conditions (BCs), as the stiffness matrices, *per se*, are singular.

2.5.1 Boundary conditions

The most efficient way to enforce zero-displacement boundary conditions is to eliminate rows and columns from the matrices and vectors in Eq. (2.176). For instance, suppose that the system has n degrees of freedom, meaning that vector $\mathbf{U}$ has n entries. If, say, the k-th degree of freedom in $\mathbf{U}$ (e.g., the transverse displacement at a certain node) is known to be zero, then the k-th column and the k-th row of all the matrices (mass, stiffness and damping), as well the k-th entry in $\mathbf{U}$, $\dot{\mathbf{U}}$ and $\ddot{\mathbf{U}}$, are eliminated. This will lead to an ODE system whose dimension is now equal to $(n-1)$.

Three types of BCs are considered herein: clamped, simply supported and symmetry boundaries. The simplest one is the clamped condition: a clamped edge satisfies $\hat{u} = \hat{v} = \hat{w} = \phi_x = \phi_y = 0$ at all of its nodes. The simple support is similar, but the rotation about the edge is released. The symmetry condition consists of restricting perpendicular displacements and parallel rotations, as illustrated in Figure 9.

Figure 9 – Application of symmetry BCs to a symmetric problem.
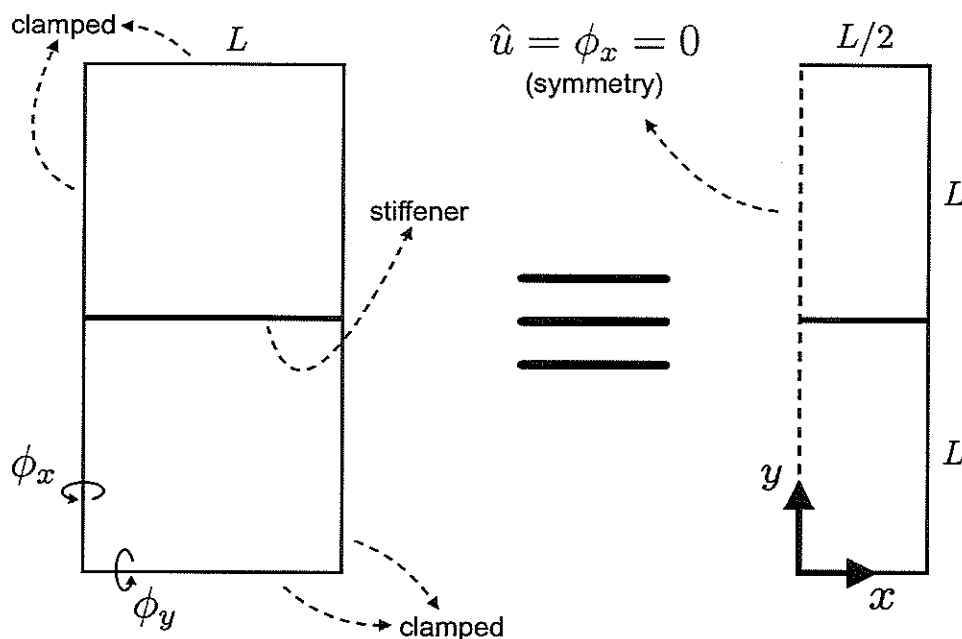
Source: Elaborated by the author.

In the panel flutter problem, the existence of mathematical symmetry requires symmetry of: material properties, flow direction, boundary conditions and initial conditions. Symmetry, when applicable, is a powerful tecnhique for reducing computational time, as it reduces the number of nodes and DOFs in the system. In the present work, symmetry BCs are used whenever possible, which is the case of isotropic and cross-ply panels.

2.5.2 Flutter boundary prediction

One of the most important results to be obtained from an aeroelastic system is the flutter boundary, or stability boundary, which is the critical condition from which limit cycle oscillations start to occur. Let λ_f be the dimensionless dynamic pressure that corresponds to the flutter boundary. Then, for $\lambda < \lambda_f$, the system is expected to display damped motion. This means that, after possible perturbations to the static equilibrium, the panel should vibrate and gradually return to its static condition. For $\lambda > \lambda_f$, the panel should undergo limit cycle oscillations, which are periodic motions with limited amplitude. This so-called post-flutter regime is where non-linearities dominate the aeroelastic motion.

The value of λ_f can be obtained by solving the linear problem, i.e., by dropping the nonlinear stiffness, $\mathbf{H}$ (XUE; MEI, 1993a). Besides, what is typically done is to fix a value for μ/M, so that the resulting linear system relies on only one parameter (λ):

$$\mathbf{M}\ddot{\mathbf{U}} + [\mathbf{G}\left(\lambda\right)]\dot{\mathbf{U}} + [\mathbf{K}\left(\lambda\right)]\mathbf{U} = 0, \tag{2.180}$$

which can be rearranged as a first-oder ODE system:

$$\dot{\mathbf{q}} - [\mathbf{R}\left(\lambda\right)]\mathbf{q} = 0, \tag{2.181}$$

in which

$$\mathbf{R}\left(\lambda\right) = \begin{bmatrix} \mathbf{0} & [\mathbf{M}^{-1}\mathbf{M}] \\ [-\mathbf{M}^{-1}\mathbf{K}\left(\lambda\right)] & [-\mathbf{M}^{-1}\mathbf{G}\left(\lambda\right)] \end{bmatrix}, \tag{2.182}$$

and

$$\mathbf{q} = \begin{Bmatrix} \mathbf{U} \\ \dot{\mathbf{U}} \end{Bmatrix}. \tag{2.183}$$

The linear ODE system can be solved by assuming a solution of the form $\mathbf{q}(t) = e^{\omega t}\mathbf{q}_0$, with $\mathbf{q}_0 \neq \mathbf{0}$, and substituting it in Eq. (2.181), which yields the classical eigenvalue problem:

$$\det\left[\mathbf{R}\left(\lambda\right) - \omega\mathbf{I}\right] = 0, \tag{2.184}$$

in which $\mathbf{I}$ is the identity matrix. The general solution consists of complex eigenvalues:

$$\omega = \omega_{\text{re}} + i\omega_{\text{im}}. \tag{2.185}$$

If, for a certain λ, all the eigenvalues have negative real parts $(\omega_{\text{re}} < 0)$, then all the aeroelastic modes are damped, which means that there is no flutter at such flight

condition. Otherwise, if at least one of the eigenvalues have a negative real part, then the system's response to any disturbance should display growing amplitude, i.e., flutter (BISMARCK-NASR, 1992). The flutter boundary, λ_f, is the value of λ for which Eq. (2.184) yields purely imaginary frequencies, that is, $\omega_{re} = 0$ for all modes. In practical terms, this can be done by solving Eq. (2.184) for successively increasing values of λ and assessing the sign of ω_{re}. If one of the ω_{re} changes sign between, say, λ_j and λ_{j+1}, then $\lambda_j \leq \lambda_f \leq \lambda_{j+1}$. Then, the value of λ_f can be sought within that shorter interval. This can be done iteratively until λ_f is found within desirable tolerance. Note that the task at hand is very similar to a root-finding problem, hence there are several possible algorithms for numerically determining λ_f.

Predicting the flutter boundary is crucial for the present study, as it determines when transient analysis is required. For $\lambda < \lambda_f$, the panel does not undergo flutter and should return to static equilibrium after perturbed, so there is no need for spending computational resources in simulating its time response. Beyond the flutter boundary, it is necessary to simulate the aeroelastic system in the time domain (including the non-linearities) in order to assess LCO amplitudes and vibration patterns.

2.5.3 Transient analysis

The solution of the nonlinear aeroelastic ODE system in Eq. (2.176) requires numerical time marching. Through the course of this work, several algorithms were implemented, such as the third- and fourth-order explicit Runge-Kutta methods, and varations of the implicit Newmark method. Tests were performed using benchmark nonlinear structural vibration and flutter problems, leading to the conclusion that the modified Newmark method proposed by Akay (1980) is the most efficient one for the present problem.

The method starts by selecting a time step Δt and expanding the displacement and velocity vectors at time $t_{n+1} = (n+1)\Delta t$ as

$$\dot{\mathbf{U}}_{n+1} = \dot{\mathbf{U}}_n + \frac{\Delta t}{2}\left(\ddot{\mathbf{U}}_{n+1} + \ddot{\mathbf{U}}_n\right), \tag{2.186}$$

and

$$\mathbf{U}_{n+1} = \mathbf{U}_n + \Delta t\dot{\mathbf{U}}_n + \left(\frac{\Delta t}{2}\right)^2 \left(\ddot{\mathbf{U}}_{n+1} + \ddot{\mathbf{U}}_n\right), \tag{2.187}$$

in which $\mathbf{U}_n$ is short for $\mathbf{U}\left(t = t_n\right)$. Equations (2.186) and (2.187) can be combined so as to attain new relations:

$$\ddot{\mathbf{U}}_{n+1} = -\ddot{\mathbf{U}}_n + \frac{4}{\Delta t^2}\left(\mathbf{U}_{n+1} - \mathbf{U}_n - \Delta t\dot{\mathbf{U}}_n\right), \tag{2.188}$$

and

$$\dot{\mathbf{U}}_{n+1} = -\dot{\mathbf{U}}_n + \frac{2}{\Delta t}\left(\mathbf{U}_{n+1} - \mathbf{U}_n\right), \tag{2.189}$$

which can be substituted into Eq. (2.176), thereby forming the time-discretised equation:

$$\left(\hat{\mathbf{K}} + \frac{\Delta t^2}{4}\mathbf{H}_{n+1}\right)\mathbf{U}_{n+1} = \frac{\Delta t^2}{4}\mathbf{F}_{n+1} + \hat{\mathbf{P}}_n, \qquad (2.190)$$

with

$$\hat{\mathbf{K}} = \mathbf{M} + \frac{\Delta t}{2}\mathbf{G} + \frac{\Delta t^2}{4}\mathbf{K}, \qquad (2.191)$$

$$\hat{\mathbf{P}}_n = \mathbf{M}\left[\mathbf{U}_n + \Delta t\dot{\mathbf{U}}_n + \frac{\Delta t^2}{4}\ddot{\mathbf{U}}_n\right] + \mathbf{G}\left[\frac{\Delta t}{2}\mathbf{U}_n + \frac{\Delta t^2}{4}\dot{\mathbf{U}}_n\right], \qquad (2.192)$$

and $\mathbf{H}_{n+1} = \mathbf{H}\left(\mathbf{U} = \mathbf{U}_{n+1}\right)$. Assuming a constant (for structural vibration studies) or zero (for flutter analysis) force vector, then $\mathbf{F}_{n+1} = \mathbf{F}$.

It is important to note that, for each time instant, Eq. (2.190) is a nonlinear algebraic system, as $\mathbf{H}_{n+1}$ is a function of $\mathbf{U}_{n+1}$. The iterative approach proposed by Akay (1980) for solving it consists of moving the nonlinear term, $\frac{\Delta t^2}{4}\mathbf{H}_{n+1}\mathbf{U}_{n+1}$, to the right-hand side of Eq. (2.190) and treating it as a forcing term. Hence, the $(k+1)$-th iteration for an $(n+1)$-th time step is computed as (CHEN; SUN, 1985)

$$\hat{\mathbf{K}}\mathbf{U}_{n+1}^{(k+1)} = \hat{\mathbf{F}}_n - \frac{\Delta t^2}{4}\mathbf{H}_{n+1}^{(k)}\mathbf{U}_{n+1}^{(k)}, \qquad (2.193)$$

in which

$$\hat{\mathbf{F}}_n = \frac{\Delta t^2}{4}\mathbf{F} + \mathbf{M}\left[\mathbf{U}_n + \Delta t\dot{\mathbf{U}}_n + \frac{\Delta t^2}{4}\ddot{\mathbf{U}}_n\right] + \mathbf{G}\left[\frac{\Delta t}{2}\mathbf{U}_n + \frac{\Delta t^2}{4}\dot{\mathbf{U}}_n\right]. \qquad (2.194)$$

The iterations should continue until a sufficiently accurate solution at each time step is achieved.

The computational efficiency of this modified iterative time-marching scheme lies in the fact that the coefficient matrix, $\hat{\mathbf{K}}$, is constant at all times and iterations, so that it only needs to be inverted once, during pre-processing. Therefore, the new solution can be straightforwardly calculated from the previous iteration:

$$\mathbf{U}_{n+1}^{(k+1)} = \left(-\frac{\Delta t^2}{4}\hat{\mathbf{K}}^{-1}\mathbf{H}_{n+1}^{(k)}\right)\mathbf{U}_{n+1}^{(k)} + \left(\hat{\mathbf{K}}^{-1}\hat{\mathbf{F}}\right). \qquad (2.195)$$

Since no inversion of the nonlinear stiffness matrix is required, the CPU time spent at each time step is drastically reduced when compared to classical Runge-Kutta methods.

At each time step, the values used when $k = 0$ correspond to the converged values from the previous time step, that is, $\mathbf{U}_{n+1}^{(0)} = \mathbf{U}_n$. After convergence, the values of $\ddot{\mathbf{U}}_n$ and $\dot{\mathbf{U}}_n$ are updated using Eqs (2.188) and (2.186). Note that initial conditions must be provided for $\mathbf{U}$, $\dot{\mathbf{U}}$ and $\ddot{\mathbf{U}}$.

This variation of the Newmark scheme is very efficient, but this comes as a trade-off for unconditional stability (AKAY, 1980). This means that this method is conditionally

stable, i.e., a minimum time step is required for convergence. For nonlinear analysis, especially when aerodynamic terms are involved, there is no closed-form solution for determining this minimum Δt. Many different estimates are proposed in the literature. One that has worked for all the analyses conducted herein is the one by Leech (1965):

$$\Delta t = \frac{1}{\omega_0} \left(\frac{\overline{\Delta x}}{2L} \right)^2 , \tag{2.196}$$

in which $\overline{\Delta x}$ is the minimum element size in the mesh.

3 VALIDATION AND VERIFICATION

3.1 Introduction

Before beginning the analysis of novel cases, it is crucial to validate the finite element model and very the solution algorithms implemented. In order to do that, results obtained through the present model are compared to those from the scientific literature. The validation/verification is carried out in multiple levels: starting with nonlinear structural vibration (*in vacuo*) of composite panels, then moving to linear and nonlinear panel flutter, including linear flutter prediction in beam-reinforced panels.

3.2 Nonlinear plate vibration

In order to verify the present nonlinear plate model against the available literature, results have been generated for simply supported square cross-ply panels subject to a uniform step load, i.e.,

$$\Delta p(x, y, t) = \begin{cases} 0, & \text{for } t < 0; \\ p_0, & \text{for } t \geq 0. \end{cases} \tag{3.1}$$

For the mesh convergence study, a two-ply ($[0° \ 90°]$) moderately thick plate is considered with the following parameters:

$$\frac{L}{h} = 10, \quad \frac{p_0}{E_2}\left(\frac{h}{L}\right)^4 = 50, \quad \nu_{12} = 0.25,$$

$$\frac{E_1}{E_2} = 25, \quad \frac{G_{12}}{E_2} = \frac{G_{13}}{E_2} = 0.5, \quad \frac{G_{23}}{E_2} = 0.2.$$

The validation parameter is the central transverse displacement, w_c, taken at the first peak of the oscillatory motion. Several different FE meshes of the form $\frac{n}{2} \times n$ are considered, i.e., half-plate symmetry is used. The coarsest mesh corresponds to $n = 6$, and the finest one has $n = 50$. Instead of using Leech's formula (Eq. (3.1)) to define the time step for each mesh, the same step has been fixed for all the meshes. The selected step is $\Delta t = \frac{3.3 \times 10^{-4}}{\omega_0}$, or, nondimensionally, $\Delta \tau = 3.3 \times 10^{-4}$. The results are given in terms of w_c/h *versus n*. Mind that $n = \frac{L}{\Delta x}$, as the meshes are uniform. From Figure 10 it is possible to verify that the solution clearly converges as the mesh is refined. Since no closed-form solution is available for this case, error convergence analyses are not performed. However, the solution at $n = 24$ has a 0.2% difference from the solution at $n = 50$, which makes it possible to conclude that the 12×24 mesh is sufficiently fine for delivering accurate nonlinear vibration solutions.

Furthermore, Figure 11 shows the transient solution in comparison with those from Chen and Sun (1985) and Reddy (1983), who also used the Newmark time-marching

scheme, but a higher-order (9-node) quadrilateral element. The comparison reveals good agreement between the present solution and results from the literature – especially those by Chen and Sun (1985). The results are plotted in dimensionless time, namely,

$$\tau = \omega_0 t. \tag{3.2}$$

Figure 10 – FE mesh convergence for a nonlinear vibrating plate.
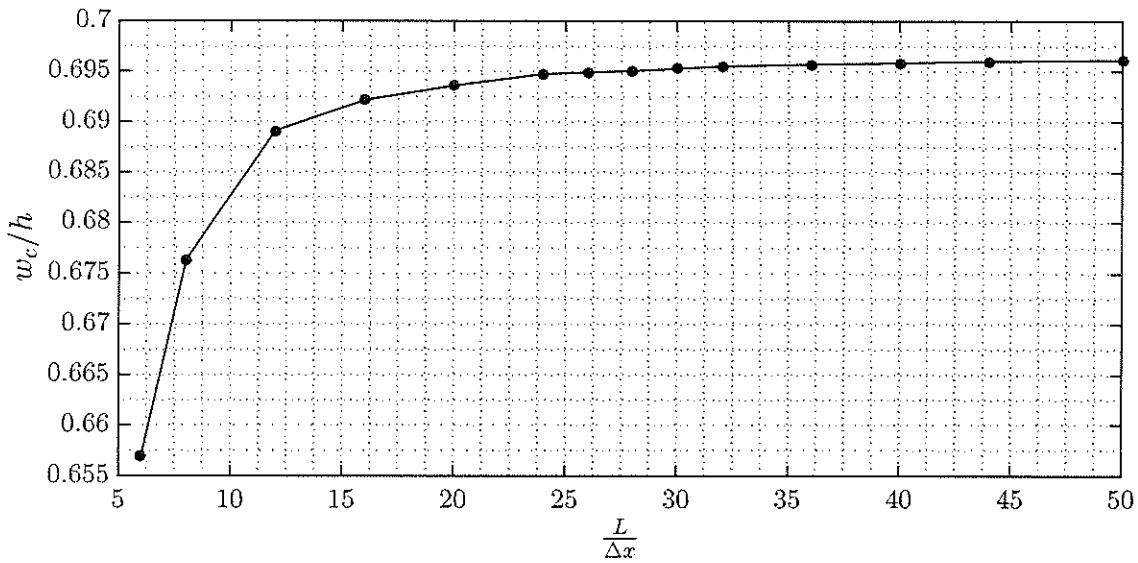
Source: Elaborated by the author.

In order to make sure that the present model is lock-free, i.e., that the reduced integration technique effectively prevents shear lock, a thin-plate solution has also been compared to results from Chen and Sun (1985). The forced vibration of a ten-ply ($[0°\ 90°\ 0°\ 90°\ 0°]_s$) plate has been simulated, with the following parameters:

$$\frac{L}{h} = 100, \quad \frac{p_0}{E_2}\left(\frac{h}{L}\right)^4 = 124, \quad \nu_{12} = 0.3,$$

$$\frac{E_1}{E_2} = 15.19, \quad \frac{G_{12}}{E_2} = \frac{G_{13}}{E_2} = \frac{G_{23}}{E_2} = 0.6962.$$

A 12 × 24 half-plate mesh has been used. Figure 12 exhibits the comparison. Once again, the present solution matches almost exactly the results from Chen and Sun (1985). This demonstrates that the method is indeed lock-free, and corroborates the satisfactory accuracy provided by the 12 × 24 mesh.

Figure 11 – Nonlinear vibration of a cross-ply asymmetric moderately thick plate.
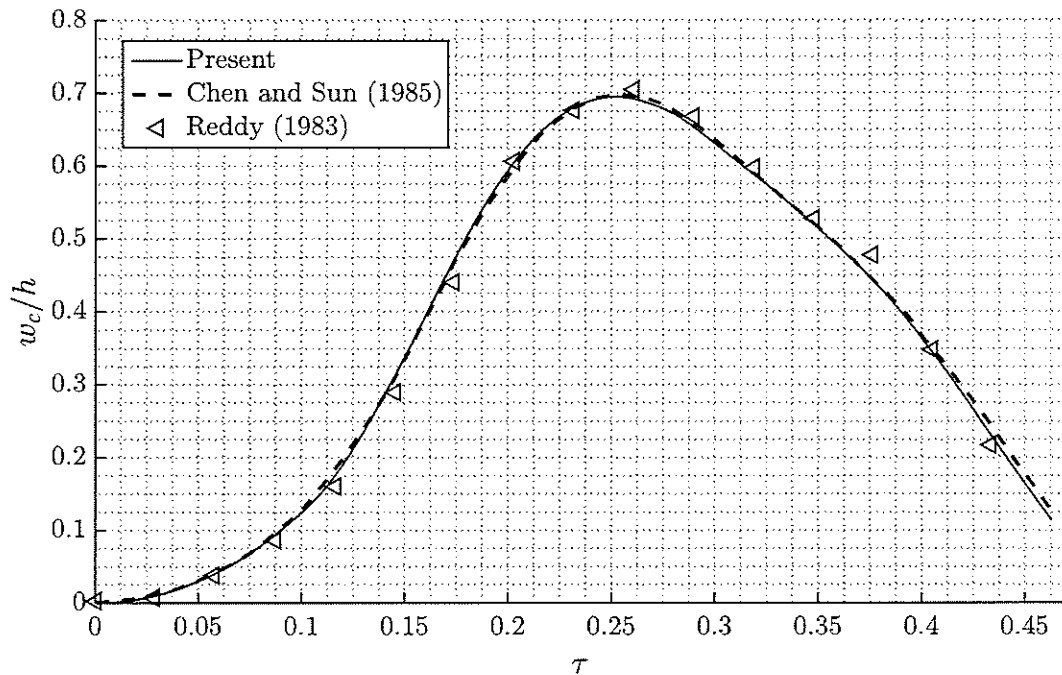
Source: Elaborated by the author.

3.3 Aeroelastic solutions

### 3.3.1 Linear flutter in a multibay composite panel

In order to validate the aeroelastic model, and also to verify results for oblique laminations (rather than only cross-ply plates), the flutter boundary of a three-bay panel has been calculated for different fiber orientation angles. The expression *three-bay panel* refers to a simply supported $L \times 3L$ panel with two additional support lines that subdivide it in three bays, as illustrated in Figure 13. Panels in which internal stiffeners are replaced by simple supports are usually called *multibay panels*.

Following the analysis conducted by Shiau and Chang (1991), flutter boundary results have been generated for lamination sequences of the form $[\theta \ \text{-}\theta \ \theta \ \text{-}\theta \ \theta]_s$, with $\theta = 20°, 40°, 60°, 80°$. A 24×72 mesh has been considered, and the geometric and material parameters are

$$\frac{L}{h} = 100, \quad \frac{\mu}{M} = 0, \quad \nu_{12} = 0.21, \quad \frac{E_1}{E_2} = 26.5, \quad \frac{G_{12}}{E_2} = \frac{G_{13}}{E_2} = \frac{G_{23}}{E_2} = 1.184.$$

Figure 14 depicts the present results and those by Shiau and Chang (1991), who employed a thin-plate FE model. The plot relates the angle θ and the critical dynamic pressure, λ_f. The comparison reveals good agreement, despite the use of different structural models.

Figure 12 – Nonlinear vibration of a cross-ply symmetric thin plate.
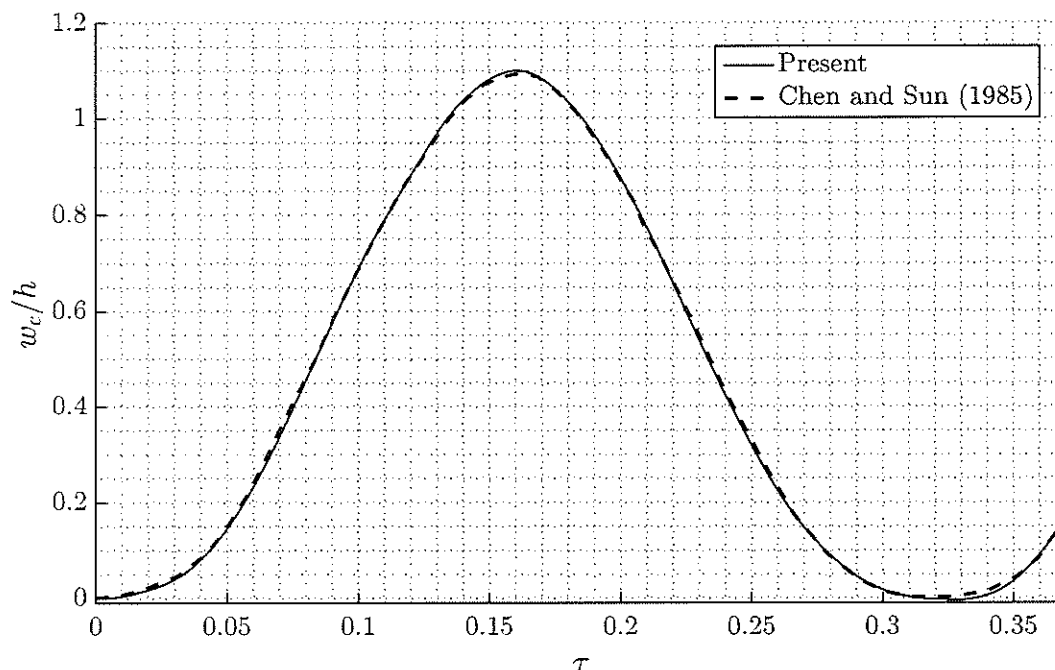
Source: Elaborated by the author.

Figure 13 – Representation of a three-bay panel.
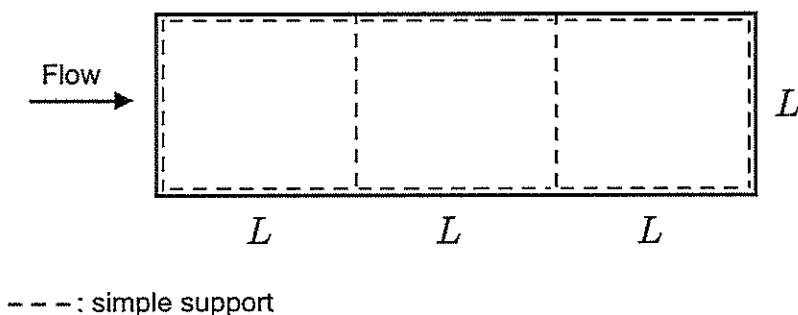
Source: Elaborated by the author.

3.3.2 Linear flutter in reinforced panels

The next stage in the aeroelastic validation involves flutter on actual beam-reinforced panels. Flutter boundary results generated by the present model are compared to those from Liao and Sun (1993), who used three-dimenional degenerated elements for both the panel and the stiffener. The geometries considered for comparison are depicted in Figure 15. All the panels are square, fully clamped and isotropic.

Figure 14 – Flutter boundary as a function of fiber orientation, for a three-bay panel.
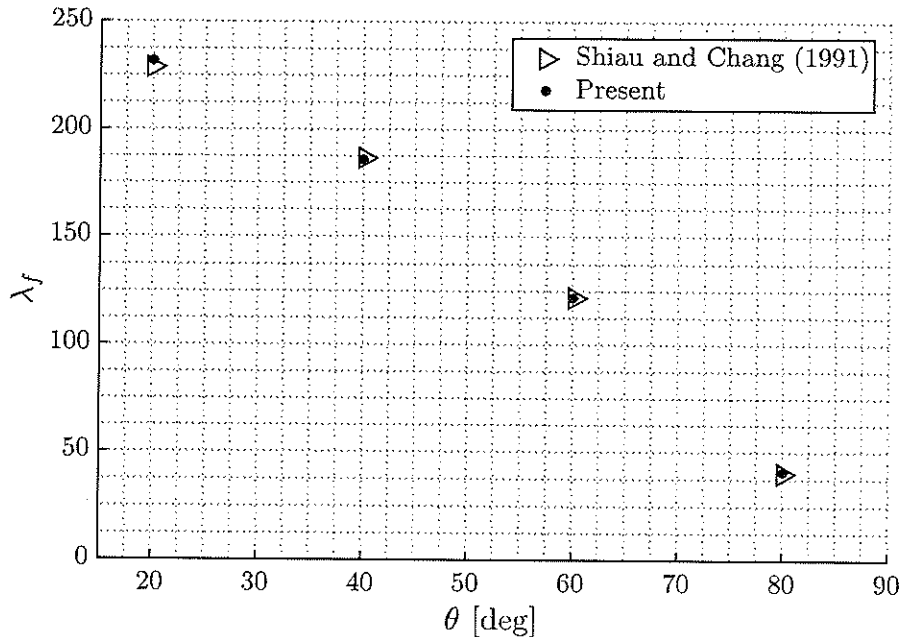
Source: Elaborated by the author.

However, before starting the analyses, it is important to investigate mesh convergence for the stiffened-panel model. In order to do that, the flutter boundary values for Case A (*c.f.* Figure 15) are plotted against the mesh size, $\frac{\Delta x}{L}$. From Figure 16, it is possible to observe that the solution converges. The value of λ_f for a 20 × 20 mesh is 854.3, which is 1.32% higher than the result obtained by Fernandes and Tamijani (2017) via the Ritz method. For a 24 × 24 mesh, this difference reduces to 0.6%. This shows, once again, that $n = 24$ provides sufficent accuracy for the purposes of the present work.

Taking that into consideration, flutter boundary results obtained by using a 24 × 24 mesh are compared in Table 2 to those from Liao and Sun (1993). The comparison reveals good agreement between the solutions, for all the geometries considered. The small discrepancy is probably due to the differences in modelling, as Liao and Sun (1993) used a shell model for the panel, and considered one additional degree of freedom for the beam.

Table 2 – Flutter boundaries for stiffened isotropic panels.

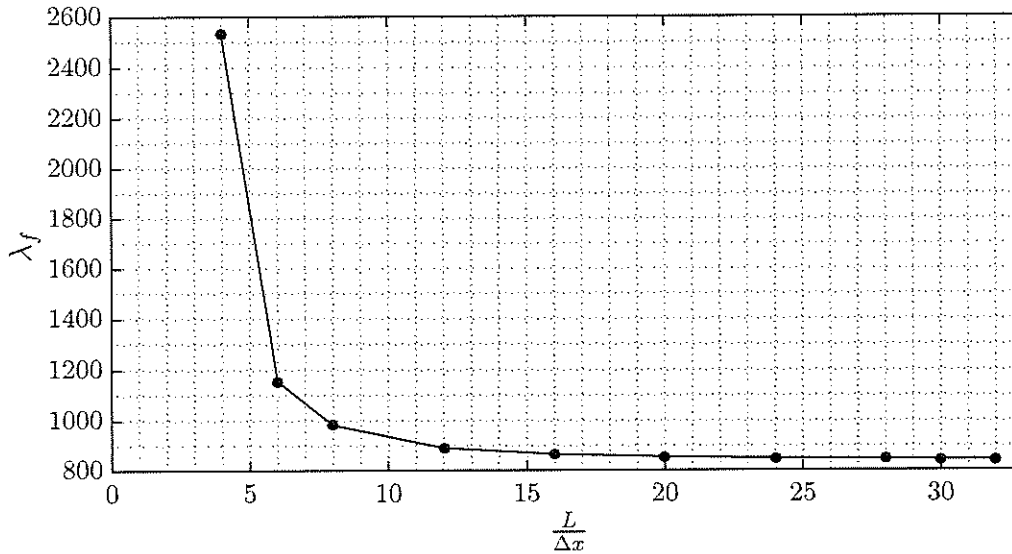| Geometry	λ_f (Present)	λ_f (LIAO; SUN, 1993)	Difference
Case A	848.31	840.716	0.90%
Case B	1449.2	1434.209	1.04%
Case C	1176.3	1172.723	0.31%

Source: Elaborated by the author.

Figure 15 – Reinforced panels considered in the validation study.
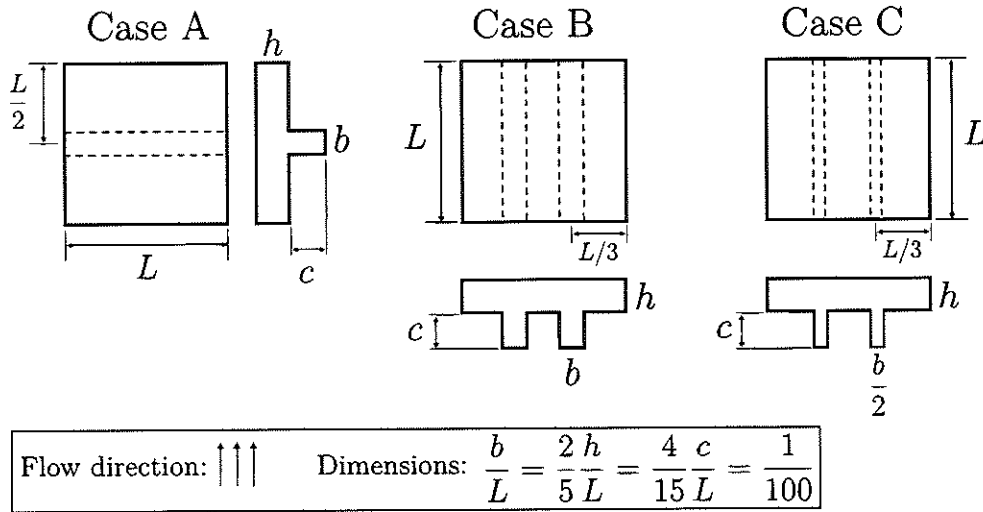
Source: Elaborated by the author.

Figure 16 – Convergence study: Flutter boundary for stiffened isotropic panels.
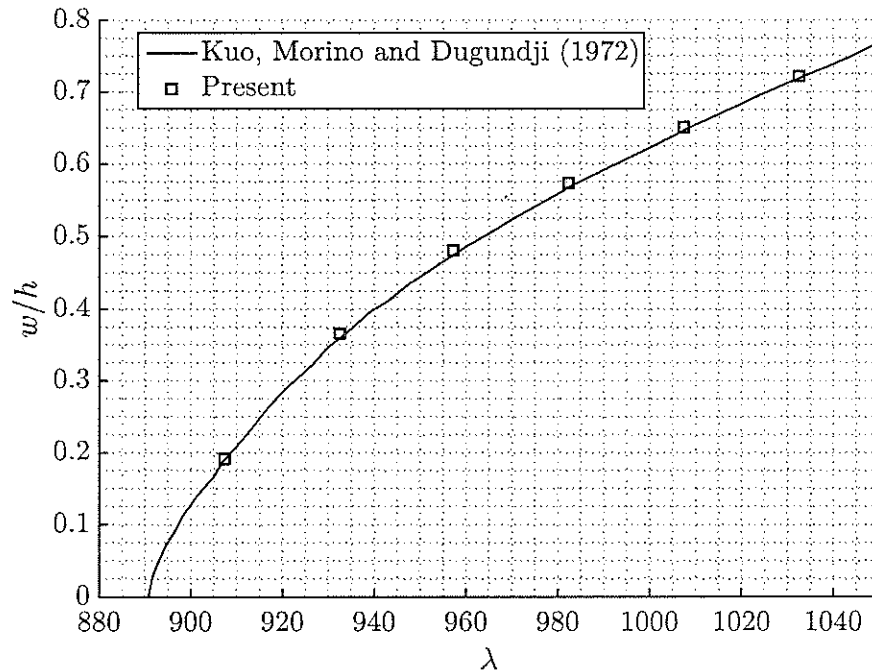

Source: Elaborated by the author.

3.3.3 Nonlinear flutter in single panels

In order to verify the nonlinear aeroelastic model, an unstiffened clamped isotropic square panel has been simulated in time at post-flutter dynamic pressures, i.e., $\lambda > \lambda_f$. It has been assumed that $\nu = 0.25$ and $\frac{\mu}{M} = 0.1$. Results have been compared to those obtained by Kuo, Morino and Dugundji (1972) through perturbation method. Figure 17 reveals very good agreement between the LCO amplitudes attained by the present model

and those from the reference.

Figure 17 – LCO amplitudes for an isotropic clamped square panel ($\nu = 0.25$, $\frac{\mu}{M} = 0.1$)

Source: Elaborated by the author.

3.3.4 Summary and remarks

The validation/verification study carried out in this chapter demonstrates that the present aeroelastic model has been correctly formulated and implemented, being capable of accurately reproducing results from the scientific literature. The computer code created for this work involves several numerical techniques: the Finite Element Method for spatial discretisation, gaussian quadrature for numerical integration, an iterative Newmark-type scheme for time-marching, root-finding algorithms for determining linear stability boundaries. Although each of these methods provides approximate results, the accuracy of the ultimate aeroelastic solutions has proven very satisfactory. The solutions yielded by discretising square panels into 24×24 elements have shown to generally differ in less than 1% from results reported in the literature. Thus, $\Delta x = \frac{L}{24}$ is henceforth considered as the standard element size for analyses. This means, for instance, that an $L \times 2L$ stiffened plate (i.e., a double panel) is meshed with 24×48 elements. If symmetry is used, then only 12×48 elements are used.

4 AEROELASTIC ANALYSIS OF REINFORCED PANELS

4.1 Introduction

The main goal of this project is to provide a systematic comparative study between stiffened (coupled) and single (isolated) panels, with respect to various aspects of their aeroelastic behaviour. Two factors can yield differences between these two models: a) The flexibility/mobility of stiffeners; and b) Cell-cell coupling, i.e., adjacent cells interacting structurally. If a stiffener is sufficiently rigid, it should provide, in practice, a clamped-like restriction, which means that it will neither move nor allow the cells to exchange moments, forces, rotation, etc. Therefore, it ultimately comes down to the stiffness of the reinforcement, that is, how rigid the stiffener must be for one to be able to safely model each cell in a reinforced panel as a single, isolated, ideally-restrained panel.

A neat way to carry out such analysis is to parametrise results in terms of the stiffener's height-to-thickness ratio. Consider that the length and cross-sectional area of the stiffener are fixed, thereby fixing its weight. Then, its cross-sectional aspect ratio is the only parameter that can affect its bending and torsional stiffnesses and inertias (minding that a rectangular cross-section is being considered in the present work, for neatness and simplicity). Therefore, the analyses performed in the present work have the cross-sectional aspect ratio as an important structural parameter.

Furthermore, the present study considers double panels, i.e., $L \times 2L$ panels with a stiffener fixed at $y = L$ (cf. Figure 7 and Figure 3). The aeroelastic behaviour of each of the two square cells is compared to that of a single, isolated square panel. A detailed study is carried out for isotropic panels, considering linear behaviour, nonlinear response and component-wise mechanical energy quantification. Laminated panels are also investigated in the nonlinear regime in terms of limit cycle amplitudes. Analyses are parametrised in terms of nonlinear dynamic pressures and the stiffener's cross-sectional aspect ratio.

4.2 Flutter boundary

The examination of Eq. (2.146) reveals that the linear bending and torsional moments of inertia for an eccentric beam element are, respectively,

$$I_y = \left(\frac{c^2}{12} + e^2 \right) A_b, \tag{4.1}$$

and

$$I_t = \left(\frac{c^2 + b^2}{12} + e^2 \right) A_b, \quad \text{with} \quad e = \frac{c + h}{2}. \tag{4.2}$$

Let α be the stiffener's cross-sectional aspect ratio, namely,

$$\alpha = \frac{c}{b}. \tag{4.3}$$

Thus, if the cross-sectional area, A_b, is fixed, then Eqs. (4.1) and (4.2) can be rewritten as

$$I_y(\alpha) = \left(4\alpha + 6h\sqrt{\frac{\alpha}{A_b}} + \frac{3h^2}{A_b}\right)\frac{A_b^2}{12}, \tag{4.4}$$

and

$$I_t(\alpha) = \left(4\alpha + 6h\sqrt{\frac{\alpha}{A_b}} + \frac{1}{\alpha} + \frac{3h^2}{A_b}\right)\frac{A_b^2}{12}. \tag{4.5}$$

It is clear that

$$\lim_{\alpha\to\infty} I_y(\alpha) = \lim_{\alpha\to\infty} I_t(\alpha) = \infty, \tag{4.6}$$

which reveals that both torsional and bending stiffnesses tend to become very large for sufficiently slender cross-sections. It is thus of interest to study how the flutter boundary of a double panel varies with respect to α. Consider andouble stiffened isotropic panel with $\frac{L}{h} = 100$ and $\frac{\mu}{M} = 0.02$. Also consider the following properties for the stiffener, arbitrarily defined: $A_b = 20h^2$, $\rho_b = 3\rho$, $E_b = 3E_1$ and $\nu_b = \nu = 0.25$ (the quantities without subscripts refer to the plate). Figure 18 shows the parametric flutter boundary assessment for such panel. The results reveal that the flutter boundary of the stiffened panel asymptotically approaches that of a single clamped square panel. This is a direct consequence of how the beam's stiffness varies with respect to α: as α becomes progressively larger, the stiffener tends to approximate a clamped line, so that each cell tends to behave as an isolated panel. Another important conclusion that can be drawn from these resullts is the fact that the single-panel model is an unconservative one, at least as far as the onset of flutter is concerned. In other words, modelling each cell in a skin structure as an isolated panel may lead to highly-overestimated flutter speeds, which can result in structural unsafety.

Figure 18 – Flutter boundary of a double panel for different cross-sectional aspect ratios.
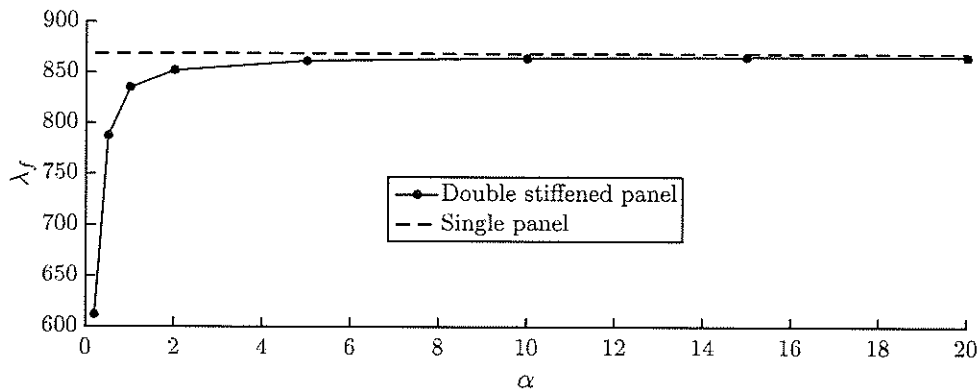
Source: Elaborated by the author.

4.3 Nonlinear aeroelastic response

Linear analysis has revealed that the discrepancies between the single- and stiffened-panel models increase as the cross-sectional aspect ratio decreases. It may not be as simple in the post-flutter regime, due to the presence of non-linearities. Solutions have been generated for several values of λ and α, including isotropic (especially) and laminated panels.

4.3.1 Isotropic panels

In order to investigate the nonlinear aeroelastic regime, the same isotropic panel from section 4.2 has been simulated at post-flutter conditions, that is, $\lambda > \lambda_f$. At such conditions, even the smallest perturbation should lead the system to periodically vibrate in what is called limit cycle oscillations. So, as initial condition, a very small displacement field is input, corresponding to the application of a uniform pressure $\Delta p_0 = 0.01 E_2 \left(h/L \right)^4$, which is then removed.

Transient solutions have been generated for several values of α, and the maximum and minimum transverse displacements are shown in Figure 19. The reference point where LCO amplitudes are taken is $y = \frac{3L}{4} + L$ at the symmetry line, which corresponds to the midspan three-quarter position in the rear cell. Once again, the results are compared to those from a single panel, taken at $y = \frac{3L}{4}$.

Figure 19 – Maximum and minimum LCO displacements for several values of λ and α.
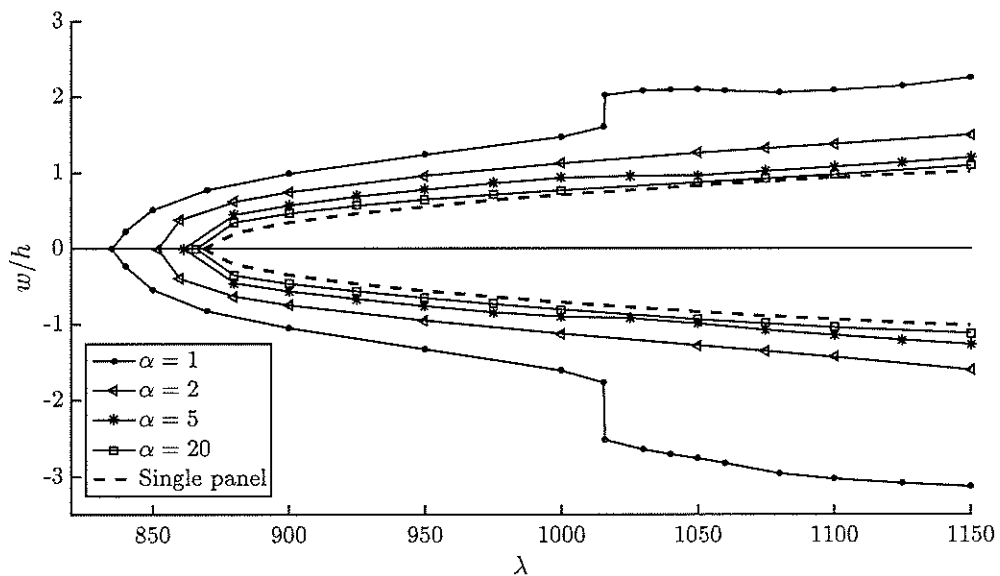
Source: Elaborated by the author.

As expected, for large values of α the cell responds similarly to a single, clamped

panel. The magnitudes of the maximum and minimum displacements increase as α decreases, which is also a direct consequence of how the beam stiffness is related to α. The single panel model is, thus, a lower bound for the LCO amplitude levels and an upper bound for the flutter boundary (*cf.* section 4.2). In practical terms, this means that simulating isolated fluttering panels is an unconservative approach when dealing with reinforced skin.

It is also possible to verify, from Figure 19, that the maximum and minimum displacements can differ, which is explained by the stiffener's eccentricity. Yet the most remarkable feature from the LCO plot is perhaps the sudden jump in amplitude observed for $\alpha = 1$. Similar discontinuities have been identified by the author in previous works (PACHECO; MARQUES; FERREIRA, 2017; PACHECO; MARQUES; FERREIRA, 2018; PACHECO et al., 2017). Through a detailed sequential continuation study, it was proved that such jumps are actually bifurcation points related to the coexistence of multiple stable limit cycles at certain dynamic pressures. This means that, under special initial conditions, the branch that existed before the jump can be continued (PACHECO; MARQUES; FERREIRA, 2017), but the branch seen after the jump in Figure 19 is generally more stable.

Let λ_{jump} be the condition at which the solution bifurcates. Figure 20 depicts the fluttering shapes for $\lambda = 1015.5 < \lambda_{\text{jump}}$ and $\lambda = 1015.7 > \lambda_{\text{jump}}$. The fluttering shape is an instantaneous shot of the panel's midspan deformed shape, taken when the reference point is at a peak of its LCO. It is possible to see that the relative position between the cells is very different prior to and after the jump, i.e., the flutter mechanism changes at the jump. As a matter of fact, a quick examination of Figure 21 shows that the relative phase between the cells changes considerably. The LCO displacements presented are taken at points $y = \frac{3L}{4}$, $y = L$ and $y = \frac{3L}{4} + L$, which are located in the front cell, the stiffener and the rear cell, respectively, along the midspan (symmetry) line. In order to improve viewing, the displacements at each of those reference points have been divided by their respective maximum LCO displacements. It is clear that the stiffener and the front cell vibrate practically in phase both prior to and after the jump, but the phase of the rear cell changes considerably. Before the jump, the rear cell vibrates roughly in antiphase with the front cell and the stiffener. This type of opposed motion is not uncommon in stiffened panels in nonlinear aeroelastic regimes. It has been observed by Oh, Lee and Lee (2001) and also by the author in previous works (PACHECO; MARQUES; FERREIRA, 2017; PACHECO et al., 2017). However, after the jump, the motion is more similar to a 90°-phase vibration, i.e., the refence points located at the front cell and the stiffener reach their peaks when the reference point of the rear cell is close to a zero-displacement position.

Two hypotheses are plausible, in theory, for explaining why the reference cell

Figure 20 − Midspan fluttering shapes prior to and after the jump.
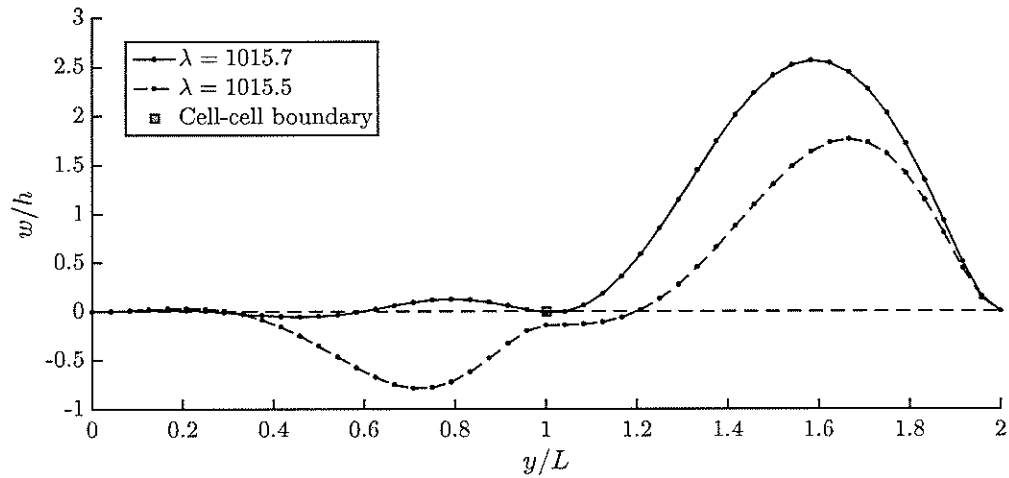
Source: Elaborated by the author.

Figure 21 − Normalised LCO amplitudes. (a) $\lambda = 1015.5$; (b) $\lambda = 1015.7$.
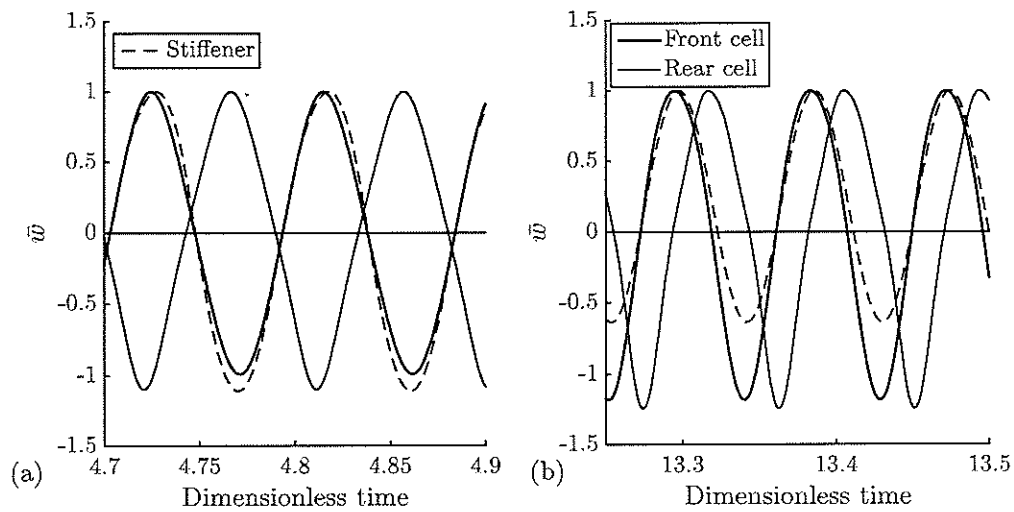
Source: Elaborated by the author.

displays highly discrepant LCO amplitudes for virtually identical dynamic pressures: a) The energy transfer from the flow to the structure is more severe in the post-jump flutter mechanism; or b) The total mean energy prior to and after the jump is the same, but the cells and the stiffener exchange the available energy between themselves in such a way as to yield larger amplitudes. In order to determine the answer, it is necessary to calculate

the mechanical energy (kinetic plus elastic) instantaneously stored in the structure:

$$E_m(t) = \int_{V+V_b} \left[\left(\frac{\partial u}{\partial t}\right)^2 + \left(\frac{\partial v}{\partial t}\right)^2 + \left(\frac{\partial w}{\partial t}\right)^2 \right] \frac{\rho}{2} dV +$$
$$\int_V \frac{\boldsymbol{\sigma}_p{}^T \boldsymbol{\varepsilon}_p + \boldsymbol{\sigma}_s{}^T \boldsymbol{\varepsilon}_s}{2} dV + \int_{V_b} \frac{\sigma_x \varepsilon_x + \tau_{xy}\gamma_{xy} + \tau_{xz}\gamma_{xz}}{2} dV, \tag{4.7}$$

which after discretisation becomes

$$E_m(t) = \frac{1}{2}\dot{\mathbf{U}}^T \mathbf{M}\dot{\mathbf{U}} + \frac{1}{2}\mathbf{U}^T \left[\tilde{\mathbf{K}}\left(\mathbf{U}_w\right) \right] \mathbf{U}, \tag{4.8}$$

with

$$\tilde{\mathbf{K}}\left(\mathbf{U}_w\right) = \mathbf{K}_0 + \mathbf{K}_1\left(\mathbf{U}_m = \mathbf{U}_\phi = 0\right) + \frac{1}{2}\mathbf{K}_2\left(\mathbf{U}\right). \tag{4.9}$$

The energy can be nondimensionalised as:

$$\bar{E} = \frac{E_m}{D\left(h/L\right)^2}. \tag{4.10}$$

The mechanical energy can also be calculated locally – rear cell, front cell, stiffener – by integrating in specific elements in the mesh. The total and component-wise energies have been computed for $\lambda = 1015.5$ and $\lambda = 1015.7$. The results are exhibited in Figure 22 and Figure 23. The total mean energy is clearly much higher after the jump than prior to it. This means that the post-jump flutter mechanism is capable of extracting more energy from the flow. It is possible to conclude from Figure 22 that the jump happens because the system moves from one limit cycle to a more energetic one. A difference of less than 0.01% in the dynamic pressure – from 1015.5 to 1015.7 – is sufficient for changing the flutter mechanism and taking the system to a considerably more energetic motion. This is not unusual, and is a consequence of the non-linearity of the aeroelastic system. For instance, Shishaeva, Vedeneev and Aksenov (2015) recently found out that, at certain flow conditions, a fluttering panel can undergo two distinct limit cycles at the same dynamic pressure.

Furthermore, Figure 23 reveals important information about the energy distribution in the stiffened panel. In both pre- and post-jump conditions, the mean energy contained by the front cell is considerably lower than that of the rear cell. This makes perfect sense, since rear cells tend to vibrate with larger amplitudes in *in tandem* panel arrangements (PACHECO et al., 2017). Also, the energy absorbed by the stiffener is negligible when compared to the energy absorbed by the panel.

Since panels with more rigid stiffeners ($\alpha = 2, 5, 20$) showed no jump, it is very reasonable to conclude that the mobility of the stiffener is directly related to the discontinuity. Moreover, as the energy stored in the stiffener is very small, it is possible to conclude that the stiffener influences the aeroelastic motion more as a "dynamic boundary condition" than as an energy absorber. Therefore, in spite of moving with very small amplitudes and

Figure 22 – Pre- and post-jump energy time histories.
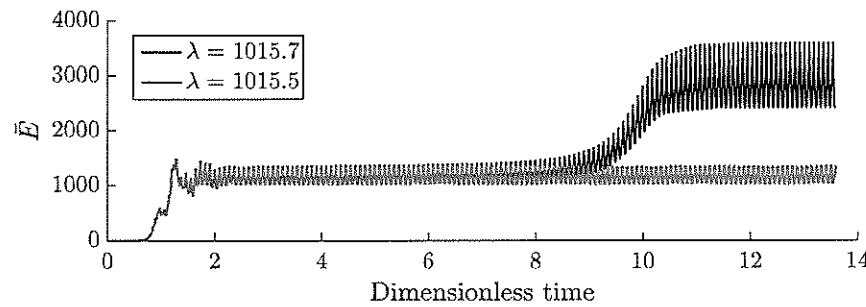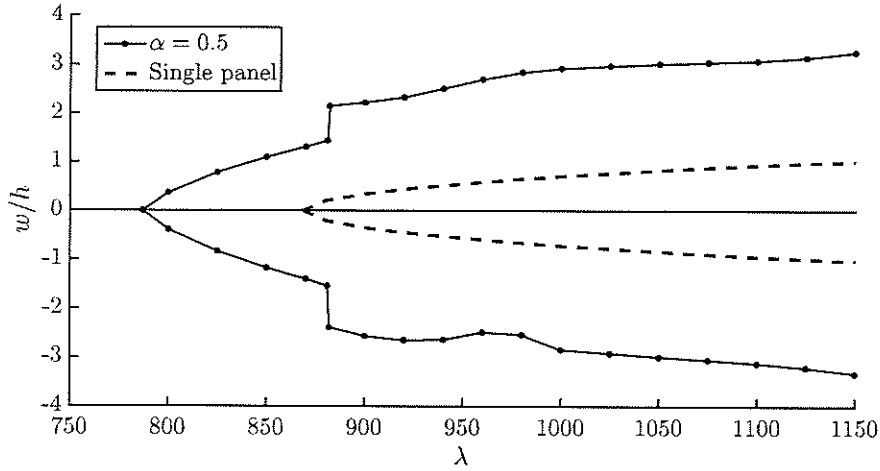

Source: Elaborated by the author.

Figure 23 – Component-wise LCO energy. (a) $\lambda = 1015.5$; (b) $\lambda = 1015.7$.
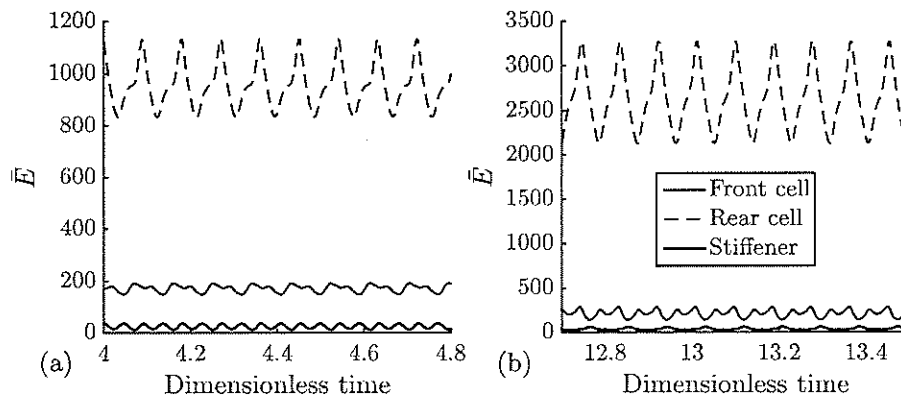
Source: Elaborated by the author.

storing very little energy, the stringer's dynamics can substantially affect the aeroelastic motion of the whole system. Figure 24 shows the LCO amplitude plot for $\alpha = 0.5$. A jump similar to what happened for $\alpha = 1$ can be seen here, but the discontinuity occurs earlier for this more flexible stiffener. Hence it is possible to conclude that stiffener mobility plays indeed an extremely important role on the aeroelastic motion.

It becomes clear, from the present analysis, that neglecting stiffener flexibility can result in unsafe structural design. The LCO amplitudes – and, consequently, strains and stresses – predicted by considering ideal restrains (single plate) can be substantially lower than in an actual reinforced panel. Moreover, the amplitude jumps observed in "weakly-stiffened" panels offer pontential risks if not predicted carefully. It is common for aircraft design philosophies to allow for some level of cycling before inspection and maintenance. Therefore, reliable calculation of oscillation frequencies and strain/stress levels is crucial for structural design and, for this reason, sudden amplitude jumps are definitely undesirable.

Figure 24 – LCO amplitudes for a panel with a very flexible stiffener.
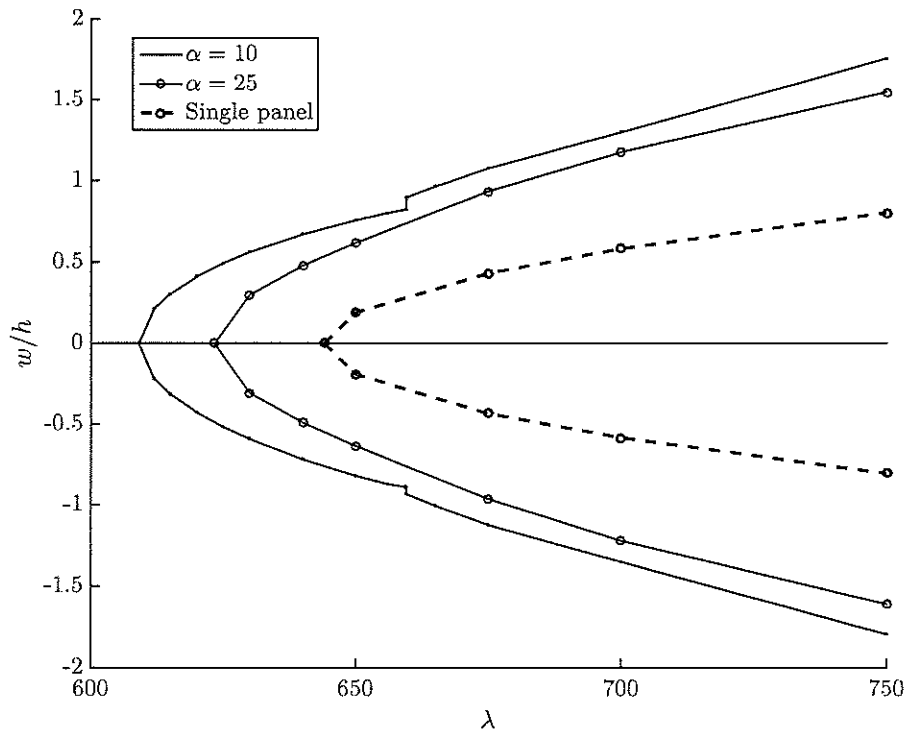

Source: Elaborated by the author.

4.3.2 Laminated panels

Analyses have also been performed for composite panels. The material properties considered here for the laminated plates are those of boron-epoxy as found in Dixon and Mei (1993): $\frac{E_1}{E_2} = 10$, $\frac{G_{12}}{E_2} = \frac{1}{3}$ and $\nu_{12} = 0.3$. It is assumed that $G_{13} = G_{23} = G_{12}$, $\frac{\mu}{M} = 0.05$ and $\frac{L}{h} = 100$. The stiffener is considered to be made of aluminium, so that $\frac{\nu_b}{\nu_{12}} = 1$, $\frac{\rho_b}{\rho} = 1.35$ and $\frac{E_b}{E_1} = \frac{1}{3}$. The cross-sectional area is taken as $A_b = (4h)^2$.

Nonlinear transient response has been simulated for a three-layer symmetric cross-ply plate ([0° 90° 0°]). The LCO amplitude diagrams for $\alpha = 10$ and $\alpha = 25$ are shown in Figure 25, in comparison to those from a single panel. The trend observed in isotropic panels is confirmed: a double panel can display extremely-larger amplitudes when compared to an idealised single panel. Moreover, a more flexibile stiffener ($\alpha = 10$) has yielded discontinuities in the LCO amplitude diagrams. In this case, the jump appears to be somewhat less intense than for the isotropic panel. The phase portraits depicted in Figure 26 reveal that indeed there are no drastic changes to the dynamic motion after this jump.

The cases simulated so far have considered cells positioned in tandem, in which the structural coupling occurs along the flow direction. In order to investigate spanwise coupling, a stiffened angle-ply ([45° -45°]) panel has been simulated with the flow aligned with the x direction, which is done by simply changing $\frac{\partial}{\partial y}$ for $\frac{\partial}{\partial x}$ in Eq. (2.173). Figure 27 illustrates the reference points, P1 and P2, where displacements are taken, and the amplitude plot for $\alpha = 1$ is shown in Figure 28. It is possible to see that, even for this low aspect ratio, each cell in the stiffened panel behaves very similarly to a single isolated panel. This happens because in this case none of the layers has fibers aligned with the flow direction, which renders the panel considerably less resistant to the aerodynamic load

Figure 25 – LCO amplitude plots for a cross-ply stiffened panel ([0° 90° 0°]).
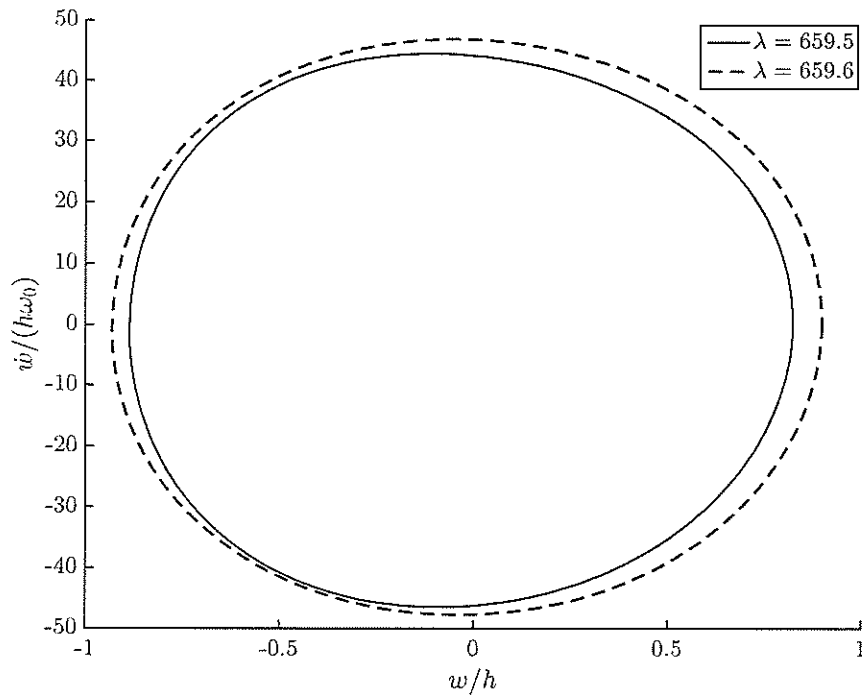

Source: Elaborated by the author.

when compared to a cross-ply panel. Therefore, even at low aspect ratios the stiffener is considerably more rigid than the plate.

Even for $\alpha = 0.1$, the amplitudes of the double panel are not drastically discrepant from those of a single panel, as shown in Figure 29. Note that, although the problem is not symmetric about the reinforcement line, the two cells vibrate with very similar amplitudes for a wide range if dynamic pressures. There is no apparent jump in this case, yet the dynamics do change as λ increases. Figure 30 and Figure 31 depict the relative LCO motion of points P1 and P2 at $\lambda = 200$ and $\lambda = 400$, respectively. For the smaller dynamic pressure, the phase between the cells is very small, and so is the amplitude difference, as also seen in Figure 32. However, at $\lambda = 400$ the phase becomes larger, meaning that, despite the inexistence of an abrupt, jump-like change, the flutter dynamics do vary as a function of the dynamic pressure.

4.3.3 Remarks

Through linear analysis, Shiau and Chang (1991) concluded that fiber orientation and stacking sequence play a major role in the aeroelastic response of reinforced panels. They showed that, depending on the material arrangement, spanwise coupling can be

Figure 26 – Pre- and post-jump phase portraits for the cross-ply panel, with $\alpha = 10$.
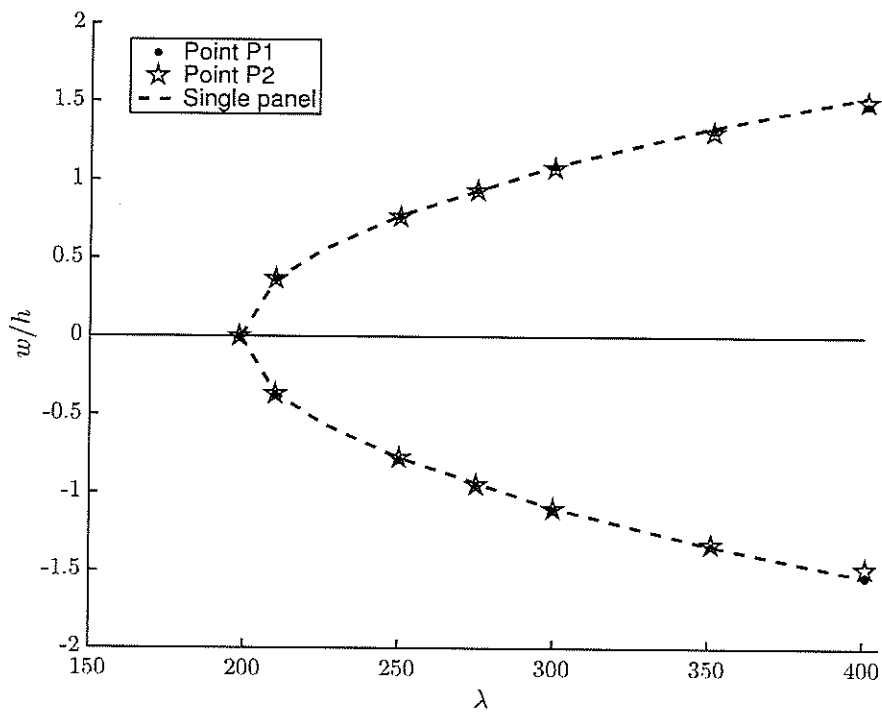

Source: Elaborated by the author.

as important as streamwise coupling, which is not true for isotropic panels. The present nonlinear study has revealed that the post-flutter response is also highly influenced by these factors. Of course, it would be ideal to simulate several lamination schemes and geometrical arrangements (triple/multiple panels, spanwise plus streamwise coupling, composite stiffeners, non-square cells, etc), but in practical situations there are infinite combinations of material properties, stacking sequences, stiffener geometries, number of cells, flow angle, among other parameters. In spite of this, it is possible to conclude that the cases presented and thoroughly analysed here are sufficient to demonstrate that the single-panel model cannot be used indiscriminately without a careful examination on how rigid specific stiffeners are when compared to the skin panels. Reinforced panels have been shown to exhibit potentially complex aeroelastic behaviour that cannot be predicted when idealised fixation/isolation is considered.

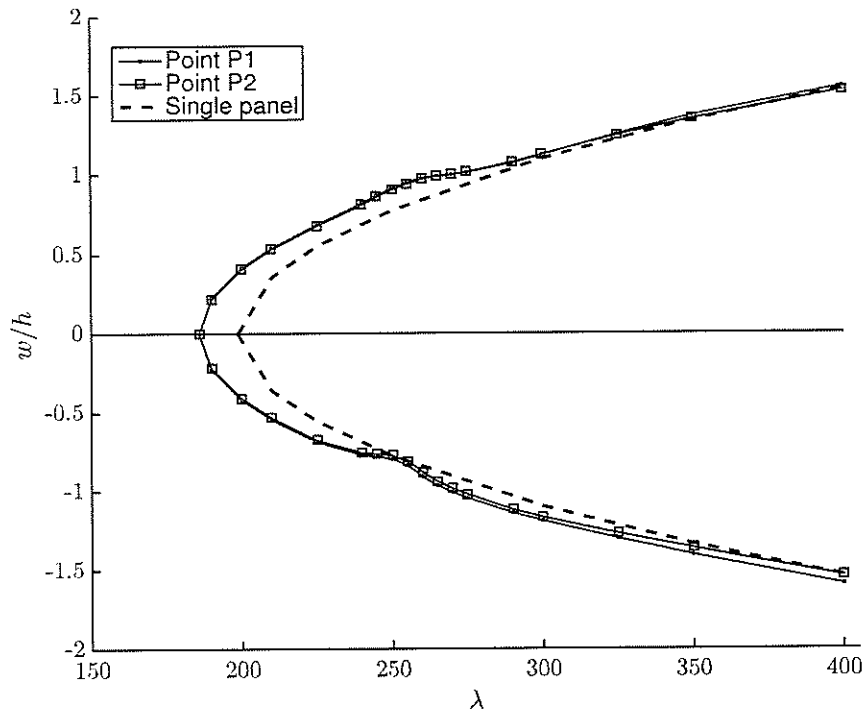Figure 27 – Reference points and schematic representation for a spanwise arrangement.
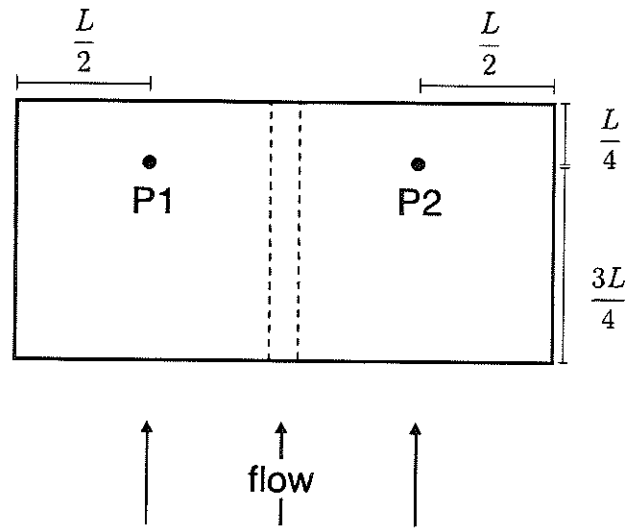
Source: Elaborated by the author.
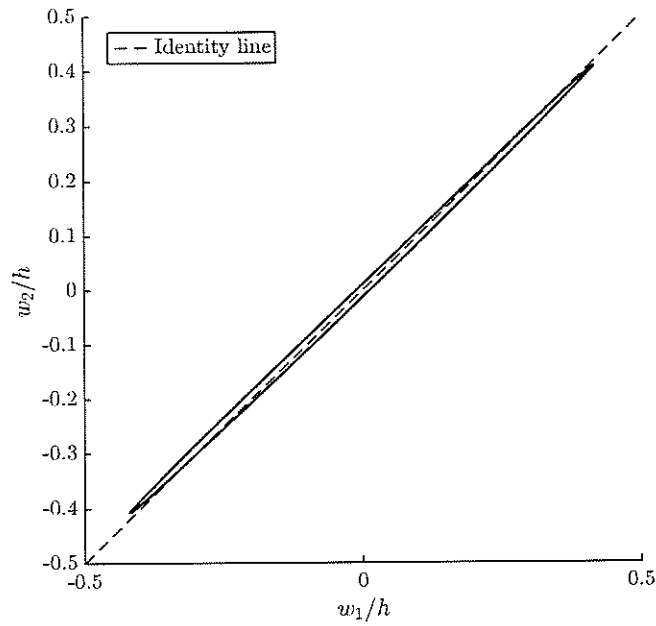
Figure 28 – LCO amplitude plots for an angle-ply stiffened panel (spanwise) with $\alpha = 1$.

Source: Elaborated by the author.

Figure 29 – LCO amplitude plots for an angle-ply stiffened panel (spanwise) with $\alpha = 0.1$.

Source: Elaborated by the author.

Figure 30 – Transverse LCO displacements at points P1 and P2, for $\lambda = 200$.

Source: Elaborated by the author.

Figure 31 – Transverse LCO displacements at points P1 and P2, for $\lambda = 400$.
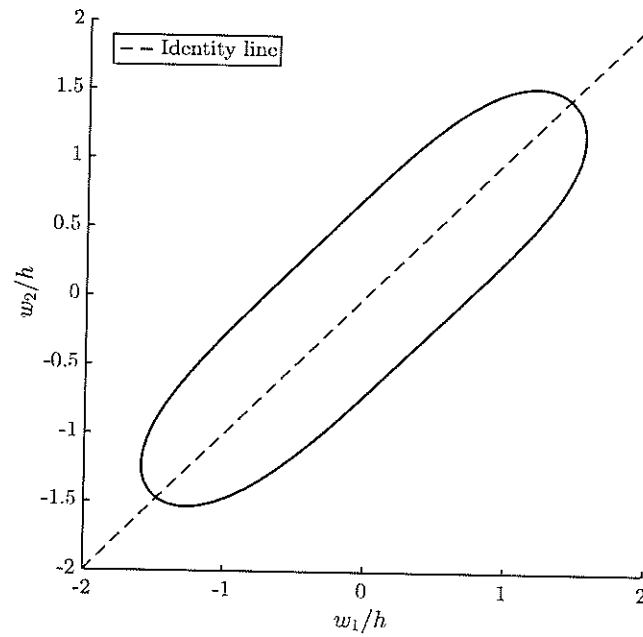
Source: Elaborated by the author.

Figure 32 – Fluttering shape of a spanwise-double panel at $\lambda = 200$, with $\alpha = 0.1$.
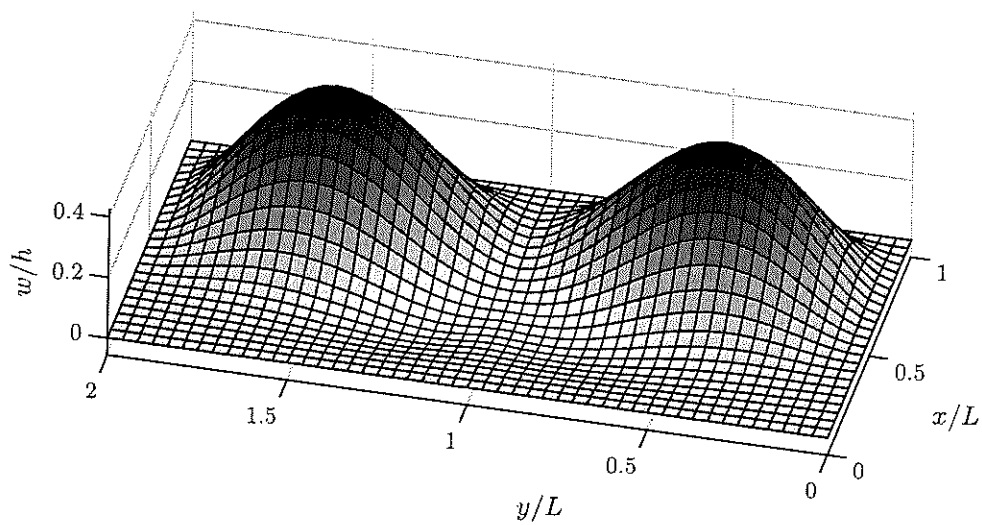

Source: Elaborated by the author.

5 CONCLUSIONS SUMMARY

This work has presented a numerical investigation on the linear and nonlinear (especially) aeroelastic behaviour of reinforced aircraft skin panels subject to one-sided supersonic flow. The main goal was to develop and implement a computer code (formulation, model and solvers) for flutter analysis in beam-reinforced panels, in order to study potentially complex behaviour of such aerospace structural elements.

The aeroelastic model employs the Mindlin plate theory to simulate the skin, and an eccentric Timoshenko beam theory for the stiffening elements. Geometrical non-linearity is included by the von Karman strain-displacement relations, for both plate and beam. The model is formulated so as to consider isotropic and composite panels. The aerodynamic load is computed via first-order piston theory, which is a linear model suitable for high-supersonic regimes. The structural and aerodynamic theories are combined by the Principle of Virtual Work, which in turn is discretised using the Finite Element Method. The plate and beam models are nodally coupled through the global stiffness and mass matrices. There are two types of solutions of interest: a) Flutter boundary prediction, which consists of finding the maximum dynamic pressure that the system can withstand without experiencing flutter; and b) Post-flutter transient simulation, in which the structural non-linearities cause the occurence of limit cycle oscillations (LCOs). The former (a) is done by iteratively varying the dynamic pressure in the search for negatively damped eigenmodes, and the latter (b) requires direct solution in the time domain, which is achieved via an implicit, iterative Newmark-type scheme.

The model and solvers have been verified through comparison with several bench-mark results from the literature. The comparative study has been performed in multiple levels: mesh convergence, nonlinear laminated plate vibration (purely structural), flutter boundary prediction for stiffened panels, and nonlinear aeroelastic simulation of unstiffened panels. Results have demonstrated that the code developed for this project is capable of yielding accurate solutions for stiffened and unstiffened, thin and thick, isotropic and laminated panels, in both linear and nonlinear regimes.

The main novel case studied here considers a double panel, i.e., a rectangular plate with a centrally-placed stiffener that subdivides it into two equal square cells. By comparing the linear and nonlinear aeroelastic behaviour of double-celled panels with those of a reference single square panel, this work has focused on assessing the limitations and inaccuracies of the classical assumption of considering each cell in a skin structure as an isolated, ideally-fixed panel. In order to do that, results have been parametrised in terms of the stiffener's cross-sectional aspect ratio, α, which determines its torsional and bending stiffnesses and controls the structural coupling between adjacent cells. In this

context, the present analysis has been able to show that:

- Flutter tends to occurs earlier for double-celled panels. The critical dynamic pressure obtained for a double-celled panel increases as the stiffener becomes more rigid, asymptotically approaching that of a single panel (isolated and fully clamped) as α becomes larger.

- The maximum LCO amplitudes of double panels can be several times higher than that displayed by the corresponding single panels.

- Jump discontinuities in LCO amplitude diagrams can occur for panels stiffened by relatively flexible beams. Such discontinuities are due to the non-linearity of the complex aeroelastic system, and are related to a change in the flutter mechanism. The post-jump mechanism is capable of extracting considerably more energy from the flow than the pre-jump mechanism.

- In the post-flutter regime, the cells in a reinforced panel can display highly-uneven maximum displacements and mean mechanical energies.

- The stiffener absorbs a very small amount of mechanical energy, playing the role of a dynamic boundary condition rather than that of an energy absorber.

- The answer to the question "when can stiffeners be safely approximated as ideal fixations (clamped boundaries)?" depends greatly upon the structural arragement at hand. For instance, the same stiffener can be considered as extremely rigid (practically clamped) when used on an angle-ply panel, but very flexible for a cross-ply panel (of course, depending of flow direction).

This work has therefore demonstrated that the single-panel model, widely explored in the literature, should not be employed indiscriminately without an assessment of the effective stiffness of reinforcements. Spars, frames and longerons tend to be rather sturdy, but this is not always true for stringers, which are used in both wing and fuselage structures. This is due to the fact that their role is not to withstand loads, but to provide the skin with stability against buckling and other thin-shell phenomena. Therefore, when considering panel flutter, it is important to either simulate the whole structure – which could demand prohibitive computational cost/time – or evaluate how stiff the stringers effectively are when compared to the skin.

The results presented in this work offer a new perspective on the flutter of reinforced panels. The comparative study between single and double-celled panels and the examination of amplitude jumps represent important novelty, especially the energy-based analysis. The results have resulted in an orginal article which has been submitted to the *Journal of Sound and Vibration* (Elsevier) and is currently under peer review.

BIBLIOGRAPHY

ABDEL-MOTAGALY, K.; DUAN, B.; MEI, C. Nonlinear panel response at high acoustic excitations and supersonic speeds. In: STRUCTURES, STRUCTURAL DYNAMICS, AND MATERIALS EXHIBIT, 40., 1999, St. Louis. **Proceedings...** Reston: AIAA, 1999.

AKAY, H. U. Dynamic large deflection analysis of plates using mixed finite elements. **Computers & Structures**, Amsterdam, v. 11, n. 1-2, p. 1–11, 1980.

ALDER, M. Development and validation of a fluid–structure solver for transonic panel flutter. **AIAA Journal**, Reston, v. 53, n. 12, p. 3509–3521, 2015.

ASHLEY, H.; ZARTARIAN, G. Piston theory – a new aerodynamic tool for the aeroelastician. **Journal of the Aeronautical Sciences**, Reston, v. 23, n. 12, p. 1109–1118, 1956.

BEIN, T. et al. Hypersonic flutter of a curved shallow panel with aerodynamic heating. In: STRUCTURES, STRUCTURAL DYNAMICS AND MATERIALS CONFERENCE, 34., 1993, La Jolla. **Proceedings...** Reston: AIAA, 1993.

BISMARCK-NASR, M. N. Finite element method applied to the supersonic flutter of circular cylindrical shells. **International Journal for Numerical Methods in Engineering**, New Jersey, v. 10, n. 2, p. 423–435, 1976.

_____. Finite element analysis of aeroelasticity of plates and shells. **Applied Mechanics Reviews**, New York, v. 45, n. 12, p. 461, 1992.

CARRERA, E.; ZAPPINO, E.; PETROLO, M. Analysis of thin-walled structures with longitudinal and transversal stiffeners. **Journal of Applied Mechanics**, New York, v. 80, n. 1, p. 011006, 2013.

CASTRO, S. G. P. et al. Flutter of stiffened composite panels considering the stiffener's base as a structural element. **Composite Structures**, Amsterdam, v. 140, p. 36–43, 2016.

CHEN, J. K.; SUN, C. T. Nonlinear transient responses of initially stressed composite plates. **Computers & Structures**, Amsterdam, v. 21, n. 3, p. 513–520, 1985.

CHEN, W.-H.; LIN, H.-C. Flutter analysis of thin cracked panels using the finite element method. **AIAA Journal**, Reston, v. 23, n. 5, p. 795–801, 1985.

CHOW, T. S. On the propagation of flexural waves in an orthotropic laminated plate and its response to an impulsive load. **Journal of Composite Materials**, Thousand Oaks, v. 5, n. 3, p. 306–319, mar 1971.

CUNNINGHAM, H. J. Flutter analysis of flat rectangular panels based on three-dimensional supersonic potential flow. **AIAA Journal**, Reston, v. 1, n. 8, p. 1795–1801, 1963.

DIXON, I. R.; MEI, C. Finite element analysis of large-amplitude panel flutter of thin laminates. **AIAA Journal**, Reston, v. 31, n. 4, p. 701–707, 1993.

DOWELL, E. H. Flutter of multibay panels at high supersonic speeds. **AIAA Journal**, Reston, v. 2, n. 10, p. 1805–1814, 1964.

_____. Generalized aerodynamic forces on a flexible plate undergoing transient motion. **Quarterly of Applied Mathematics**, v. 24, n. 4, p. 331–338, 1966.

_____. Nonlinear oscillations of a fluttering plate. **AIAA Journal**, Reston, v. 4, n. 7, p. 1267–1275, 1966.

_____. Nonlinear flutter of curved plates. **AIAA Journal**, Reston, v. 7, n. 3, p. 424–431, 1969.

_____. Panel flutter – a review of the aeroelastic stability of plates and shells. **AIAA Journal**, Reston, v. 8, n. 3, p. 385–399, 1970.

_____. Generalized aerodynamic forces on a flexible plate undergoing transient motion in a shear flow with an application to panel flutter. **AIAA Journal**, Reston, v. 9, p. 834–841, 1971.

_____. **Aeroelasticity of Plates and Shells**. Leyden: [s.n.], 1975.

FERNANDES, R. R.; TAMIJANI, A. Y. Flutter analysis of laminated curvilinear-stiffened plates. **AIAA Journal**, Reston, v. 55, n. 3, p. 998–1011, 2017.

FERREIRA, A. J. M. **MATLAB codes for finite element analysis: solids and structures**. Dordrecht: Springer Science & Business Media, 2008. v. 157.

KUO, C.-C.; MORINO, L.; DUGUNDJI, J. Perturbation and harmonic balance methods for nonlinear panel flutter. **AIAA Journal**, Reston, v. 10, n. 11, p. 1479–1484, 1972.

KUO-JIUN, L.; PONG-JEU, L.; JIANN-QUO, T. Flutter analysis of composite panels using high-precision finite elements. **Computers & Structures**, Amsterdam, v. 33, n. 2, p. 561–574, 1989.

LEE, D.-M.; LEE, I. Vibration analysis of anisotropic plates with eccentric stiffeners. **Computers & Structures**, Amsterdam, v. 57, n. 1, p. 99–105, 1995.

LEE, I. Supersonic flutter analysis of stiffened laminated plates subject to thermal load. **Journal of Sound and Vibration**, Amsterdam, v. 224, n. 1, p. 49–67, 1999.

LEECH, J. W. Stability of finite-difference equation for the transient response of a flat plate. **AIAA J.**, v. 3, n. 9, p. 1772–1773, 1965. ISSN 0001-1452.

LIAO, C.-L.; SUN, Y.-W. Flutter analysis of stiffened laminated composite plates and shells in supersonic flow. **AIAA Journal**, Reston, v. 31, n. 10, p. 1897–1905, 1993.

LIU, Y.; SOH, C.-K. Shear correction for Mindlin type plate and shell elements. **International Journal for Numerical Methods in Engineering**, New Jersey, v. 69, n. 13, p. 2789–2806, mar 2007.

LOCK, M. H.; FARKAS, E. F. Flutter of two-bay flat panels of infinite span at supersonic mach numbers. **AIAA Journal**, Reston, v. 3, n. 9, p. 1692–1697, 1965.

MARQUES, F. D.; NATARAJAN, S.; FERREIRA, A. J. M. Evolutionary-based aeroelastic tailoring of stiffened laminate composite panels in supersonic flow regime. **Composite Structures**, Amsterdam, v. 167, p. 30–37, 2017.

MEI, C. A finite-element approach for nonlinear panel flutter. **AIAA Journal**, Reston, v. 15, n. 8, p. 1107–1110, 1977.

MEI, C.; ABDEL-MOTAGALY, K.; CHEN, R. Review of nonlinear panel flutter at supersonic and hypersonic speeds. **Applied Mechanics Reviews**, New York, v. 52, n. 10, p. 321, 1999.

MUKHERJEE, S.; PARTHAN, S. Wave propagation in one-dimensional multi-bay periodically supported panels under supersonic fluid flow. **Journal of Sound and Vibration**, Amsterdam, v. 186, n. 1, p. 71–86, 1995.

NETTLES, A. T. Basic mechanics of laminated composite plates. **NASA Reference Publication 1351**, Washington, 1994.

OH, I. K.; LEE, I.; LEE, D.-M. Non-linear transient response of fluttering stiffened composite plates subject to thermal load. **Journal of Sound and Vibration**, Amsterdam, v. 245, n. 4, p. 715–736, 2001.

PACHECO, D. R. Q.; MARQUES, F. D.; FERREIRA, A. J. M. Nonlinear finite element aeroelastic analysis of multibay panels in supersonic flow regime. **Thin-Walled Structures**, Amsterdam, v. 120, p. 470–478, 2017.

_____. On the effects of structural coupling on the supersonic flutter and limit cycle oscillations of transversely reinforced panels. **Journal of Fluids and Structures**, Amsterdam, v. 79, p. 158–170, feb 2018.

PACHECO, D. R. Q. et al. Nonlinear finite element post-flutter analysis of multibay composite panels in supersonic regime. **Composite Structures**, Amsterdam, v. 180, p. 883–891, 2017.

PANY, C.; PARTHAN, S. Flutter analysis of periodically supported curved panels. **Journal of Sound and Vibration**, Amsterdam, v. 267, n. 2, p. 267–278, 2003.

PICA, A.; WOOD, R. D.; HINTON, E. Finite element analysis of geometrically nonlinear plate behaviour using a Mindlin formulation. **Computers & Structures**, Amsterdam, v. 11, n. 3, p. 203–215, 1980.

REDDY, J. N. Geometrically nonlinear transient analysis of laminated composite plates. **AIAA Journal**, Reston, v. 21, n. 4, p. 621–629, 1983.

_____. **Mechanics of Laminated Composite Plates and Shells: Theory and Analysis**. Boca Raton: [s.n.], 2004. v. 2nd. 855 p.

REDDY, J. N.; MAHAFFEY, P. Generalized beam theories accounting for von Kármán nonlinear strains with application to buckling. **Journal of Coupled Systems and Multiscale Dynamics**, Valencia, v. 1, n. 1, p. 120–134, 2013.

RODDEN, W. P. Flutter of multibay panels at supersonic speeds. **AIAA Journal**, Reston, v. 2, n. 8, p. 1476–1478, 1964.

SARMA, B. S.; VARADAN, T. K. Nonlinear panel flutter by finite-element method. **AIAA Journal**, Reston, v. 26, n. 5, p. 566–574, 1988.

SAWYER, J. W. Flutter and buckling of general laminated plates. **Journal of Aircraft**, Reston, v. 14, n. 4, p. 387–393, 1977.

SHIAU, L. C.; CHANG, J. T. Finite element analysis of supersonic flutter of multibay composite panels. **Computers & Structures**, v. 39, n. 3-4, p. 269–276, 1991.

SHISHAEVA, A.; VEDENEEV, V.; AKSENOV, A. Nonlinear single-mode and multi-mode panel flutter oscillations at low supersonic speeds. **J. Fluids Struct.**, Elsevier, v. 56, p. 205–223, 2015. ISSN 08899746.

SHITOV, S.; VEDENEEV, V. Flutter of rectangular simply supported plates at low supersonic speeds. **Journal of Fluids and Structures**, Amsterdam, v. 69, n. 8, p. 154–173, 2017.

SHORE, C. P.; MEI, C.; GRAY, C. E. Finite element method for large-amplitude two-dimensional panel flutter at hypersonic speeds. **AIAA Journal**, Reston, v. 29, n. 2, p. 290–298, 1991.

SRINIVAS, S. A refined analysis of composite laminates. **Journal of Sound and Vibration**, Amsterdam, v. 30, n. 4, p. 495–507, 1973.

STROUD, A. H.; SECREST, D. **Gaussian quadrature formulas**. New Jersey: Prentice-Hall, 1966.

SUNDER, P. J.; RAMAKRISHNAN, C. V.; SENGUPTA, S. Finite element analysis of 3-ply laminated conical shell for flutter. **International Journal for Numerical Methods in Engineering**, New Jersey, v. 19, n. 8, p. 1183–1192, 1983.

SZABO, B. A.; BABUÂŠKA, I. **Finite element analysis**. Hoboken: [s.n.], 1991.

VEDENEEV, V. V. Panel flutter at low supersonic speeds. **Journal of Fluids and Structures**, Amsterdam, v. 29, p. 79–96, 2012.

WHITNEY, J. M. Stress analysis of thick laminated composite and sandwich plates. **Journal of Composite Materials**, Thousand Oaks, v. 6, n. 3, p. 426–440, 1972.

_____. Shear correction factors for orthotropic laminates under static load. **Journal of Applied Mechanics**, New York, v. 40, n. 1, p. 302, 1973.

XUE, D. Y.; MEI, C. Finite element nonlinear flutter and fatigue life of two-dimensional panels with temperature effects. **Journal of Aircraft**, Reston, v. 30, n. 6, p. 993–1000, 1993a.

_____. Finite element nonlinear panel flutter with arbitrary temperatures in supersonic flow. **AIAA Journal**, Reston, v. 31, n. 1, p. 154–162, 1993b.

ZHAO, H.; CAO, D. A study on the aero-elastic flutter of stiffened laminated composite panel in the supersonic flow. **Journal of Sound and Vibration**, Amsterdam, v. 332, n. 19, p. 4668–4679, 2013.